Effect of doping on the photocatalytic, electronic and mechanical properties of sol-gel titanium dioxide films

A Thesis

Submitted to the Faculty

of

Drexel University

by

Murat Kurtoglu

In Partial Fulfillment of the Requirements

for the Degree of

Doctor of Philosophy

in Materials Science and Engineering

2011

TABLE OF CONTENTS

LIST OF FIGURES vii

LIST OF TABLES xv

Acknowledgements xvii

Abstract xix

CHAPTER 1) LITERATURE REVIEW 1

1.1. Introduction 1

1.2. Heterogeneous Photocatalysis 3

  1.2.1. Applications 11

    1.2.1.1. Water Purification 12

    1.2.1.2. Self-cleaning coatings 13

    1.2.1.3. Antimicrobial Surfaces 14

    1.2.1.4. Other Applications 15

1.3. Photocatalytic Materials 15

1.4. Titanium Dioxide 17

  1.4.1. Structure 17

  1.4.2. Electronic Structure 19

  1.4.3. Production Methods 22

    1.4.3.1. Powders 22

    1.4.3.2. Films 22

      1.4.3.2.1. Hydro/Solvo-Thermal Synthesis 22

      1.4.3.2.2. Sol-Gel 23

  1.4.4. Mechanical Properties of Titanium Dioxide Films 27

  1.4.5. Improving Photocatalytic Activity of Titanium Dioxide Films 27

    1.4.5.1. Visible-Light Photocatalytic Activity 28

    1.4.5.2. Substrate Effect 28

    1.4.5.3. Surface Area of Thin Films 29

1.5. Conclusions 30

OBJECTIVES 32

CHAPTER 2) MATERIALS AND METHODS 33

2.1. Materials 33
  2.1.1. Titanium precursors 33
  2.1.2. Solvents 33
  2.1.4. Dopant Precursors 34
2.2. Film Synthesis 34
  2.2.1. Synthesis of “sol” 35
    2.2.1.1. Doping 37
2.3. Simulation of Doping 39
  2.3.1. Density Functional Theory 39
2.4. Photocatalytic Activity Tests 42
2.5. Nanoindentation 45
2.6. Structural Characterization 48
  2.6.1. X-Ray Difffraction 48
  2.6.2. Micro-Raman Spectroscopy 48
  2.6.3. UV-Vis Spectroscopy 48
  2.6.4. Fourier-Transformed Infrared Spectroscopy (FT-IR) 48
  2.6.5. Scanning/Transmission Electron Microscopy 48

CHAPTER 3) RESULTS AND DISCUSSION 49

3.1. Synthesis of Undoped Titanium Dioxide Films 49
  3.1.1. Introduction 49
  3.1.2. Structure 49
  3.1.3. Mechanical Properties 53
  3.1.4. Photocatalytic Activity 57
  3.1.5. Conclusions 59
3.2. Modeling and Simulation of Doping 60
  3.2.1. Introduction 60
  3.2.2. Simulations Parameters 60
  3.2.3. Metal Doping 61
  3.2.4. Nitrogen Doping 71

3.2.5. Metal-Nitrogen Doping 72
3.2.6. Conclusions 77
3.3. Carbothermally Reduced Titanium Dioxide Films 79
3.3.1. Introduction 79
3.3.2. Experimental 79
3.3.3. Results and Discussion 80
3.3.4. Conclusions 102
3.4. Metal Doped Titanium Dioxide Films 103
3.4.1. Introduction 103
3.4.2. Experimental 103
3.4.3. Results and Discussion 104
3.4.4. Conclusions 118
3.5. Nitrogen Doped Titanium Dioxide Films 119
3.5.1. Introduction 119
3.5.2. Experimental 119
3.5.4. Conclusions 123
3.6. Metal-Nitrogen Doped Titanium Dioxide Films 125
3.6.1. Introduction 125
3.6.2 Experimental 125
3.6.3. Results and Discussion 125
3.6.3.1. Cr-N-doped Titanium Dioxide Films 128
3.6.3.1.1. Cr-Doped TiO_2: Non-compensated Case 133
3.6.3.1.2. Cr-Doped TiO_2: Compensated Case 137
3.6.3.1.3. Cr-N-Doped TiO_2 140
3.6.3.2. V-N-doped Titanium dioxide 148
3.7. Formation of MoO3 Nanobelts on Titanium Dioxide Films 156
3.7.1. Experimental 156
3.7.2. Results and Discussion 157
3.7.3. Conclusion 167
CHAPTER 4) SUMMARY AND CONCLUSIONS 168
REFERENCES 173

CURRICULUM VITA... 191

LIST OF FIGURES

Figure 1-1: Intensity of sunlight versus wavelength for AM 1.5 conditions (ASTM 2008). The filled area shows the part of the spectrum that can be absorbed by titanium dioxide. 7

Figure 1-2: Schematics of the bulk and surface electron-hole dynamics of a photocatalytic particle. Electrons reaching to the surface either recombine on the surface or reduce an adsorbed electron acceptor (e.g. dissolve oxygen). (Palmisano, Augugliaro et al. 2007).. 11

Figure 1-3: Schematics of the self-cleaning effect on a titanium dioxide coated window glass. (1) Dirt particles on the titanium dioxide film is (2) decomposed to inorganic minerals by the photocatalytic action induced by solar irradiation and (3) removed from the surface by rain water penetrating between the dirt and superhydrophillic film. 14

Figure 1-4: Relative photocatalytic activity of several oxides (Miyauchi, Nakajima et al. 2002). Total amount of dye adsorbed on the oxide vs. illumination time is given. TiO_2, ZnO and $SrTiO_3$ are highly active. SnO_2, Fe_2O_3 and In_2O_3 showed slight photocatalytic activity. V_2O_5, CeO_2, CuO, MoO_3 and Cr_2O_3 did not show any photocatalytic activity..... 16

Figure 1-5: Titanium dioxide mineral sources: (a) rutile, (b) ilmenite and (c) leucoxene. 17

Figure 1-6: World and US titanium ore production amounts vs. year. 18

Figure 1-7: Crystal structure of the most common phases of titanium dioxide: (a) rutile, (b) anatase and (c) brookite... 19

Figure 1-8: Density of states (DOS) plot of titanium dioxide (anatase)........................... 21

Figure 1-9: (A) Stages of dip coating process: (a-e) batch; (f) continuous. (B) Detail of the liquid flow patterns in area 3 of the continuous process. U is the withdrawal speed, S is the stagnation point, δ is the boundary layer and h is the thickness of the liquid film (Brinker and Scherer 1990). 25

Figure 1-10: Schematics of the steady-state deposition stage of the dip-coating process (Brinker and Scherer 1990). 26

Figure 2-1: Titanium dioxide precursors: (a) titanium (IV) isopropoxide, (b) titanium (IV) butoxide, (c) titanium (IV) chloride. 33

Figure 2-2: Schematics of the individual steps of synthesis of titanium dioxide films. 35

Figure 2-3: Procedure used for the undoped titanium dioxide sol synthesis. 36

Figure 2-4: Procedure used for the metal doped titanium dioxide sols (1% at. Mo-doped titanium dioxide is given as specific example). 38

Figure 2-5: Schematics of the setup used for post-annealing of titanium dioxide films (for nitrogen doping, carbothermal reduction). 39

Figure 2-6: (a) Molecular structure and (b) optical spectrum of methylene blue. 43

Figure 2-7: Methylene blue degradation test setup. 44

Figure 2-8: Schematics of the nanoindentation process (left) and interpretation of a typical load-displacement curve as obtained from the nanoindentation results. 46

Figure 3-1: Raman spectra of titanium dioxide films on glass substrates calcined at 400°C, 450°C, 500°C and 550°C. Excitation wavelength: 514 nm, 100x magnification. 50

Figure 3-2: Raman spectra of titanium dioxide films on glass substrates calcined at 500°C with various heating rates. Excitation wavelength: 514 nm, 100x magnification. 51

Figure 3-3: SEM micrographs of the surface of titanium dioxide films calcined at 500°C at a heating rate of 50°C/min (a) and 5°C/min (b), at 350°C with a heating rate of 5°C/min (b-d). 53

Figure 3-4: Nanoindentation Load-Displacement curves of sol-gel titanium dioxide films calcined at different temperatures at a heating rate of 10°C/min and dwell time of 1 hr. 55

Figure 3-5: Nanoindentation Load-Displacement curves of sol-gel titanium dioxide films calcined at 500°C at different heating rates and dwell time of 1 hr. 56

Figure 3-6: Schematics explaining the heating rate on the stress formation of titanium dioxide films. 57

Figure 3-7: Photocatalytic rate constants of sol-gel titanium dioxide films on glass calcined at various temperatures and various heating rates. 58

Figure 3-8: Calculated Gibbs free energy changes of doping of various elements into the titanium dioxide (anatase) lattice. 64

Figure 3-9: Trend in the Gibbs free energy cost of doping with different elements. 65

Figure 3-10: Resulting volume changes in the anatase lattice accompanying the doping with different elements in the transition block. 66

Figure 3-11: Calculated net spin of metal-doped structures. 67

Figure 3-12: Calculated optical spectra of (a) Sc-, (b) V-, (c) Cr-, (d) Mn-, (e) Fe-, (f) Co-, (g) Ni-, (h) Cu-, (i) Zn-, (j) Ga-, and (k) Ge-doped anatase. Calculated optical spectrum of anatase is given at each figure for comparison. 70

Figure 3-13: Density of states (DOS) plots of N-doped anatase with various nitrogen concentrations. 71

Figure 3-14: Calculated optical absorption spectra of N-doped anatase with various nitrogen concentrations. 72

Figure 3-15: Metal-nitrogen doped anatase cell used for calculations. 73

Figure 3-16: Calculated Gibbs free energy changes of metal co-doping into the nitrogen-doped titanium dioxide (anatase) lattice.. 74

Figure 3-17: Calculated optical spectra of (a) Sc-N, (b) V-N, (c) Zn-N, (d) Cr-N, (e) Mn-N, (f) Ga-N, (g) Fe-N, (h) Co-N, (i) Ge-N, (j) Ni-N, and (k) Cu-N doped anatase. Calculated optical spectrum of nitrogen doped anatase is given at each figure for comparison...... 75

Figure 3-18: Calculated net spin of metal-nitrogen doped anatase with various metals. 76

Figure 3-19: Metal-nitrogen bond length in metal-nitrogen doped anatase structures. 77

Figure 3-20: Refractive index (n) vs. wavelength plots of films calcined at (a) 900°C in air, (b) 700°C under N_2, (c) 800°C under N_2, and (d) 900°C under N_2 81

Figure 3-21: XRD patterns of the films calcined at various temperatures (a) in air and (b) under nitrogen. ●: anatase, ■: rutile. 83

Figure 3-22: Raman spectra of the films calcined at various temperatures in (a) air and (b) nitrogen. Carbon range of the Raman spectra of nitrogen-calcined films is shown in (c). Spectra in (c) have been normalized using the peak of Si at 960 cm^{-1}. (d) The lowest frequency anatase band positions for air-calcined samples with respect to calcination temperature... 86

Figure 3-23: Morphological evolution of the films calcined at 600°C (a, d), 900°C (b, e) and 1000°C (c, f). a, b, c belong to the films calcined under nitrogen. 89

Figure 3-24: SEM image around a micro-crack showing the extensive growth of TiO_2 particles on the edge. 90

Figure 3-25: TEM images of the films calcined at 900°C in (a) air and (b) nitrogen......... 91

Figure 3-26: Optical spectra of TiO_2 films calcined in (a) air and (b) nitrogen. Sample photographs are shown in (c)... 93

Figure 3-27: Reflection maximums of films with respect to the calcination temperature and environment. 95

Figure 3-28: Photocatalytic activity of the films as obtained from methylene blue decomposition test. 96

Figure 3-29: (a) Indentation hardness and (b) modulus of the films with respect to the calcination temperature and environment. Load-displacement curves of the films calcined at 400°C, 600°C and 900°C under (c) air and (d) nitrogen............................... 101

Figure 3-30: SEM image of a fracture surface of TiO_2 film on Si (100). The image was taken at a 75° angle, so the real thickness is given as $t = t_o \times \cos(75) = 101$nm, where t and t_o denotes real and observed thickness, respectively. 105

Figure 3-31: XRD patterns of the anatase (110) peak for un-doped and doped TiO_2 films. 106

Figure 3-32: Raman spectra of un-doped, Ag-, Co-, Cu-, Ga-, Mo-, and Ta-doped films (a) and FTIR reflection spectra near grazing angle (80°) of the films on SiO_2 coated glass (b). 109

Figure 3-33: Optical spectra of the undoped and doped TiO_2 films on (a) glass and (b) SiO_2 coated glass near the absorption edge. Representative Tauc plots of (i) undoped, (ii) Ag-and (iii) Mo-doped films on (c) glass and (d) SiO_2 coated glass. 112

Figure 3-34: Photocatalytic activity of TiO_2 films on (a) glass and (b) SiO_2-coated glass. 113

Figure 3-35: Raman spectrum of the 5% Mo-doped TiO_2 film. Surface of the film as pictured by SEM is shown in the inset. Proposed mechanism of the process is shown on the right. A: anatase, B: brookite, M: sodium molybdate, G: glass.............................. 115

Figure 3-36: Photocatalytic activity of metal-doped films with various metal dopant concentrations. 116

Figure 3-37: Nanoindentation hardness values of the metal doped films. Undoped film's value is given for comparison. 117

Figure 3-38: Optical absorption spectra of N-doped films with increasing nitrogen concentration. 120

Figure 3-39: Photocatalytic rate constant vs. nitrogen dopant concentration under UV and visible light. 121

Figure 3-40: Nanoindentation hardness of titanium dioxide films vs. nitrogen dopant concentration. 123

Figure 3-41: Photocatalytic rate constants of metal-nitrogen doped titanium dioxide films with different metal co-dopants under ultraviolet light. 126

Figure 3-42: Photocatalytic rate constants of metal-nitrogen doped titanium dioxide films with different metal co-dopants under visible light. 127

Figure 3-43: Nanoindentation hardness of the metal-nitrogen doped films. Nitrogen-doped film (no metal co-dopant) is given for comparison. 128

Figure 3-44: Photocatalytic rate constants (methylene blue decomposition) of undoped, N-, Cr-, and Cr-N-doped films under UV and visible light. Individual rate constants are given on top of the respective bars. 129

Figure 3-45: XPS spectra of the films around (a) Cr 2p, (b) N 1s, (c) Ti 2p, (d) valence band (inset: Cr-N-TiO_2 closer view) , and (e) O 1s. 132

Figure 3-46: DOS plots of Cr-doped TiO_2 in the (a) uncompensated and (b) compensated state. DOS plot of undoped anatase is given as the dotted line. Partial DOS arising from Cr d orbitals are shown as filled plots. 136

Figure 3-47: (a) Experimental and (b) calculated optical spectra of (compensated and uncompensated) Cr-doped TiO_2. (c) Optical “difference” spectra, where undoped TiO_2 spectrum was subtracted from Cr-doped TiO_2 spectrum. Individual spectra were normalized to their respective peak positions before further processing. 139

Figure 3-48: 2 x 2 x 1 anatase supercell for calculations. Additional nitrogen positions considered are numbered, i.e. P2, P3, and P4. 141

Figure 3-49: Calculated DOS plot of (a) $Ti_{15}CrO_{31}N$, (b) $Ti_{15}CrO_{30}N_2$, (c) $Ti_{15}CrO_{29}N_3$, (d) $Ti_{15}CrO_{30}N$, (e) $Ti_{15}CrO_{29}N_2$, and (f) $Ti_{15}CrO_{28}N_3$ 144

Figure 3-50: Calculated electron densities around Cr atoms in Cr-doped (left) and Cr-N-doped (right) TiO_2. 146

Figure 3-51: XRD pattern of samples (a) calcined at 650°C in air and (b) post-treated at 650°C under NH_3. A: anatase, R: rutile. Anatase (101) positions are shown above the respective peaks. 149

Figure 3-52: Optical spectra of the films calcined in air and air + NH_3. 150

Figure 3-53: Visible-light photocatalytic activity of vanadium and vanadium-nitrogen co-doped films. Nitrogen concentration is estimated to be 10 at. % in all N-doped films. Photocatalytic activity of undoped and nitrogen-doped titanium dioxide films are given for comparison. 151

Figure 3-54: UV-light photocatalytic activity of vanadium and vanadium-nitrogen co-doped films. Nitrogen concentration is estimated to be 10 at. % in all N-doped films. Photocatalytic activity of undoped and nitrogen-doped titanium dioxide films are given for comparison. 152

Figure 3-55: Electronic potentials of TiO_2 and V-doped TiO_2 in aqueous solutions at pH 7 and pH 14. 154

Figure 3-56: Density of States (DOS) plot of TiO_2 (anatase), V-doped TiO_2, and V,N-doped TiO_2. 155

Figure 3-57: Low-magnification (a) and high-magnification (b) SEM images of MoO_3 nanobelts. A TEM image and a single-crystal SAED pattern (inset) of a typical nanobelt are shown in (c). XRD pattern of nanobelts is shown in (d). 158

Figure 3-58: SEM images and XRD patterns of α-MoO_3 on TiO_2 coated (a,b) plain soda-lime glass and (c,d) quartz slides; both coatings were calcined at 500°C. (□ - Na_2MoO_4) 159

Figure 3-59: MoO_3 structures obtained after quenching at (a) 350°C and (b) 400°C. (c) SEM image of the film prepared by using 2-propanol as the solvent. 160

Figure 3-60: (a) (001) Anatase plane (left) and (010) MoO_3 plane. (b) Principal growth directions of MoO_3. (c) A typical anatase crystal. (d) nucleation of (010) MoO_3 on (001) faces of polycrystalline anatase and (e) growth of nanobelts. 162

Figure 3-61: Total reflection spectra and photographs of (a) MoO_3 nanobelts, (b) MoO_3 nanoplatelets, (c) carbon-coated MoO_3 nanobelts, (d) carbon-coated MoO_3 nanoplatelets, and (e) carbon-coated glass. 165

Figure 3-62: SEM images of the TiO_2 coated MoO_3 nanobelts (a,b) and a plot showing photocatalytic degradation of methylene blue by TiO_2 coated MoO_3 nanobelts, TiO_2 film and a glass substrate (c). 166

Figure 3-63: Contact angle of (a) carbon coated and (b) flurosilane coated MoO_3 nanobelts, as determined by the sessile drop method. 167

LIST OF TABLES

Table 1-1: Primary processes and associated characteristic time domains of titanium dioxide photocatalysis steps (Hoffmann, Martin et al. 1995). 10

Table 3-1: Photocatalytic reaction rate constants vs. heating rate/calcination temperature of titanium dioxide films 59

Table 3-2: Accuracy and the computational cost of the selected approximations and exchange-correlation functionals. Calculations were performed with a conventional anatase cell on a dual-core Intel Xeon 2.8 GHz processor. Error is given as the largest deviation from the lattice parameters. 61

Table 3-3: Summary of results of the doping of anatase with 4th Period elements......... 68

Table 3-4: Summary of results of the doping of anatase with 5th Period elements......... 69

Table 3-5: Summary of results of the doping of anatase with 6th Period elements......... 69

Table 3-6: Summary of XRD crystal size measurements. 84

Table 3-7: Calculated first-order photocatalytic rate constants of the films. 97

Table 3-8: Crystallite size, anatase (110) peak position and ionic radiuses of the dopants 107

Table 3-9: Calculated band gaps of the films... 111

Table 3-10: Methylene Blue photocatalytic decomposition rate constants (hr^{-1}) 113

Table 3-11: DFT calculation summary of non-compensated Cr-doped TiO_2 134

Table 3-12: Calculation results for TiO_2 anatase... 135

Table 3-13: Summary of the calculation results of the Cr-N doped systems with varying amount of N and with/without oxygen vacancy. 147

Acknowledgements

Over the last four years of my graduate research at Drexel University, I have learned great things not only about science and academics, but also about the life, the truth and the faith. I have truly enjoyed every moment of learning and I am grateful to have these kinds of experience in my life. I believe this is possible only because of all the people supporting me many ways and I would like to acknowledge them.

First of all, I would like to thank my advisor, Prof. Yury Gogotsi, for all the support and guide throughout the years. He gave me many opportunities and he was always supportive whenever I proposed new research topics or brought some problems of ongoing study or even personal matter. I also thank to my committee members, Prof. Caroline Schauer, Prof. Wei-Heng Shih in Materials Engineering, and Prof. Karl Sohlberg in Chemistry.

Also, I want to thank to my employer Gurallar Artcraft and Gural Family for their support. I would like to thank Mr. Erol Gural for supporting me all these years with utmost understanding and patience. I would not be here without his support. I would also like to thank Dr. Ali Altiner, Mr. Omer Alagoz, and my colleagues at ArtCraft for their support and encouragement.

I would like to thank all the former and current members of Drexel Nanomaterials group for their help. All of the group members helped me with my work and contributed to me in countless ways, particularly Travis Longenbach, Min Heon, Riju Singhal, Sayan

Bhattacharyya, Amanda Pentecost, Sun-Hwa Yeon, Byung-Yong Lee, Goknur Cambaz and everyone else. Special thanks to Danielle Tadros for her patience with me, even after my countless inquiries for her help.

My experience at Drexel would have not been the same without the terrific staff of Materials Engineering and I am grateful for their help and support.

I want to thank Ed Basgall, Zhorro Nikolov and Craig Johnson for teaching me how to operate all these characterization tools.

Of course, none of this would have been possible at all without the love support of my family. Always there for me no matter what, I have the best parents and brothers anyone can hope for.

Finally, I have saved the most important person for last. My wife Derya has done as much for me as any person could ask for. Her endless love and support has made all the difference.

Abstract

Effect of doping on the photocatalytic, electronic and mechanical properties of sol-gel titanium dioxide films

Murat Kurtoglu

Advisor: Prof. Yury Gogotsi

Heterogeneous photocatalysis has been an active research area over the last decade as a promising solution for energy generation and environmental problems which has led to promising applications from air and water purification systems, self-cleaning and self-sterilizing surfaces to solar cells and hydrogen production from water dissociation reaction. Titanium dioxide (TiO_2), an abundant material with a high photocatalytic efficiency and chemical stability, is undoubtedly the most widely studied and used among all photocatalytic materials. Although titanium dioxide has been used in powder form, its immobilized form (film) is necessary from practical application standpoint. However, there are several shortcomings of titanium dioxide films that need to be addressed to realize a wide range of successful applications: lack of visible light activity, poisoning of the catalytic performance by the substrate and the low surface area compared to powder forms. In addition, mechanical properties of such films have not been investigated thoroughly, which may be critical when abrasion and weathering resistance are necessary. To address each of these issues, a systematic experimental and theoretical investigation of doping titanium dioxide films with a variety of elements were conducted. Utilizing theoretical calculations to filter elements for experimental studies as well as interpretation of the experimental results, several dopant or dopant combinations were found to remedy some of the issues of photocatalytic titanium dioxide films.

Doping with 32 metals, nitrogen and 11 metal-nitrogen combinations are investigated theoretically and the results are used as guideline for the experimental studies. Particular attention is given to certain metal dopants such as Cr, V, Mo, Ta and Ga not just because of their relatively modest cost but also their non-toxicity and wide availability of their compatible compounds for sol-gel synthesis. While metal-dopants improved the overall efficiency and mechanical properties of titanium dioxide films, visible light activity is only achieved with nitrogen and metal-nitrogen doping where some of the metal co-dopants significantly improved the overall photocatalytic efficiency compared to nitrogen-only doped films.

In addition, majority of the experimental studies is accompanied by nanoindentation technique to study the effect of doping and calcination on the key mechanical properties of titanium dioxide films. It is shown that good mechanical properties – good photocatalytic activity combinations can be achieved by a choice of appropriate dopant –dopant combinations and coupled with appropriate calcination parameters.

Results of the theoretical and experimental investigations led to the development of first commercial photocatalytic tableware glass items which can be utilized under indoor lighting conditions by carefully selecting metal-nitrogen couples for doping of titanium dioxide films.

CHAPTER 1) LITERATURE REVIEW

1.1. Introduction

Heterogeneous photocatalysis has been an active research area over the last decade as a promising solution for energy generation and environmental problems which has led to promising applications including air and water purification systems, self-cleaning and self-sterilizing surfaces, solar cells and hydrogen production from water dissociation reaction. Since the discovery of photo-electrochemical splitting of water by titanium dioxide electrode under ultraviolet light by Fujishima and Honda in 1972 (Fujishima and Honda 1972), titanium dioxide has become the state-of-the-art material for photocatalytic reactions due to its relatively high efficiency under UV irradiation, abundance, low cost, photo-corrosion resistance and biocompatibility. Although titanium dioxide can be used in powder form for some applications, its immobilized form (film) is necessary for many applications including but not limited to self-cleaning and bactericidal surfaces (Sunada, Kikuchi et al. 1998; Allain, Besson et al. 2007), anti-fogging glasses (Wang, Hashimoto et al. 1997), and advanced filters (Lee, Behler et al. 2010). In particular, titanium dioxide coated self-cleaning glasses (e.g. Pilkington Activ™, Saint-Gobain Bioclean™, PPG SunClean™) have become commercially successful. Considering the architectural trends for larger windows and the difficulties to clean windows in high-rise buildings, high efficiency self-cleaning glasses will become more important. Thus, it is important to fully evaluate and optimize the photocatalytic efficiency of titanium dioxide films on glass, since glass items will most likely form the majority of the substrates to be used widely.

Being a wide-band gap semiconductor, titanium dioxide films can utilize only a limited (ultraviolet) portion of the solar spectrum which limits its efficiency under solar irradiation. It is because of this limitation that the utilization of titanium dioxide films for indoor applications is extremely limited. Extending the absorption to the visible range requires the modification of the underlying electronic structure (or so-called band gap engineering) of titanium dioxide which is closely related to its chemical composition and the corresponding atomic arrangements. Therefore, doping of titanium dioxide is an indispensable way to produce favorable changes in the electronic structure while keeping the integrity of the original crystal structure. Density Functional Theory (DFT), in this respect, is an incredibly useful method to analyze and shed light on the doping process and its effect on the electronic structure. Thanks to the dramatically increased processing powers and more efficient software codes that can implement parallel computation techniques, performing such calculations is significantly easier compared to the case just a decade ago.

Several methods have been reported for the preparation of TiO_2 films: sol-gel (Brinker, Hurd et al. 1992), chemical vapor deposition (Mills, Elliott et al. 2002), magnetron sputtering (Takeda, Suzuki et al. 2001), spray pyrolysis (Abou-Helal and Seeber 2002), direct deposition (Shimizu, Imai et al. 1999) and layer-by-layer coating (Lee, Rubner et al. 2006). In particular, sol-gel is an attractive method because of the capability to coat materials with various shapes and ease of control over the composition of the films with relatively simple and inexpensive equipment (Brinker, Hurd et al. 1992).

In many cases, good mechanical integrity needs to be coupled with good photocatalytic and optical properties in order to achieve sufficient lifetime of the coatings, since their functionalities can be lost if the films are deteriorated due to wear or environmental degradation.

1.2. Heterogeneous Photocatalysis

Heterogeneous photocatalysis is the catalysis of a reaction in which the catalyst is activated by photons. Classical heterogeneous catalysis involves five steps (Herrmann 1999):

- Transfer of reactants in the fluid phase to the catalysts surface
- Adsorption of the reactant(s)
- Reaction of the reactant(s) on the catalyst surface
- Desorption of the product(s)
- Removal of products from the interface region

Overall, a photocatalytic reaction can be summarized as follows (Carp, Huisman et al. 2004):

$$(Ox_1)_{ads} + (Red_1)_{ads} \xrightarrow{photocatalyst+h\nu} (Ox_2)_{ads} + (Red_2)_{ads}$$

In practice, photocatalytic reactions typically take place in aqueous environments and in case of titanium dioxide (TiO_2) as the photocatalyst, are composed of four steps (Kabra, Chaudhary et al. 2004):

(i) Activation of the photocatalyst by photon energy greater than its band gap (3.2 eV for titanium dioxide) which generates electron-hole couples:

$$TiO_2 \xrightarrow{h\nu \geq 3.2eV} e^- + h^+$$

(ii) Adsorption of the compound (to be oxidized – R_1) on the catalyst surface and the lattice oxygen (O_L^{2-}):

$$O_L^{2-} + Ti^{IV} + H_2O \rightarrow O_LH^- + Ti^{IV} - OH^-$$

$$Ti^{IV} + H_2O \rightarrow Ti^{IV} - H_2O$$

$$site + R_1 \rightarrow R_{1ads}$$

(iii) Recombination of some of the carriers generated in the step (i) to produce heat:

$$e^- + h^+ \rightarrow heat$$

(iv) Trapping of the carriers on the catalyst surface:

$$Ti^{IV} - OH^- + h^+ \rightarrow Ti^{IV} - OH^\bullet$$

$$Ti^{IV} - H_2O + h^+ \rightarrow Ti^{IV} - OH^\bullet + H^+$$

$$R_{1ads} + h^{+} \rightarrow R_{1ads}^{+}$$

$$Ti^{IV} + e^{-} \rightarrow Ti^{III}$$

$$Ti^{III} + O_2 \rightarrow Ti^{IV} - O_2^{\bullet -}$$

(v) Oxidation of the adsorbed compound (R_{1ads})

$$Ti^{IV} - OH^{\bullet} + R_{1ads} \rightarrow Ti^{IV} + R_{2ads}$$

$$OH^{\bullet} + R_{1ads} \rightarrow R_{2ads}$$

$$Ti^{IV} - OH^{\bullet} + R_1 \rightarrow Ti^{IV} + R_2$$

$$OH^{\bullet} + R_1 \rightarrow R_2$$

Step (i) is the first important step that the efficiency of the photocatalyst is dependent on the wavelength and intensity of the illumination source. Activation of the photocatalyst only takes place with photons having energies larger than the band gap of the photocatalyst (3.2 eV for TiO_2). Figure 1.1 shows the portion of the solar spectrum that titanium dioxide can absorb. Integration of the data shows that titanium dioxide can only absorb 2.5% of the solar spectrum whereas a relatively modest shift of 0.5 eV can increase the absorption to 8.0%. Accordingly, successful band gap engineering is extremely important as minor gains in the band gap shift will bring exponential gains in performance. Similarly, lack of UV light is the biggest obstacle against use of photocatalyst under indoor lighting conditions.

Another important parameter in the photocatalytic activity is the intensity of the irradiation source. Three regions exist for the photocatalytic reaction rate with respect to UV-light intensity (Ollis, Pelizzetti et al. 2002). In the low intensity region, an increase in the light intensity brings a linear increase in the photocatalytic reaction rate (first-order). At intermediate levels, the reaction rate increases with the square root of illumination intensity. At significantly higher intensity levels reaction rate decreases with the square root of intensity. The behavior can be explained by the increased recombination rate at high intensity levels due to the decreased trapping of carriers by adsorbed chemicals (Ollis, Pelizzetti et al. 2002; Wang, Chiang et al. 2003; Carp, Huisman et al. 2004).

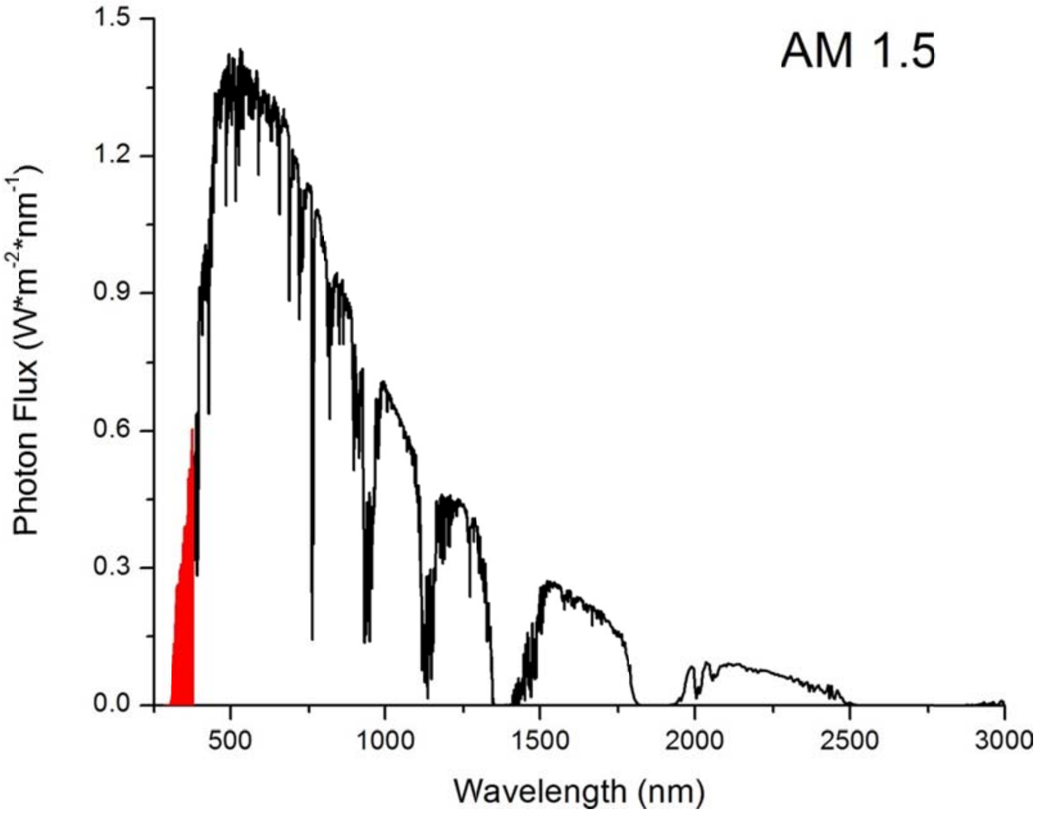

Figure 1-1: Intensity of sunlight versus wavelength for AM 1.5 conditions (ASTM 2008). The filled area shows the part of the spectrum that can be absorbed by titanium dioxide.

Step (ii) is determined by the compound to be adsorbed, its concentration, pH of the solution, and the number of available adsorption sites on the catalyst surface. An analysis of the photocatalytic degradation of methylene blue, a model pollutant, by titanium dioxide has shown that adsorption is of the Langmuirian type and the behavior is given by (Houas, Lachheb et al. 2001):

$$\frac{1}{n_{ads}} = \frac{1}{n_0} + \left(\frac{1}{n_0 K}\right)\frac{1}{C}$$

where n_0, n_{ads}, K and C are the number of adsorption sites, number of sites adsorbed, adsorption constant and concentration, respectively. Since n_0 is a function of surface area, small size (high surface area) catalysts adsorb more compound which results in higher photocatalytic activities. This is one of the shortcomings of an immobilized photocatalyst (thin film), which inherently has a smaller surface area compared to powders. Another important parameter is the adsorption constant K of the compound, which, other parameters being equal, is strongly dependent on the pH of the solution. pH of the solution influences the surface state of the photocatalyst and the ionization of the molecules to be adsorbed. Titanium dioxide, for example, has a point of zero charge (PZC) around pH 6, above which its surface is negatively charged and positively charged below according to the following equilibria (Lachheb, Puzenat et al. 2002):

$$pH < 6 : Ti - OH + H^{+} \Leftrightarrow TiOH_2^{+}$$

$$pH > 6 : Ti - OH + OH^{-} \Leftrightarrow TiO^{-} + H_2O$$

Thus, adsorption of cationic and anionic dyes is favored at pH values above and below the PZC of catalyst, respectively.

Step (iii) is the dominant step that more than 95% of the charge carriers recombine before taking a role in the chemical reaction. Electron-hole recombination can take place in the bulk or on the surface and the kinetics of these processes determine the efficiency of the photocatalyst. For example, anatase has shown to possess a much higher donor state radius compared to rutile, due to its lower electron effective mass which contributes to lower recombination rates thence to higher photocatalytic activity (Tang, Prasad et al. 1994).

Step (iv) involves the trapping of holes and electrons on the catalyst surface. Number of trap centers is important and strongly influences the recombination rate. It is indeed, the competition between charge-carrier recombination and trapping (step (iii) and step (iv)) that determines the overall quantum efficiency of a photocatalyst. Anatase phase of titanium dioxide, for example; possess strong hole trapping sites on the surface which results in higher lifetime of the carriers compared to rutile phase and this results in anatase being a better photocatalytic material than rutile (Colbeau-Justin, Kunst et al. 2003).

Step (v) describes the possible cases of photocatalytic oxidation. Oxidation of the compounds occurs directly by holes on the surface or indirectly by the attack of hydroxyl radicals generated by photocatalysis. There are a significant number of studies claiming either of the cases as the principle mechanism. Lawless et al. have studied the reaction of hydroxyl radicals generated by pulse radiolysis with titanium dioxide particles and concluded that surface trapped holes were responsible for the majority of oxidation reactions whereas free hydroxyl radicals play only a minor role at most (Lawless, Serpone et al. 1991). On the other hand, Daneshvar et al. have shown that addition of ethanol, a hydroxyl radical quencher, strongly inhibits the photocatalytic oxidation of an azo dye in aqueous solution and concluded that hydroxyl radicals, indeed play a significant role in the photocatalytic oxidation reactions (Daneshvar, Salari et al. 2003).

Presence of an electron acceptor is also necessary to preserve the charge balance of the photocatalyst. The most common electron acceptor for photocatalytic reactions is dioxygen species, which is reduced by conduction band electrons of titanium dioxide forming hydrogen peroxide according to the following mechanism (Hoffmann, Martin et al. 1995):

$$Ti^{IV}O_2^{\bullet -} + H_3O^+ \rightarrow Ti^{IV}OH_2 + HO_2^{\bullet}$$

$$2HO_2^{\bullet} + 2H^+ \rightarrow H_2O_2 + O_2$$

Hydrogen peroxide generated by the above reactions can either act as a more efficient alternative electron acceptor to dioxygen or split into hydroxyl radicals (Cater, Stefan et al. 2000; Daneshvar, Salari et al. 2003).

Characteristic times for some of the steps described above are summarized in Table 1-1 (Hoffmann, Martin et al. 1995).

Table 1-1: Primary processes and associated characteristic time domains of titanium dioxide photocatalysis steps (Hoffmann, Martin et al. 1995).

Process	**Characteristic Times**
Step (i): *electron-hole generation*	fs
Step (iii): *electron-hole recombination*	10 – 100 ns
Step (iv): *electron-hole trapping*	0.1 – 10 ns
Step (v): *interfacial charge transfer*	100 ns - ms

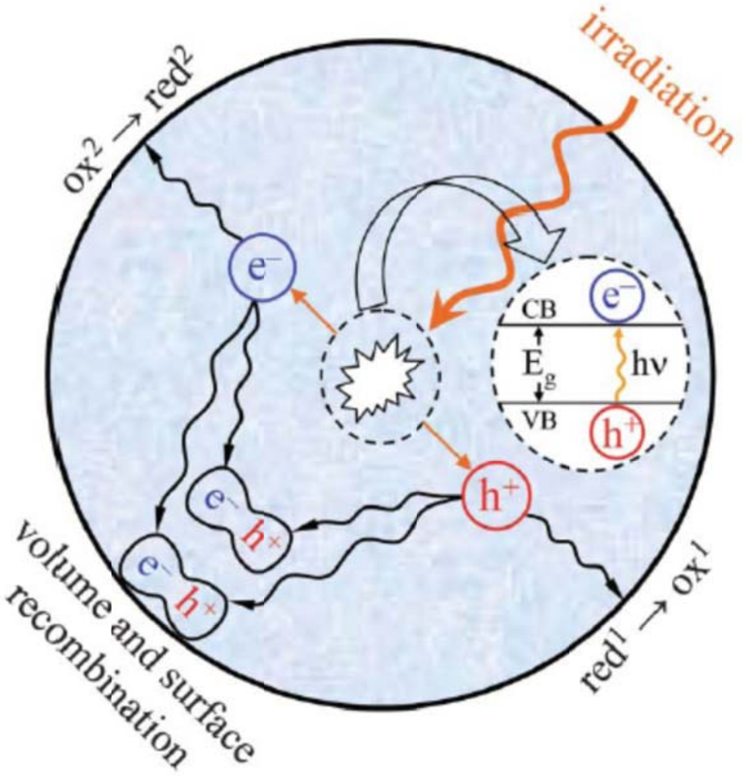

Figure 1-2: Schematics of the bulk and surface electron-hole dynamics of a photocatalytic particle. Electrons reaching to the surface either recombine on the surface or reduce an adsorbed electron acceptor (e.g. dissolve oxygen). (Palmisano, Augugliaro et al. 2007)

1.2.1. Applications

Heterogeneous photocatalysis is utilized in a variety of applications and reactions: air and water purification, self-cleaning coatings (Paz, Luo et al. 1995), self-sterilizing surfaces (Fu, Vary et al. 2005), dehydrogenation, hydrogen transfer, metal deposition etc.

1.2.1.1. Water Purification

Around 2 million people die each year due to the sicknesses acquired by ingestion of contaminated water, lack of sanitation and bad hygiene practice (WHO). According to The Water Project, Inc., a non-profit organization, nearly one billion people don't have safe water to drink. Titanium dioxide photocatalysis has been suggested as a promising way to purify water by sunlight amid growing demand for effective, economic and environmentally friendly water treatment technologies. Photocatalytic water purification has the following advantages (Carp, Huisman et al. 2004):

- In contrast to chlorination/ozonation, photocatalytic water purification can remove virtually all kinds of contaminants even at very low concentrations
- It does not produce harmful by-products (as opposed to chlorination, which produces potential carcinogens such as trihalomethanes)
- The use of oxygen as the only oxidant

There are still problems that need to be addressed before applications of photocatalytic water purification can become a viable alternative to chlorination and ozonation. These are mainly:

- Lack of a visible-light active photocatalyst
- Need for increased efficiency of the current photocatalysts
- Recovery of the photocatalyst

The first two of the problems can be solved by effectively modifying the electronic structure of the current photocatalysts whereas the last one can be remedied by immobilizing the photocatalyst, though this comes at the expense of losing some of surface area.

1.2.1.2. Self-cleaning coatings

Although titanium dioxide performs very efficiently in its powder form, an immobilized form is necessary for most practical applications. Being a wide band gap semiconductor, titanium dioxide is transparent, thus allowing its use as a thin film on a variety of surfaces without degrading the aesthetic view. Following the first demonstration of self-cleaning concept on titanium dioxide coated ceramic tiles by Hashimoto et al. in 1992, several commercial applications have emerged by large such as TOTO, Pilkington, PPG, Saint-Gobain, AFG etc.

Self-cleaning effect by photocatalytic titanium dioxide coating on a glass window is explained in Figure 1-3. When titanium dioxide is illuminated by UV light (solar illumination), it starts decomposing contaminants to minerals and carbon dioxide. At the same time, titanium dioxide becomes superhydrophillic and it retains this property for a while after illumination ceases. This enables the easy washing (typically by rain) of stains adsorbed on the titanium dioxide surface as water penetrates to the molecular-level space between the stain and titanium dioxide surface.

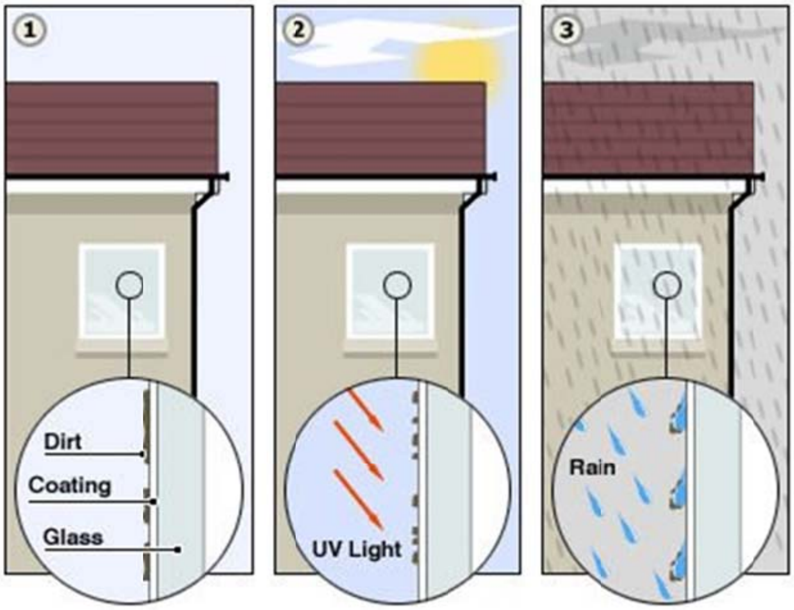

Figure 1-3: Schematics of the self-cleaning effect on a titanium dioxide coated window glass. (1) Dirt particles on the titanium dioxide film is (2) decomposed to inorganic minerals by the photocatalytic action induced by solar irradiation and (3) removed from the surface by rain water penetrating between the dirt and superhydrophillic film.

1.2.1.3. Antimicrobial Surfaces

Photocatalytic oxidation ability of titanium dioxide has been utilized in self-sterilizing surfaces which can be particularly useful in public areas where sterile conditions are important such as hospitals, hotels, restaurants etc. The passive operation of such surfaces removes the need for continuous care with cleaning agents and disinfectants, thus decreases the amount of environmental pollution. On the other hand, tiny fraction of ultraviolet light available indoors significantly limits the antimicrobial activity of titanium dioxide surfaces. In order to solve this problem, several other antimicrobial elements such as silver, copper and zinc are typically added to titanium dioxide films to collectively increase the antimicrobial activity. Some of the pathogenic organisms that are shown to be killed by photocatalytic titanium dioxide are Escherichia coli, Salmonella choleraesuis, Bacillus subtilis, Poliovirus 1.

1.2.1.4. Other Applications

There are several other application areas that titanium dioxide photocatalysis has been used (Carp, Huisman et al. 2004):

- Selective synthesis of organic compounds
- Anti-fogging materials
- Dehydrogenation

1.3. Photocatalytic Materials

There are several materials known for their photocatalytic activity of which most of them are metal oxides. Since the discovery of its photocatalytic effect by Honda and Fujishima in 1978, titanium dioxide has become the most popular photocatalytic material due to its abundance, low cost, chemical stability, biocompatibility and high efficiency under UV light.

Though not as popular as titanium dioxide, zinc oxide has been getting increasing attention as a photocatalytic material due to its similar electronic structure and catalytic efficiency. While zinc oxide can be a more efficient photocatalyst in near UV excitations compared to titanium dioxide, it has the problem of photo-corroding itself, limiting its wide use (van de Krol, Liang et al. 2008).

There are several other photocatalytic materials which have been investigated such as Fe_2O_3, CdS, MoS_2, WO_3, $SrTiO_3$. Photocatalytic activities of some of the materials investigated are shown in Figure 1-4.

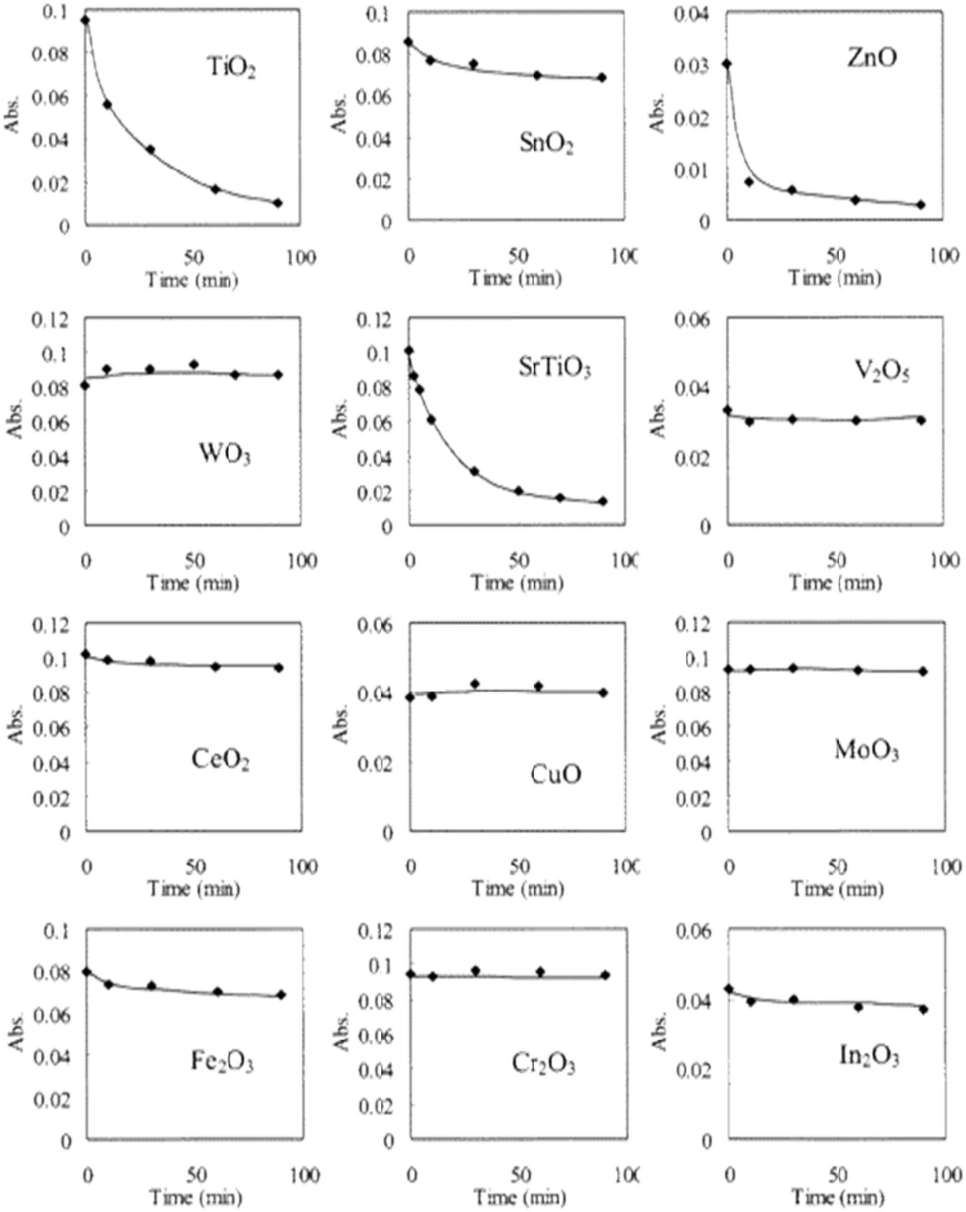

Figure 1-4: Relative photocatalytic activity of several oxides (Miyauchi, Nakajima et al. 2002). Total amount of dye adsorbed on the oxide vs. illumination time is given. TiO_2, ZnO and $SrTiO_3$ are highly active. SnO_2, Fe_2O_3 and In_2O_3 showed slight photocatalytic activity. V_2O_5, CeO_2, CuO, MoO_3 and Cr_2O_3 did not show any photocatalytic activity.

1.4. Titanium Dioxide

1.4.1. Structure

Titanium is the ninth most abundant element on earth's crust. Most common mineral sources of titanium are rutile (93-96% TiO_2), ilmenite (44-70% TiO_2) and leucoxene (60-90% TiO_2) (Figure 1-5).

Figure 1-5: Titanium dioxide mineral sources: (a) rutile, (b) ilmenite and (c) leucoxene.

Most of the mineral concentrates are located in Australia, Canada and South Africa. World production levels of titanium ores have seen an increase over the last decade although a sharp decrease was observed due to the global economic recession (Figure 1-6) (2009). Despite the fact that titanium is extremely corrosion resistant and has the highest strength-to-weight ratio of any metal (Donachie 1988), only 1-2% of the imported ore in the US is used for making titanium metal whereas the rest is used for titanium dioxide production where the majority of which is utilized as white pigment (2009).

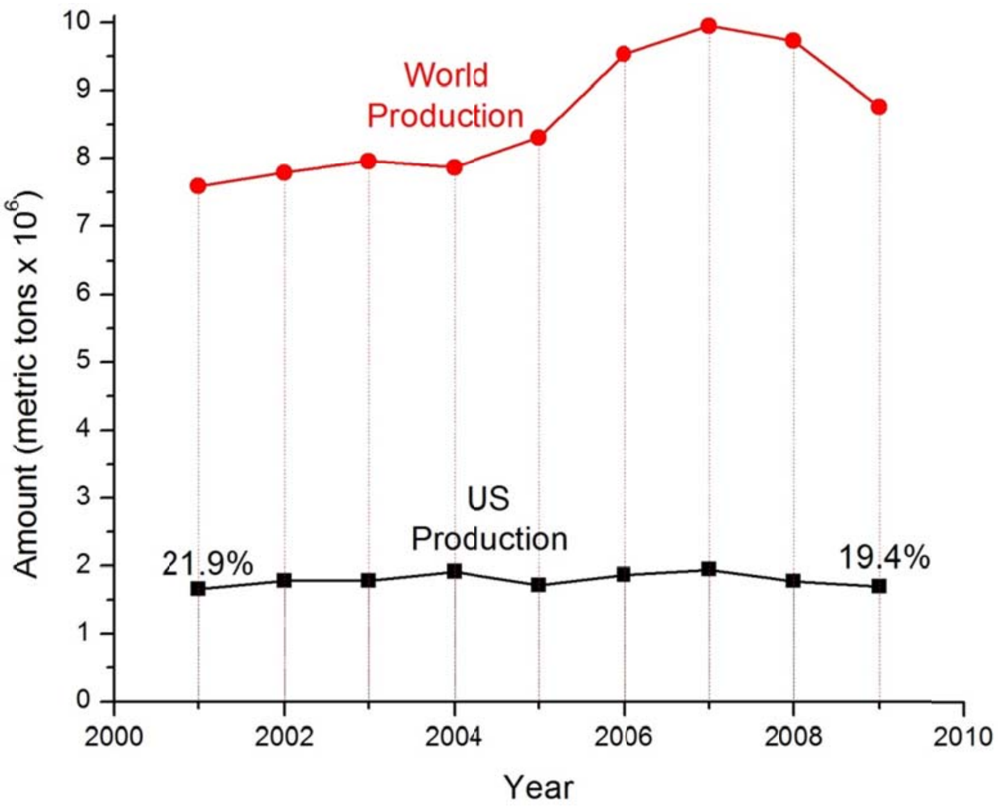

Figure 1-6: World and US titanium ore production amounts vs. year.

Titanium forms several oxides: TiO, Ti_2O_3, Magneli phases (Ti_3O_5, Ti_4O_7 etc.), TiO_2. Titanium dioxide (TiO_2) is the most stable oxide of titanium oxides in air and has three well-known phases: anatase, rutile and brookite. Crystal structure of all forms (Figure 1-7) can be defined by (TiO_2^{6-}) octahedrals where individual phases differ by the distortion of each octahedral the way they are assembled. Octahedrals are connected by their vertices, edges and vertices and edges in anatase, rutile and brookite, respectively. The less common phases of titanium dioxide are TiO_2 (B), TiO_2 (II) and TiO_2 (H).

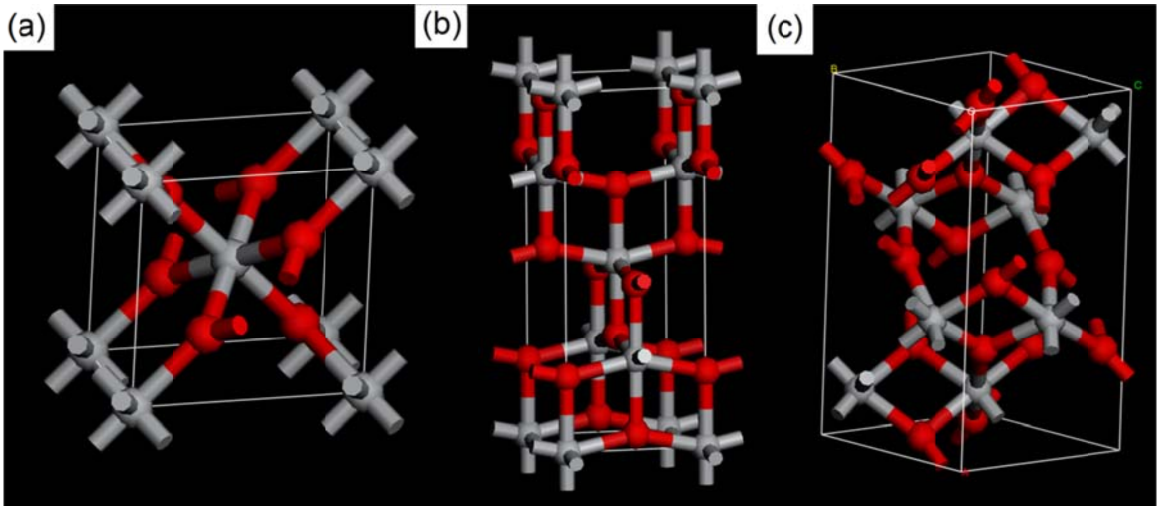

Figure 1-7: Crystal structure of the most common phases of titanium dioxide: (a) rutile, (b) anatase and (c) brookite.

Rutile is the thermodynamically most stable phase of titanium dioxide although the differences in the Gibbs free energy of formation between the three phases are relatively small. Because of this reason, surface energy contributions are so significant that relative stability of titanium dioxide phases are strongly affected by the particle size (Zhang and Banfield 1998). According to the thermodynamic calculations reported by Zhang et al., stability of titanium dioxide phases are defined by particle size regions in which anatase is the most stable phase below 11 nm, brookite is the most stable phase between 11 nm and 35 nm and rutile is the most stable phase above 35 nm (Zhang and Banfield 2000).

1.4.2. Electronic Structure

Titanium dioxide is an n-type semiconductor with a band gap of 3.0 eV, 3.1 eV and 3.2 eV for rutile, brookite and anatase, respectively. n-type behavior arises due to oxygen vacancies and creation of Ti^{3+} sites, which are also responsible for the observed electronic conductivity. Density of states (DOS) of titanium dioxide is composed of Ti e_g, Ti t_{2g} (d_{yz}, d_{zx}, d_{xy}), O p_σ and O p_π (Figure 1-8) (Asahi, Taga et al. 2000). Overall, valence band is composed of O-related states whereas conduction band is composed of Ti-related states. Anatase possesses a narrower 3d band compared to rutile which is due to the localization of Ti 3d states as Ti –Ti distances are larger in anatase (Di Valentin, Pacchioni et al. 2004).

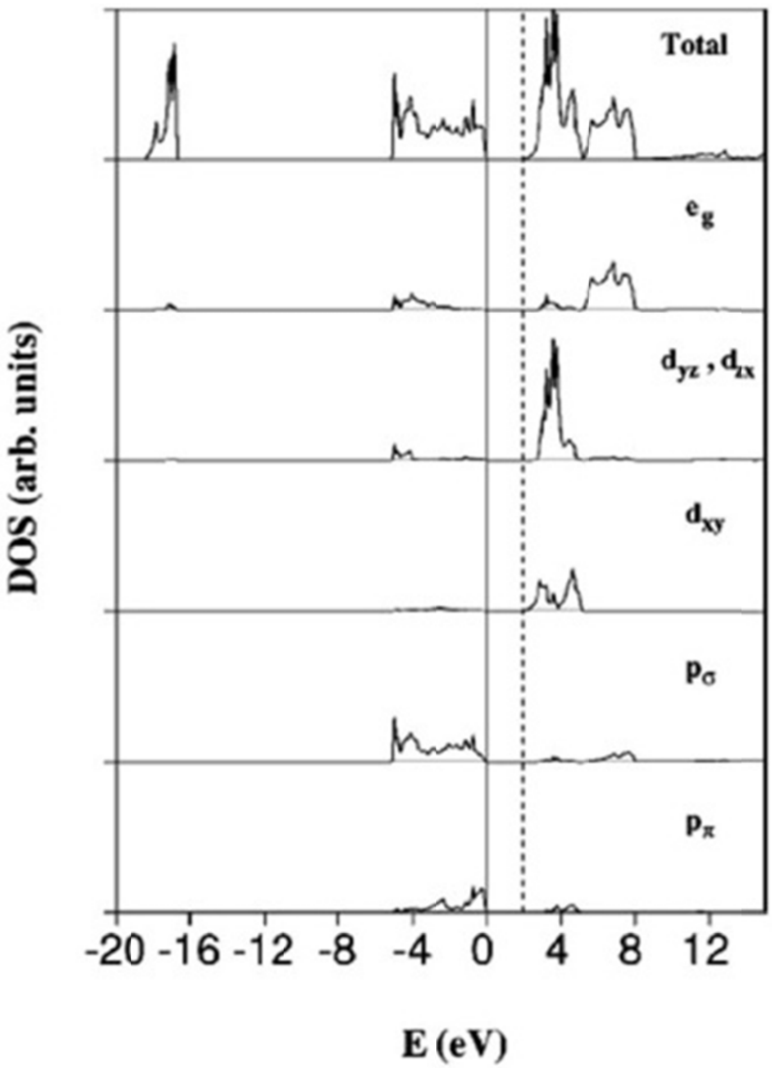

Figure 1-8: Density of states (DOS) plot of titanium dioxide (anatase).

Contrary to other semiconductors, quantum-size effect is rarely seen in titanium dioxide particles since such effect can be seen only particles below 2 nm (Satoh, Nakashima et al. 2008).

A study to investigate the carrier dynamics of anatase and rutile has shown that the latter has a faster photoconductivity decay which is explained by the surface trapping of holes in anatase and high recombination rate of rutile (Colbeau-Justin, Kunst et al. 2003).

1.4.3. Production Methods

Titanium dioxide can be prepared in the powder and film forms.

1.4.3.1. Powders

Titanium dioxide powders are prepared by precipitation of titanium hydroxides followed by calcination, hydro/solvo-thermal processes, sol-gel method and spray pyrolysis.

1.4.3.2. Films

There are various methods to produce titanium dioxide films. The methods can be divided into two major routes: solution based and gas phase methods. Solution based methods include hydro/solvo-thermal processing, sol-gel methods, layer-by-layer process and electrochemical synthesis. Gas phase methods include chemical and physical vapor deposition, spray pyrolysis deposition, sputtering and molecular beam epitaxy.

1.4.3.2.1. Hydro/Solvo-Thermal Synthesis

These methods include the various techniques of crystallizing titanium dioxide particles at high temperatures and vapor pressures in aqueous (hydrothermal process) or organic (solvothermal process) solutions. These methods allow in situ formation of stable, transparent crystalline titanium dioxide particle dispersions, which is quiet difficult to achieve with already crystallized titanium dioxide particles. Obtained dispersions can be used to deposit titanium dioxide films on substrates with low temperature resistance especially since a calcination treatment for crystallization is not necessary. On the other hand, an efficient wetting of the substrate may require a binder such as silica followed by a low temperature annealing step.

1.4.3.2.2. Sol-Gel

Sol-gel process is undoubtedly the most popular process for the synthesis of titanium dioxide films owing to its simplicity, low-cost, ease of composition control. Sol-gel process involves the generation of colloidal suspensions ("sol") which are subsequently converted to viscous "gels" and to solid materials (Wright and Sommerdijk 2001).

In a typical sol-gel process, a titanium dioxide precursor (usually an alkoxide, and an inorganic salt occasionally) forms a sol by hydrolysis and polymerization reactions followed by completer polymerization and loss of solvent to form a gel. Hydrolysis reaction involves the replacement of alkoxide groups (OR) with hydroxyl groups (OH):

$$\equiv Ti - OR + H_2O \rightleftharpoons \equiv Ti - OH + ROH$$

Condensation process produce Ti – O – Ti bonds plus byproducts of alcohol or water:

$$\equiv Ti - OR + HO - Ti \equiv \rightleftharpoons \equiv Ti - O - Ti \equiv + ROH$$

$$\equiv Ti - OH + OH - Ti \equiv \rightleftharpoons \equiv Ti - O - Ti \equiv + H_2O$$

Prepared sol can subsequently be used for thin film deposition by dip-coating or spin-coating. Dip coating consists of five stages: immersion, start-up, deposition, drainage, and evaporation (Figure 1-9). There are six forces that dictate the deposited film thickness by the dip coating (Brinker and Scherer 1990):

- Viscous drag upward on the liquid by the moving substrate
- Gravitational force
- Force due to surface tension in the concavely curved meniscus
- Inertial force of the boundary layer liquid arriving at the deposition region
- Disjoining and conjoining pressure

Landau and Levich formulated the relationship between dip coating parameters and thickness of the resulting film:

$$h = 0.94 \cdot \left(\frac{\eta U}{\gamma_{LV}} \right)^{1/6} \left(\frac{\eta U}{\rho g} \right)^{1/2}$$

Where h is the thickness of the film, η is the viscosity of the sol, U is the withdrawing speed of the substrate, γ is the liquid-vapor surface tension, ρ is the density of the sol and g is the gravitational constant. It can be deduced form the formula that thicker films can be obtained by higher withdrawing speeds of the substrate from a high viscosity sol.

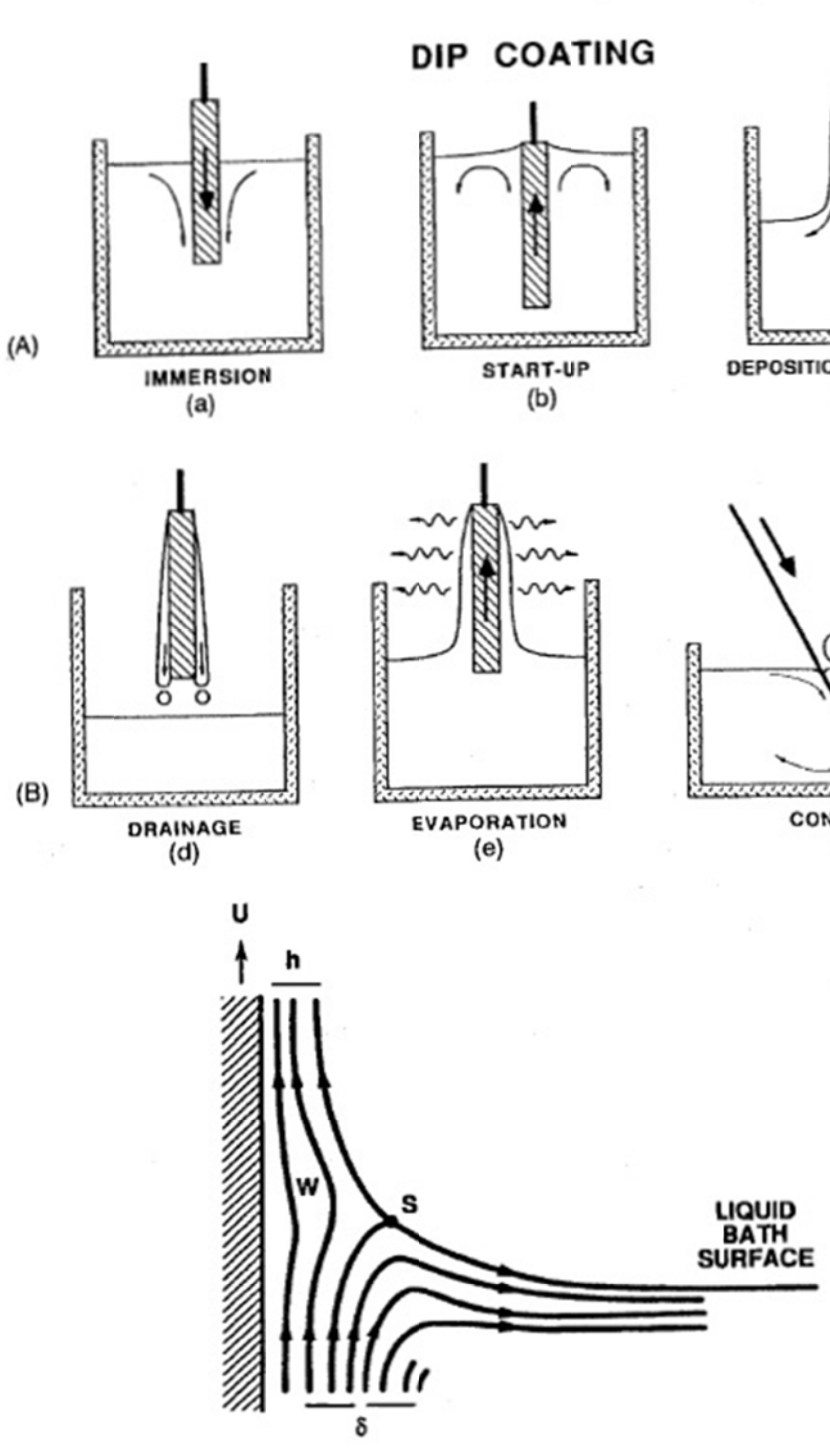

Figure 1-9: (A) Stages of dip coating process: (a-e) batch; (f) continuous. (B) Detail of the liquid flow patterns in area 3 of the continuous process. U is the withdrawal speed, S is the stagnation point, δ is the boundary layer and h is the thickness of the liquid film (Brinker and Scherer 1990).

Evaporation is the most important step following the dipping and withdrawing process that it is relied upon to solidify the coating. The rate of evaporation depends strongly on the rate of diffusion of the vapor away from the surface which is related to the movement of gas within a very thin layer (≈ 1 mm) due to the substantial effect of convection (Brinker and Scherer 1990).

Obtaining a solid film by dip-coating requires gelation of the deposited sol on the substrate which is driven by the polymerization of the inorganic precursor. Figure 1-10 shows the schematics of the steady-stage deposition stage of the dip coating process.

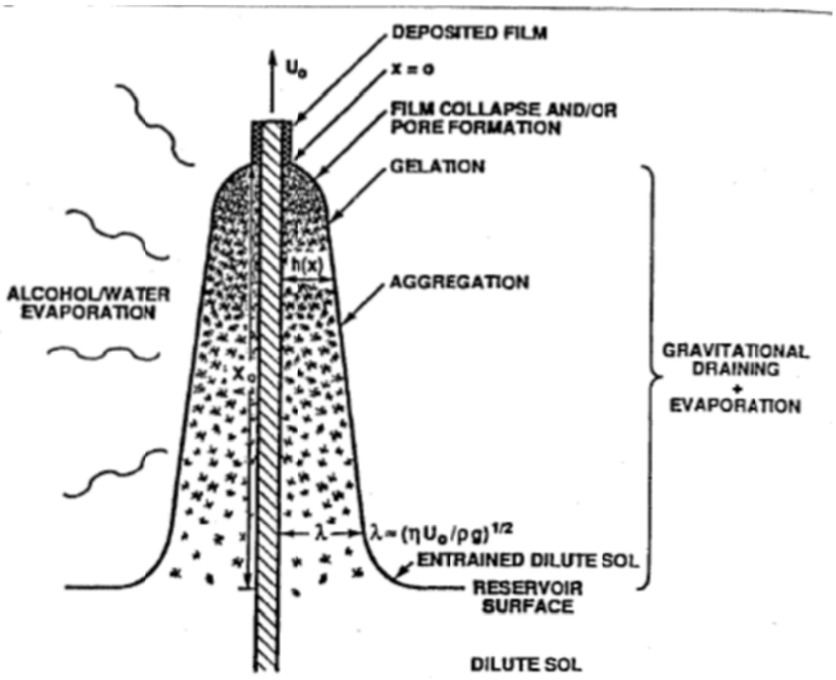

Figure 1-10: Schematics of the steady-state deposition stage of the dip-coating process (Brinker and Scherer 1990).

As-prepared titanium dioxide films are typically amorphous and contain significant amount of organic impurities, thus they need a calcination step between 200°C and 1000°C.

1.4.4. Mechanical Properties of Titanium Dioxide Films

Despite its well investigated photochemical, electrical (Tang, Prasad et al. 1994) and optical properties (Cao, Oskam et al. 1995; Mardare and Hones 1999), mechanical properties of TiO_2 films have been much less studied. However, mechanical durability of the thin films is one of the most important parameters that make their application feasible, especially when coatings are exposed to the open air environment and experience erosion wear and damage. There has been very limited amount of nanoindentation studies to understand the key mechanical properties such as hardness and modulus of titanium dioxide films.

1.4.5. Improving Photocatalytic Activity of Titanium Dioxide Films

After decades of search for a better photocatalyst, titanium dioxide has proved to be difficult to beat; there is still not a better alternative to titanium dioxide owing to its high efficiency, low-cost, abundance, chemical resistance and biocompatibility. On the other hand, there are very important problems and shortfalls of titanium dioxide which need to be addressed for successful applications. The most important problems are the lack of visible-light activity and dramatic loss of surface area when prepared in film form (which is the problem of all catalysts) and the deteriorative effect of the substrate (most ceramic substrates).

1.4.5.1. Visible-Light Photocatalytic Activity

Being a wide-band gap semiconductor, titanium dioxide can only absorb a tiny fraction of solar irradiation (<5%) which significantly limits its applications, especially for indoor applications. Several approaches have been tried to overcome this limitation. The most prominent of them are doping with other elements (Nie, Zhuo et al. 2009), sensitizing with other compounds or semiconductors, preparing oxygen-deficit titanium dioxide and coupling with plasmonic noble metal nanoparticles. In particular, doping approach has taken the majority of the attention due to its promising results and potential. A variety of metals have been doped into titanium dioxide with some limited success. Borgarella et al. reported visible light induced water cleavage in colloidal solutions of chromium-doped titanium dioxide nanoparticles (Borgarello, Kiwi et al. 1982). In a similar study, photocatalytic oxidation of water by ruthenium-doped titanium dioxide powders under visible light (Ohno, Tanigawa et al. 1999). Other metals reported include silver (Seery, George et al. 2007), iron (Chatterjee and Dasgupta 2005), vanadium (Klosek and Raftery 2001) and cobalt (Iwasaki, Hara et al. 2000).

1.4.5.2. Substrate Effect

Since it is not a strong optical absorber, titanium dioxide is particularly suitable for coating transparent materials such as glass without sacrificing the optical properties of the substrate. However, photocatalytic activity of titanium dioxide films is strongly dependent on the underlying substrate due to the possible chemical interaction between titanium dioxide and the substrate material during high temperature calcination treatment (Hattori, Shimoda et al. 1999; Nam, Amemiya et al. 2004). For example, sodium is known to diffuse into sol-gel prepared films during calcination and degrade their photocatalytic activity (Paz, Luo et al. 1995; Nam, Amemiya et al. 2004; Xie and Lin 2007). Degradation of photocatalytic activity by sodium diffusion has been explained by the increased particle size (Nam, Amemiya et al. 2004), formation of catalytically inactive sodium titanates (Fujishima and Rao 1997), formation of recombination centers (Paz, Luo et al. 1995), and suppressed crystallization (Lee and Lee 2007). Yu et al. have shown that photocatalytic activity of titanium dioxide films on glass can be improved by a surface post-treatment in sulphuric acid (Yu, Yu et al. 2002). Although not ruling out other mechanisms, this finding clearly shows that creation of recombination centers by sodium is a very important contributor to the deterioration of photocatalytic activity. While the exact mechanism is still under debate, sodium is clearly a catalytic poison. Pre-coating the glass substrate with a sodium blocking layer such as silicon dioxide (SiO_2) or post-treatment in acidic media have been shown to improve photocatalytic activity of titanium dioxide films (Yu and Zhao 2000; Yu and Zhao 2001; Yu, Yu et al. 2002). However, these methods are still imperfect in that all of them require additional processing steps which would be costly for many practical applications. Therefore it is important to find a feasible solution to circumvent the need for these additional steps.

1.4.5.3. Surface Area of Thin Films

A significant reduction in the surface area accompanies film formation which results in the resulting low photocatalytic activity of titanium dioxide films compared to its powder form. Since an immobilized form (films) is necessary for most practical applications, there is an increased need to overcome the low surface area problem. Several solutions have been proposed: formation of porous films by phase separation and methods like evaporation-induced self-assembly (Lu, Ganguli et al. 1997), in situ formation of titanium dioxide nanotubes on titanium metal by electrochemical methods (Paulose, Shankar et al. 2006) and using high surface area templates (Lakshmi, Dorhout et al. 1997).

1.5. Conclusions

The investigation and optimization of titanium dioxide films are of significant importance from scientific and practical points of view. While doping of titanium dioxide <u>powders</u> has been investigated by several research groups in the past, a systematic study of doping of titanium dioxide <u>films</u> is still lacking. In many practical applications, immobilization of titanium dioxide, typically in the form of a thin film, is necessary and the underlying mechanism and the aftereffects of doping process on the film structure is different than powder forms due to strong interaction of the former with the underlying substrate given the fact that catalytic supports have dramatic effect on the performance and selectivity of the catalyst. Although there is a countless amount of possibilities for the substrate, typical usage area of photocatalytic materials suggests that the substrate is most likely a silica-based glass, especially since the majority of the already commercialized photocatalytic coatings are either deposited on soda-lime glasses or on ceramic tiles which are covered with silica-based glazes. Thus, investigating the effects of doping of titanium dioxide films on glass substrates are of utmost importance.

It is important to complement experimental studies with theoretical calculations to understand the underlying mechanism of doping process to develop better photocatalysts in the future. However, research on the doping of titanium dioxide for photocatalytic applications are so far focused either on the experimental trial-and-error methods or on purely theoretical calculations but rarely both.

OBJECTIVES

- Study the fundamental sol-gel film synthesis parameters such as calcination temperature and heating rate on the structural, photocatalytic and mechanical properties of undoped titanium dioxide films to develop a guideline for future experiments
- Model and simulate the doping process with Density Functional Theory (DFT) to understand the thermodynamic cost of doping and its effects on the electronic structure of the anatase structure
- Evaluate the effect of reductive calcination atmospheres at a wide range of calcination temperatures on the photocatalytic (UV and particularly visible light), structural and mechanical properties of titanium dioxide films
- Produce a wide range of metal doped titanium dioxide films on glass substrates and study the effects of individual dopants on the substrate-film interaction, optical, photocatalytic and mechanical properties on such films
- Investigate the photocatalytic (visible and UV) and mechanical properties of nitrogen-doped titanium dioxide films with respect to nitrogen dopant concentration
- Evaluate the efficiency of a wide-range of metal co-dopants on the photocatalytic and mechanical properties of nitrogen-doped titanium dioxide films

CHAPTER 2) MATERIALS AND METHODS

2.1. Materials

2.1.1. Titanium precursors

Titanium dioxide films were produced from a variety of precursors: titanium (IV) isopropoxide -$Ti[OCH(CH_3)_2]_4$-, titanium (IV) butoxide –$Ti(OCH_2CH_2CH_2CH_3)_4$-, titanium (IV) chloride –$TiCl_4$- (Figure 2-1). Precursors were used in the as-received state.

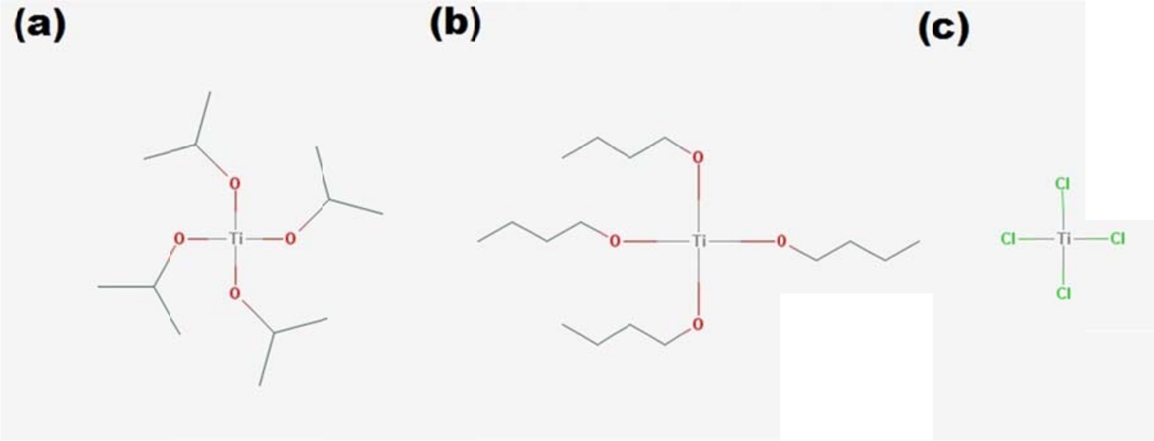

Figure 2-1: Titanium dioxide precursors: (a) titanium (IV) isopropoxide, (b) titanium (IV) butoxide, (c) titanium (IV) chloride.

2.1.2. Solvents

Various solvents were used for the generation of titanium dioxide sols: ethanol (C_2H_5OH, Sigma-Aldrich, 200 proof), 2-propanol ($(CH_3)_2CHOH$, Sigma-Aldrich, 99.5%), 1-butanol ($CH_3(CH_2)_3OH$, Sigma-Aldrich, 99.8%), N,N-dimethylformamide ($HCON(CH_3)_2$, Sigma-Aldrich, 99.8%), dichloromethane (CH_2Cl_2, Sigma-Aldrich, 99.8%).

2.1.3. Catalysts, Chelating Agents and Other Additives

Ultra-pure DI water (18.2 MΩ-cm) was used for the hydrolysis of the titanium precursor. Hydrochloric acid (HCl, Sigma-Aldrich, 37%), nitric acid (HNO_3, Sigma-Aldrich, 70%) are used as reaction catalysts. Acetylacetone ($CH_3COCH_2COCH_3$, Sigma-Aldrich, 98%) was used as chelating agent to control the reaction of the titanium precursor.

2.1.4. Dopant Precursors

A variety of metal dopant precursors were used: silver nitrate ($AgNO_3$, Sigma-Aldrich, 99.0%), cobalt (II) chloride ($CoCl_2$, Sigma-Aldrich, 97%), copper (II) acetylacetonate ($Cu(C_5H_7O_2)_2$, Sigma-Aldrich, 97%), gallium (III) chloride ($GaCl_3$, Sigma-Aldrich, 99.99%), molybdenum (V) chloride ($MoCl_5$, Sigma-Aldrich, 99.99%), tantalum chloride ($TaCl_5$, Sigma-Aldrich, 99.8%), chromium (III) chloride ($CrCl_3$, Sigma-Aldrich, 99%), vanadium (III) chloride (VCl_3, Sigma-Aldrich, 97%).

2.2. Film Synthesis

Preparation of the films consisted of three steps: (i) synthesis of colloidal sol, (ii) dip-coating and (iii) calcination. Figure 2-2 shows the general outline of the film synthesis process.

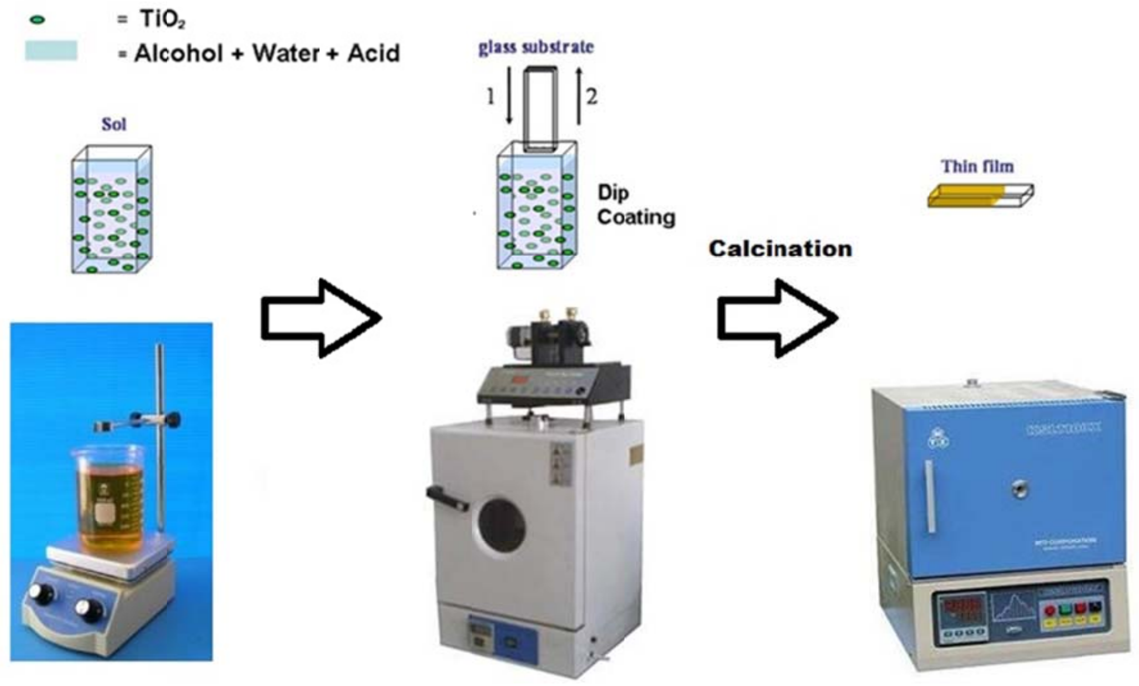

Figure 2-2: Schematics of the individual steps of synthesis of titanium dioxide films.

2.2.1. Synthesis of "sol"

In a typical preparation process, a titanium dioxide precursor (titanium isopropoxide, titanium n-butoxide, titanium tetrachloride) was dissolved in an organic solvent (typically ethanol, 2-propanol, or 1-butanol, and less commonly dimethylformamide, dichloromethane) and hydrolyzed in the presence of a catalyst (typically hydrochloric acid or nitric acid, but less commonly sulphuric acid and acetic acid). Several modification agents were used to increase the lifetime and/or viscosity of the solution. Stabilizers typically include a chelating agent with an acetyl group, most typically acetylacetone. These chelating agents strongly bind to the hydrolyzed titanium dioxide precursor (titanium oxyhydroxides) and prevent the uncontrolled polycondensation reaction that results in gelation. Viscosity of the solution was modified by solvents with very low or high viscosities such as acetonitrile, toluene, hexane, ethylene glycol, diethylene glycol, and ethyl-o-aceto-citrate. Detailed schematic of the process is shown in Figure 2-3.

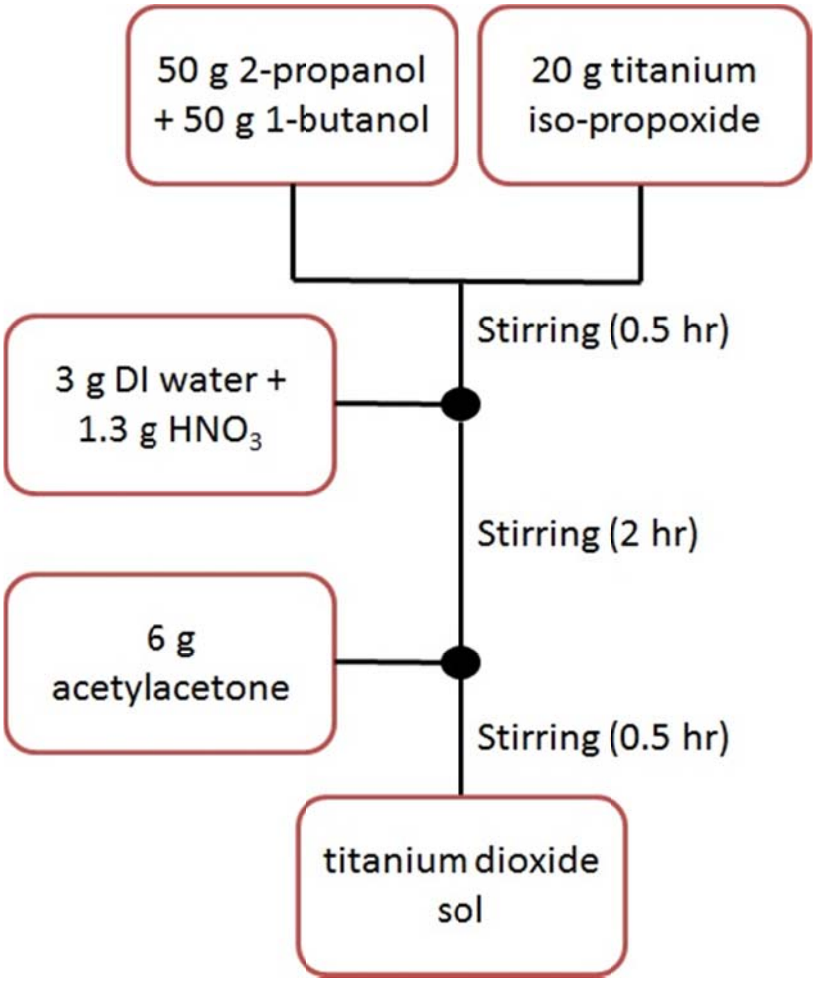

Figure 2-3: Procedure used for the undoped titanium dioxide sol synthesis.

2.2.1.1. Doping

Doping of the films was performed either in the solution preparation or in the calcination stage. Metallic dopants were introduced to the film preparation solution by using appropriate precursors so that titanium and the dopant co-hydrolyze in the solution forming a mixed oxide. Dopant precursor can be an alkoxide or a salt, though the latter is more common especially since the most metal alkoxides are either very reactive or expensive. Typical salts include acetates, nitrates, acetylacetonates, or chlorides. Acetylacetonates and chlorides were used in the majority of the cases in this study. Detailed schematic of the metal doping process -with molybdenum given as example- is shown in Figure 2-4.

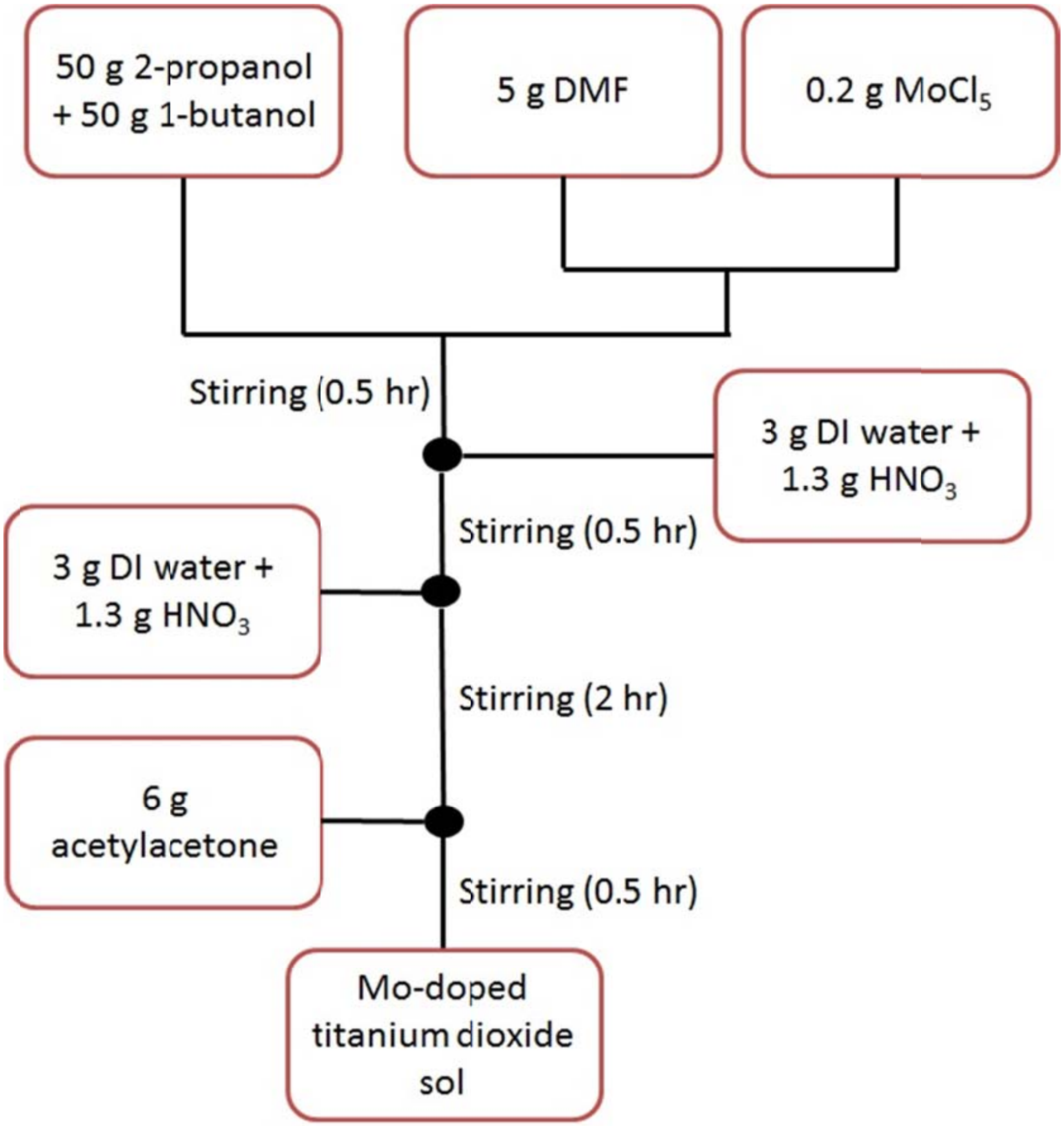

Figure 2-4: Procedure used for the metal doped titanium dioxide sols (1% at. Mo-doped titanium dioxide is given as specific example).

Nitrogen doping is performed by annealing the films in an ammonia atmosphere. Although there are reported cases of nitrogen doping by using urea or thiourea in the solution phase followed by calcination in air, the amount of nitrogen that can be incorporated into the titanium dioxide lattice was found to be low in my preliminary studies.

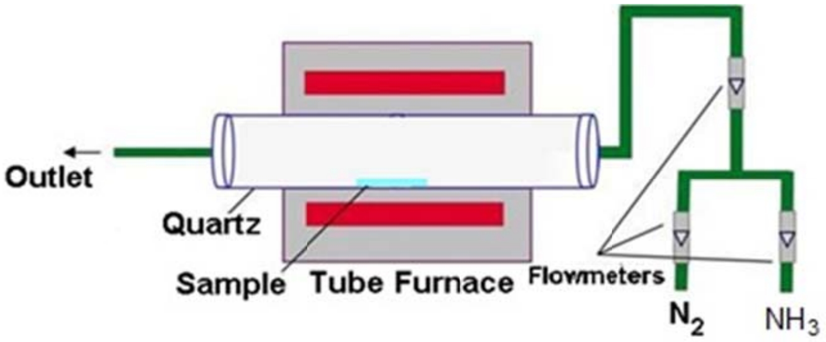

Figure 2-5: Schematics of the setup used for post-annealing of titanium dioxide films (for nitrogen doping, carbothermal reduction).

2.3. Simulation of Doping

Simulations of the doped systems were performed using the density functional theory (DFT) as implemented in the CASTEP code in Materials Studio. Doping was modeled by replacing a titanium or oxygen atom in the titanium dioxide lattice with the selected dopant followed by full geometry optimization. Dopant concentration was varied by using different size titanium dioxide super-cells. For example, in the conventional anatase lattice a titanium atom was replaced by a dopant M, which resulted in Ti_3MO_8, or 25% doping. Creation of supercells allows lower concentration such as $Ti_{15}MO_{32}$ in a 2 x 2 x 1 supercell, albeit at a significantly increased computational cost.

2.3.1. Density Functional Theory

Density functional theory (DFT) states that all ground-state properties are functionals of the charge density ρ in which total energy can be given as

$$E_t[\rho] = T[\rho] + U[\rho] + E_{XC}[\rho]$$

Where *T[ρ], U[ρ]* and *E_{XC}[ρ]* are the kinetic energy, classical electrostatic energy and energy due to many-body contributions (i.e. exchange and correlation), respectively. Charge density is constructed from the wavefunction Ψ which is taken to be an antisymmetrized product of molecular orbitals

$$\Psi = A(n)\left|\phi_1(1)\phi_2(2)...\phi_n(n)\right| .$$

When the molecular orbitals are orthonormal, i.e.

$$\left\langle \phi_i \mid \phi_j \right\rangle = \delta_{ij} ,$$

the charge density is given by

$$\rho(r) = \sum_i \left|\phi_i(r)\right|^2$$

where the sum is over all occupied molecular orbitals. In practice, molecular orbitals are expanded in terms of atomic orbitals

$$\phi_i = \sum_\mu C_{i\mu} X_\mu$$

where X_μ and $C_{i\mu}$ are the atomic basis functions and molecular orbital expansion coefficients, respectively.

Kinetic energy *T* is given by

$$T = \left\langle \sum_i^n \phi_i \left| \frac{-\nabla^2}{2} \right| \phi_i \right\rangle$$

Electrostatic energy *U* is given by

$$U = \sum_{i}^{n} \sum_{\alpha}^{N} \left\langle \phi_i(r) \left| \frac{-Z}{R_\alpha - r} \right| \phi_i(r) \right\rangle + \frac{1}{2} \sum_{i} \sum_{j} \left\langle \phi_i(r_1)\phi_j(r_2) \frac{1}{r_1 - r_2} \phi_i(r_1)\phi_j(r_2) \right\rangle + \sum_{\alpha}^{N} \sum_{\alpha<\beta} \frac{Z_\alpha Z_\beta}{\left| R_\alpha - R_\beta \right|}$$

$$= \langle -\rho(r_1) V_N \rangle + \left\langle \rho(r_1) \frac{V_e(r_1)}{2} \right\rangle + V_{NN}$$

where Z_α refers to the charge on nucleus α of an N-atom system. The first term ρV_N represents the electron-nucleus attraction, second term $\rho V_e/2$ represents the electron-electron repulsion and the final term V_{NN} represents the nucleus-nucleus repulsion.

Energy due to many-body functionals E_{XC} requires some approximation. The most common approximations are local density approximation (LDA) or generalized gradient approximation (GGA), which will not be discussed here.

Optimization of the total energy with respect to variations in ρ leads to set of coupled equations known as Kohn-Sham equations

$$\left\{ \frac{-\nabla^2}{2} - V_N + V_e + \mu_{XC}[\rho] \right\} \phi_i = \varepsilon_i \phi_i$$

where μ_{XC} is the exchange-correlation potential. Since atomic orbitals are not orbital (in contrast to molecular orbitals) reformulation of the Fourier transform of the Kohn-Sham equation gives

$$HC = \varepsilon SC$$

where

$$H_{\mu v} = \left\langle X_{\mu}(r_1) \left| \frac{-\nabla^2}{2} - V_N + V_e + \mu_{XC} \rho r_1 \right| X_v(r_1) \right\rangle$$

and

$$S_{\mu v} = \left\langle X_{\mu}(r_1) \,|\, X_v(r_1) \right\rangle .$$

Since H is a function of C, equation x has to be solved iteratively, with so-called self-consistent field theory, details of which will not be discussed here.

2.4. Photocatalytic Activity Tests

Determination of the photocatalytic activity was done by the so-called methylene blue degradation test. Methylene blue is a brightly colored cationic thiazine dye with the molecular formula $C_{16}H_{18}N_3SCl$. It has absorption maximums around 664, 614 and 292 nm. Overall photocatalytic decomposition of methylene blue in the presence of oxygen can be given with the reaction:

$$C_{16}H_{18}N_3SCl + \frac{25}{2}O_2 \xrightarrow{TiO_2, h\nu \geq 3.2eV} HCl + H_2SO_4 + 3HNO_3 + 16CO_2 + 6H_2O$$

Photocatalytic decomposition of methylene blue has been studied extensively and the intermediates and kinetics of the reaction are discusses on a number of papers (Mills and Wang 1999; Houas, Lachheb et al. 2001).

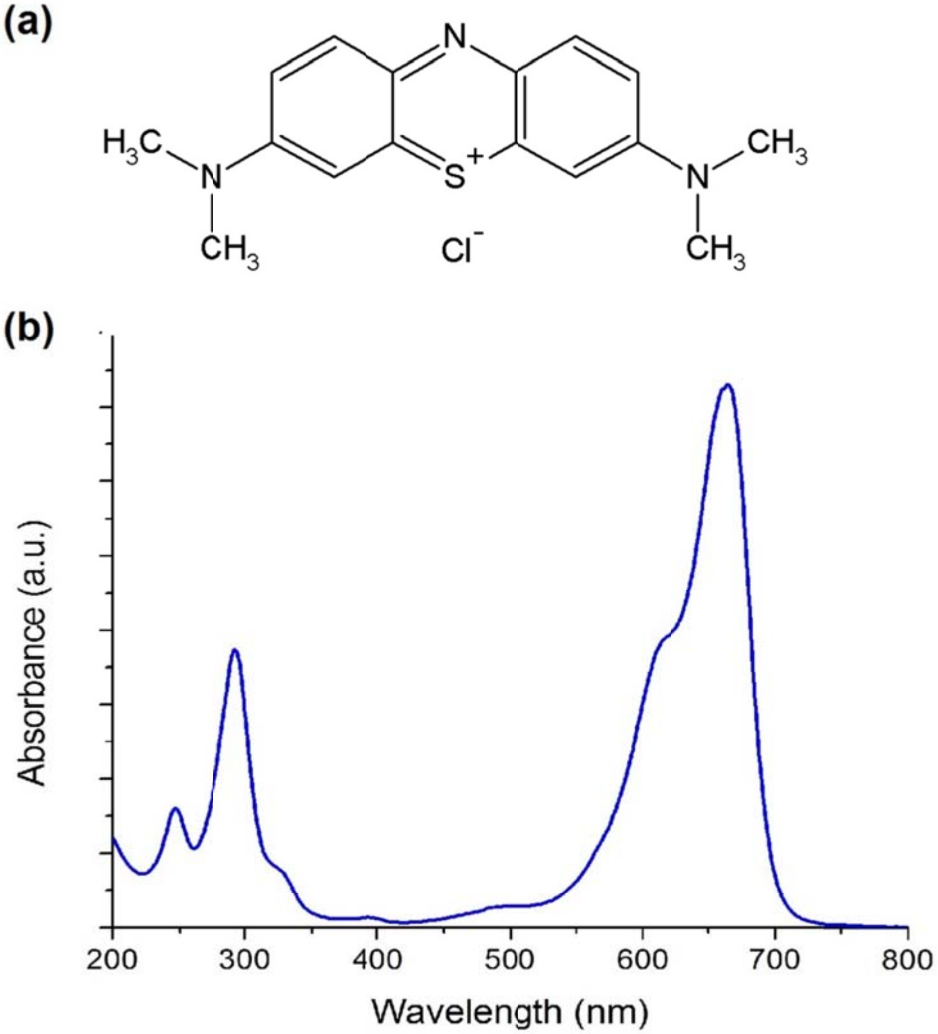

Figure 2-6: (a) Molecular structure and (b) optical spectrum of methylene blue.

In a typical photocatalytic activity test, a known amount (15 ml) and concentration (2 ppm in this study) of aqueous methylene blue solution was placed in a petri dish. Coated substrate (2 cm x 2 cm) was placed in this solution and allowed to reach adsorption equilibrium for half an hour.

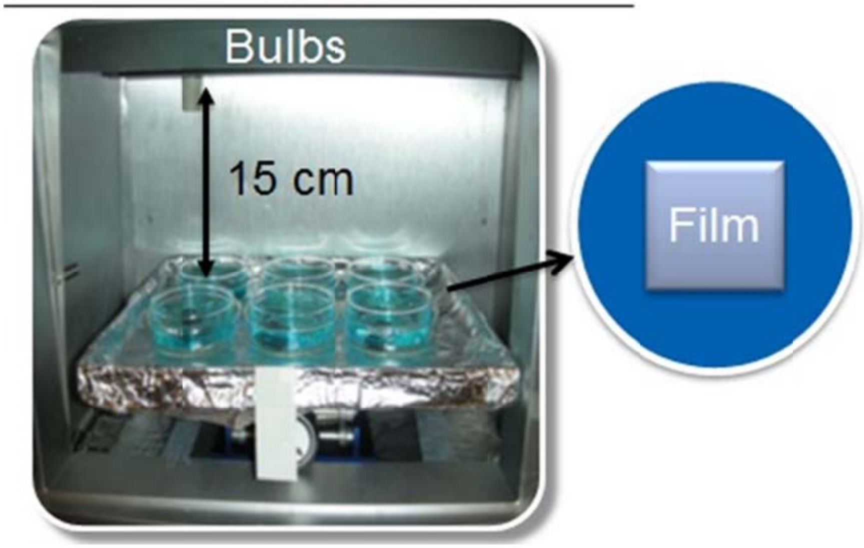

Figure 2-7: Methylene blue degradation test setup.

0.5 ml of the solution was taken from the solution and the initial concentration was determined by UV-Vis Spectroscopy using the Beer-Lambert Law, which is given by

$$A = \varepsilon \cdot l \cdot C$$

where *ε, l*, and *C* are the absorption coefficient of the liquid, the path length (10 mm), and the concentration, respectively. A is the absorbance and for liquids it can be given as

$$A = -\log\left(\frac{I}{I_0}\right)$$

where I and I_0 are the intensity of the transmitted and incident light, respectively. For methylene blue, A is the absorbance value at 664 nm. Since the absorbance value is measured, relative concentration can be calculated by simply using the formula

$$\frac{A_1}{A_0} = \frac{C_1}{C_0}$$

The samples then were placed in a light cabinet in which they are illuminated with a UV- or Visible-light source at a distance of 15 cm. Representative samples were taken at each hour from the solutions and the remaining dye concentration was analyzed by UV-Vis spectroscopy.

In order to calculate the rate constants a first-order kinetic rate was assumed,

$$\ln\left(\frac{C_0}{C}\right) = k \cdot t$$

where C, C_0, k, and t are the methylene blue concentration, initial methylene blue concentration, rate constant, and time, respectively.

2.5. Nanoindentation

Mechanical properties of the films were studied by nanoindentation technique. In a typical nanoindentation experiment, a controlled load is applied to the sample with a diamond tip where a load-displacement curve is obtained which gives key information about the mechanical properties of the sample (Figure 2-8). In contrast to typical indentation tests, nanoindentation involves much smaller loads and tip diameters.

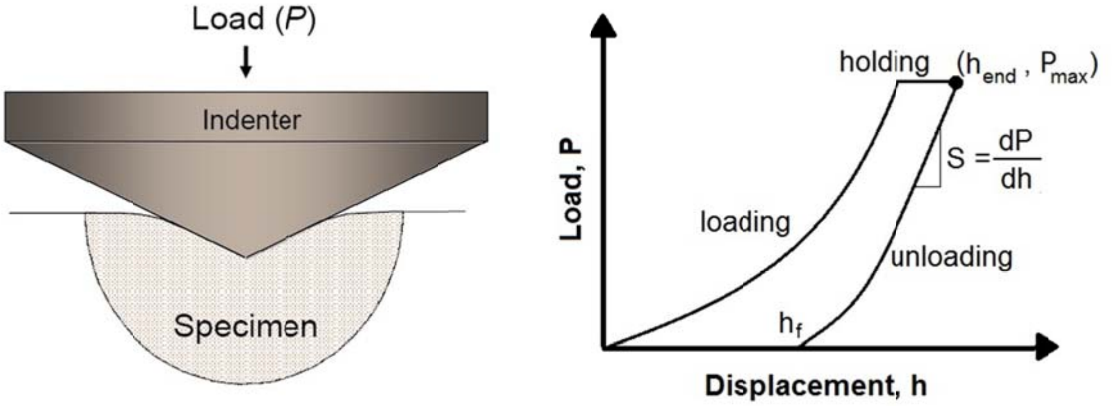

Figure 2-8: Schematics of the nanoindentation process (left) and interpretation of a typical load-displacement curve as obtained from the nanoindentation results.

Load-displacement curves obtained by the nanoindentation technique were analyzed by Oliver-Pharr formula (Oliver and Pharr 1992). Assuming a purely elastic deformation, unloading curve follows a simple power law given by

$$P = \alpha \cdot (h - h_f)^m$$

where P is the indenter load, h is the elastic displacement of the indenter, h_f is the final displacement, α and m are constants. An analytical model of the contact between the tip and the sample can be modeled by

$$S = \frac{2\sqrt{A}}{\sqrt{\pi}} \cdot E_r$$

Where A is the contact area and S is the contact stiffness. Er is called the reduced modulus and given by

$$\frac{1}{E_r} = \frac{1-\nu_i^2}{E_i} + \frac{1-\nu_s^2}{E_s}$$

Where E is the Young's modulus, ν is the Poisson's ratio and i and s refer to the indenter and sample, respectively. Contact area, A, of the tip can be found by generating a tip area function

$$A_c = f(h_c)$$

where h_c is the contact depth and is given by

$$h_c = h_{end} - \theta \cdot \frac{P_{\max}}{S}$$

Where θ = 0.72, 0.75 and 1, for conical-, spherical- and flat-punch tips respectively.

Hardness, H can be found by the formula

$$H = \frac{P_{\max}}{h_c}$$

For thin films, obtained hardness values represent the substrate-film system rather than the film alone, especially when the contact depth is larger than 10-15% of the film thickness. Although there are models to estimate the mechanical properties of the substrate and the film separately, it is not being considered here as the mechanical properties of the combined system is more relevant for practical applications.

2.6. Structural Characterization

2.6.1. X-Ray Difffraction

Crystal structure of the films was analyzed by Siemens D500 X-Ray Diffractometer. Since the films analyzed in this study were very thin (< 150 nm), getting a significant signal/noise ratio was only possible with films deposited on silicon wafers.

2.6.2. Micro-Raman Spectroscopy

Micro-Raman spectroscopy is a very powerful technique for the analysis of thin films of titanium dioxide on glass substrates where XRD analysis proves to be problematic due to high noise/signal ratio. Renishaw RM1000 Vis-Raman Spectrometer with 514.5 nm laser excitation and 100 cm^{-1} cutoff notch filter was used to analyze films.

2.6.3. UV-Vis Spectroscopy

Optical properties of the films were analyzed with Thermo Scientific Evolution 600 UV-Vis Spectrophotometer in the transmission mode for films on glass and in the reflectance mode for films on silicon wafers.

2.6.4. Fourier-Transformed Infrared Spectroscopy (FT-IR)

FTIR spectra of the films were analyzed with Varian Excalibur FTS-3000 utilizing specular reflectance accessory to study films with a variable angle.

2.6.5. Scanning/Transmission Electron Microscopy

Morphology of the films was analyzed with Zeiss Supra 50VP.

CHAPTER 3) RESULTS AND DISCUSSION

3.1. Synthesis of Undoped Titanium Dioxide Films

3.1.1. Introduction

In order to make successful comparison with the doped titanium dioxide films, it is necessary to investigate the effect of preparation parameters on the structural, photocatalytic and mechanical properties. For this purpose, titanium dioxide films were prepared on soda-lime glass substrates were subjected to various calcination temperatures and heating rates and a comparative analysis was performed to assess the effect of selected parameters on the structure, photocatalytic and mechanical properties of those films.

3.1.2. Structure

In most cases titanium dioxide films prepared by sol-gel process are amorphous or crystalize in the anatase phase. Rutile formation only occurs at high calcination temperatures (usually above 800°C). In contrast to powders, crystallization of titanium dioxide films is dominated by the underlying substrate and the film thickness. In most cases, the underlying substrate significantly hinders the crystallization of titanium dioxide, thus relatively higher calcination temperatures are necessary for films compared to powders. The substrate effect becomes lower in thicker films and crystallization follows a pattern similar to the ones seen in powder form with increasing thickness. Raman spectra of the films calcined between 400°C and 550°C at a heating rate of 5°C/min are shown in Figure 3-1. Films calcined at 400°C and 450°C are amorphous and the ones calcined at 500°C and 550°C are anatase. Thus, a calcination temperature above 450°C is necessary to crystallize titanium dioxide films. While it is, in theory, possible to increase the calcination temperature further to increase the crystallinity of the films, it is practical to stay at moderate calcination temperatures due to the extreme softening and deformation of glass slides above 550°C and unwanted formation of rutile phase which is typically inferior to anatase in terms of photocatalytic activity.

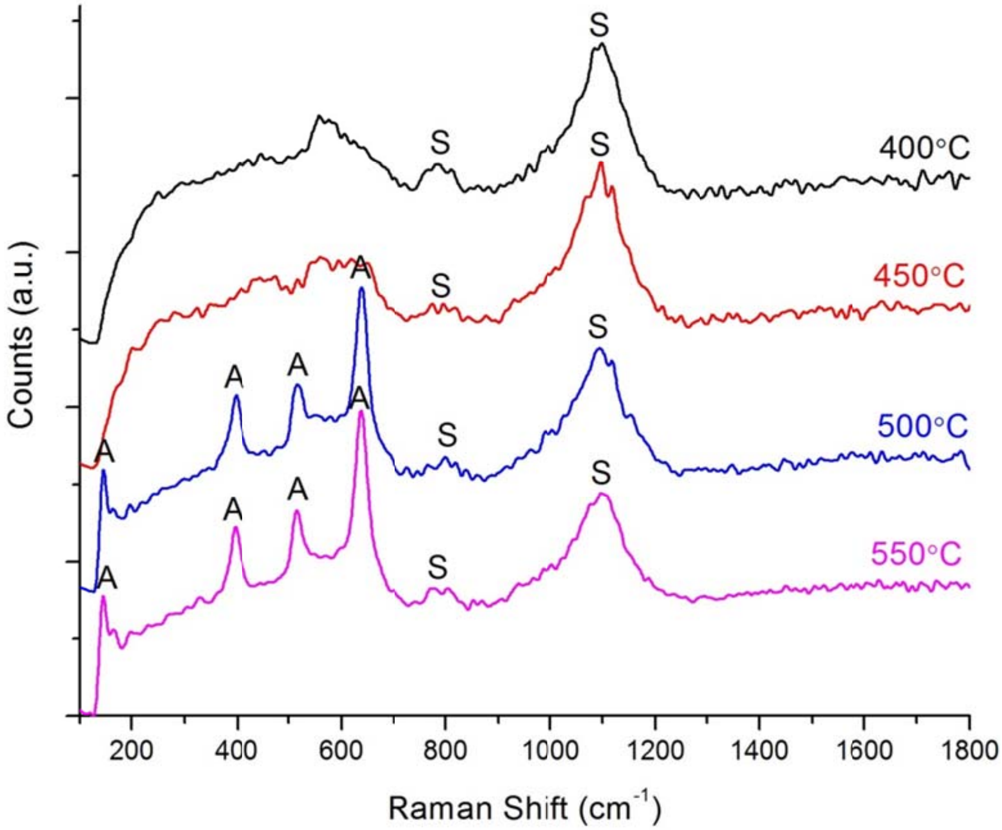

Figure 3-1: Raman spectra of titanium dioxide films on glass substrates calcined at 400°C, 450°C, 500°C and 550°C. Excitation wavelength: 514 nm, 100x magnification.

A: anatase, S: silica.

Besides the calcination temperature, heating rate also has an effect on the crystallization behavior. Raman spectra of the films calcined at 500°C with different heating rates are shown in Figure 3-2. It can be seen from the spectra that a moderate heating rate is most beneficial for crystallization whereas a too low or too high heating rate inhibits the crystallization.

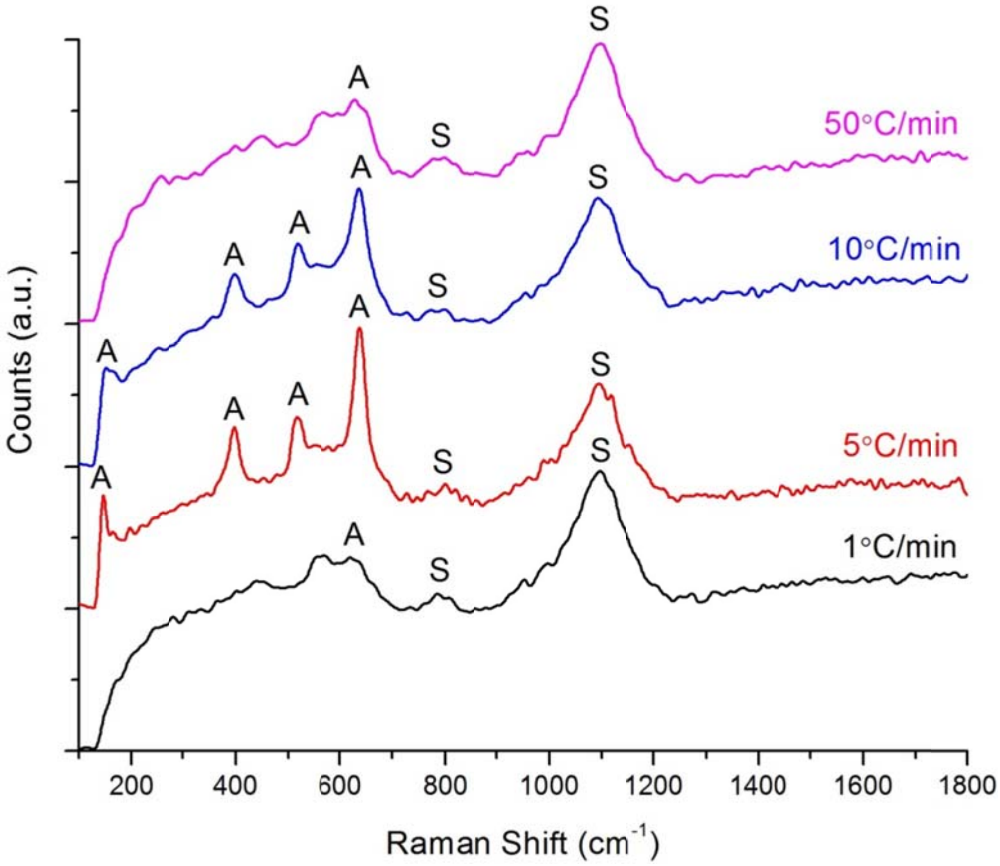

Figure 3-2: Raman spectra of titanium dioxide films on glass substrates calcined at 500°C with various heating rates. Excitation wavelength: 514 nm, 100x magnification.

A: anatase, S: silica.

Surface structure of the films investigated with scanning electron microscopy is shown in Figure 3-3. The film calcined at 500°C in the preheated furnace has very fine grains which are barely visible even with the highest magnification. For the film calcined at 500°C with a ramp rate of 5°C/min, several pin-holes were visible on the surface. These are likely due to the evaporation of water and organic constituents and short calcination time. For the samples calcined at lower temperatures, no patterns were detected on the surface, suggesting that the films were amorphous, in agreement with Raman spectroscopy results. When carefully examined, peeling and delamination was observed at some areas of the film calcined at 350°C. At these areas, it can be clearly seen that the film was not able to make a strong bonding to the glass surface but the film itself was continuous and very elastic. The low calcination temperature and short calcination time should be reason for this observation. Organics within the film structure may be responsible for the elastic behavior. While unlikely, a second reason for the peeling of the film might be the insufficient cleaning of the glass surface prior to coating which prevented the bonding in some areas. Thus, it is concluded that calcination at 350°C is not enough for an intact, durable titanium dioxide film.

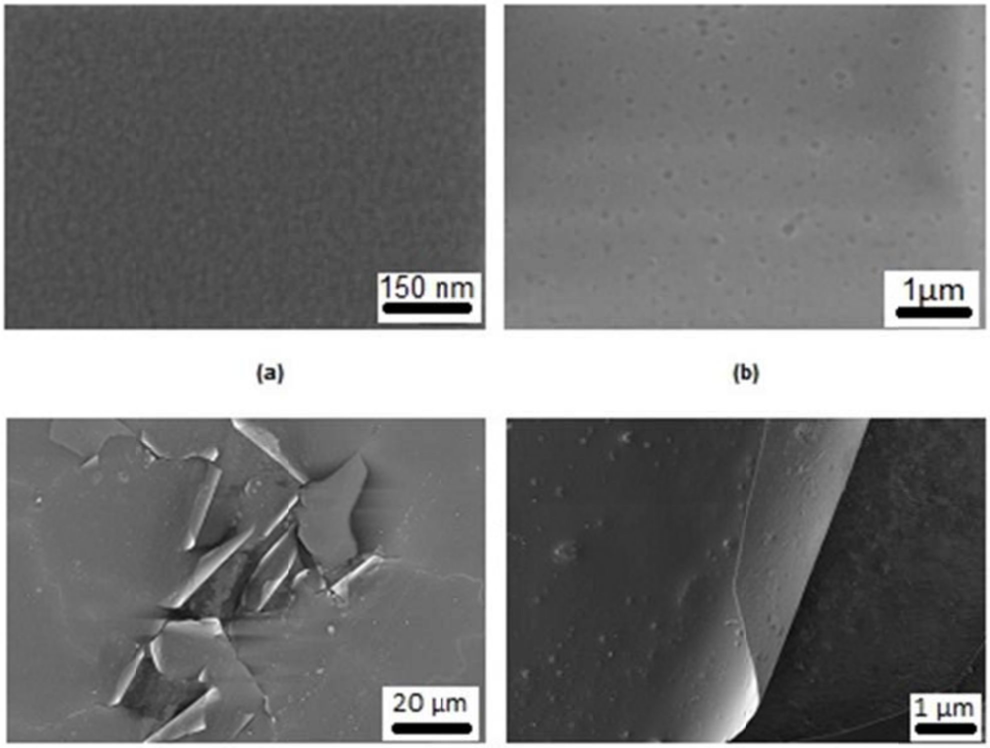

Figure 3-3: **SEM micrographs of the surface of titanium dioxide films calcined at 500°C at a heating rate of 50°C/min (a) and 5°C/min (b), at 350°C with a heating rate of 5°C/min (b-d).**

3.1.3. Mechanical Properties

In general, sol-gel titanium dioxide films are prone to cracking when deposited as a thick film with a typical thickness over 1 micron. Although cracking is less of a problem with sufficiently thin films (like the ones in this study) the interaction between the substrate and film dramatically affects the stress state, thus mechanical properties of the films.

Mechanical properties of titanium dioxide films prepared by sol-gel depend on several parameters, where the most important ones are the chemistry of the coating solution, aging of the films before calcination, calcination temperature and heating rate.

However, the calcination step dominates the mechanical properties at temperatures higher than 300-350°C as organic residue starts burning off and titanium dioxide grains start forming quickly at these temperatures. Calcination process involves the three steps: (a) heating, (b) dwell, and (c) cooling. Of these three, heating stage is extremely important as the film undergoes a significant volume reduction (i.e. densification) due to polycondensation reactions, capillary pressure upon evaporation of the liquid (solvent) and mismatch of the coefficient of thermal expansion with the substrate. During cooling stage, no major change is expected in the chemistry and the structure of the film. Although slow cooling rates are necessary in order to control stresses both in the film and the substrate, the rate should be reasonably high to keep the process cost-effective for wide range use and utilization.

Figure 3-4 shows the load-displacement curves of titanium dioxide films on glass calcined at different temperatures (constant heating rate of 10°C/min). Films calcined between 400°C and 500°C show minor differences in their mechanical behavior, whereas the film calcined at 550°C possesses significantly better mechanical properties. The improvement in such property increase can be attributed to the typical annealing point (≈550°C) of soda-lime glasses at which the film makes a strong bonding to the substrate. However, as will be shown later, such high calcinations temperatures usually lead to a poor photocatalytic activity owing to the poisoning of the catalytic film by alkali (sodium mainly) diffusion from the glass substrate.

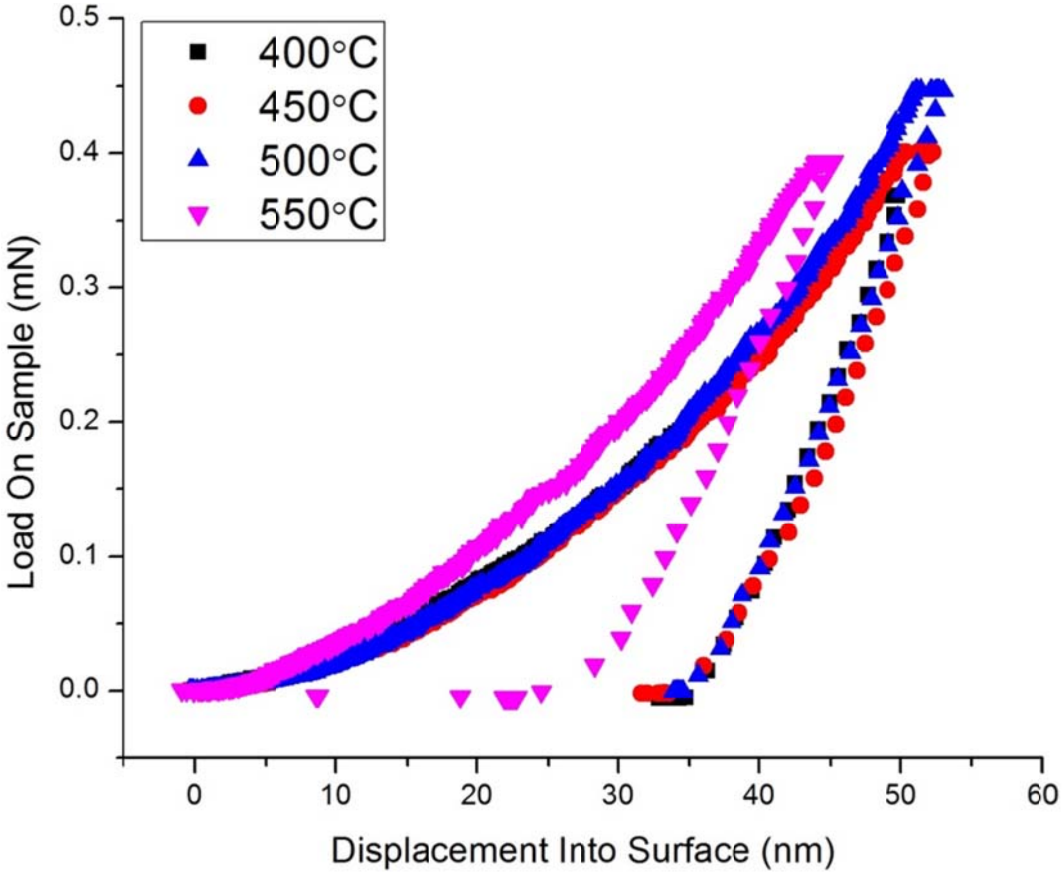

Figure 3-4: Nanoindentation Load-Displacement curves of sol-gel titanium dioxide films calcined at different temperatures at a heating rate of 10°C/min and dwell time of 1 hr.

Heating rate is one of the most important parameters that has a substantial effect on the mechanical properties of titanium dioxide films. Figure 3-5 shows the load-displacement curves of the films calcined at 500°C with different heating rates. As can be seen from the graph, films calcined with higher heating rates have better mechanical properties compared to the ones calcined with low heating rates.

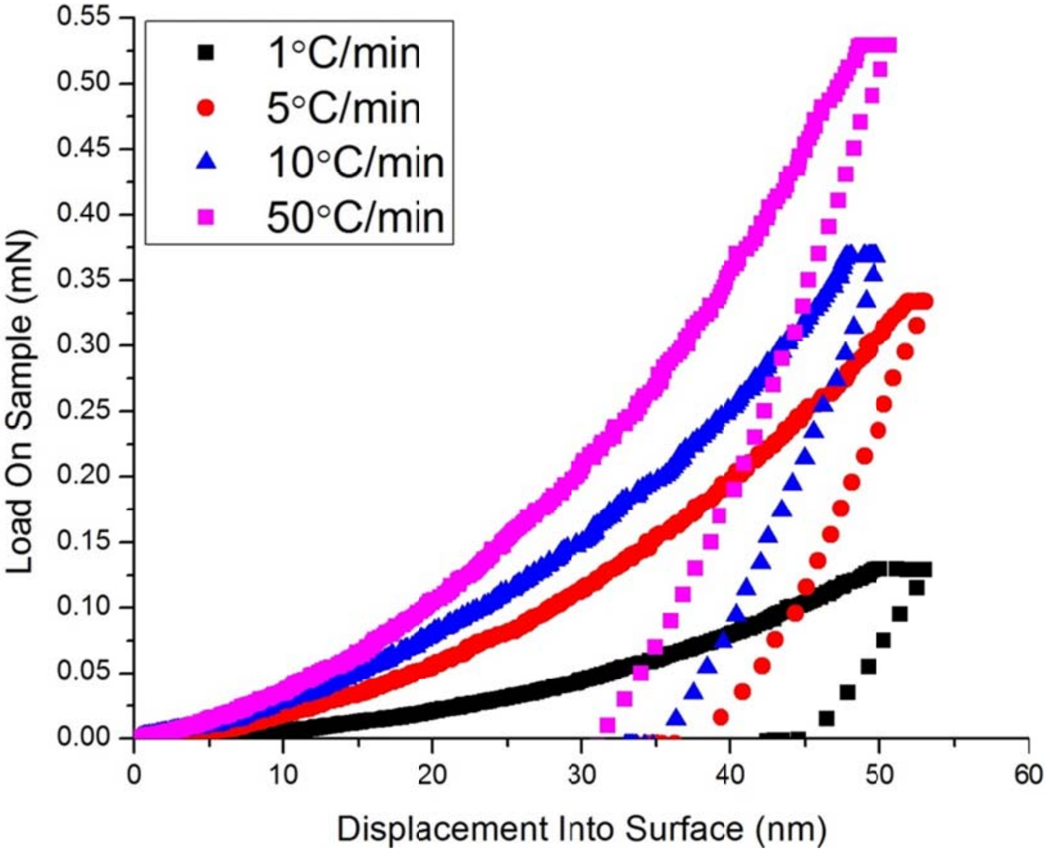

Figure 3-5: Nanoindentation Load-Displacement curves of sol-gel titanium dioxide films calcined at 500°C at different heating rates and dwell time of 1 hr.

Thus, slow heating rates are found to be detrimental to the mechanical properties of the films which is most likely due to the tensile stresses developed in the film. This can be explained by the thermal expansion effect. At a fast heating rate, the film heats up faster than the substrate and tend to expand whereas substrate expands less because of its lower temperature. This puts a compressive stress on the film thus improving the density and the mechanical properties of the film. At a small heating rate, on the other hand, film and substrate are at the same temperature and film experiences a tensile stress due to the higher thermal expansion coefficient of glass compared to titanium dioxide, which eventually degrades the mechanical properties of the films. This is explained in Figure 3-6.

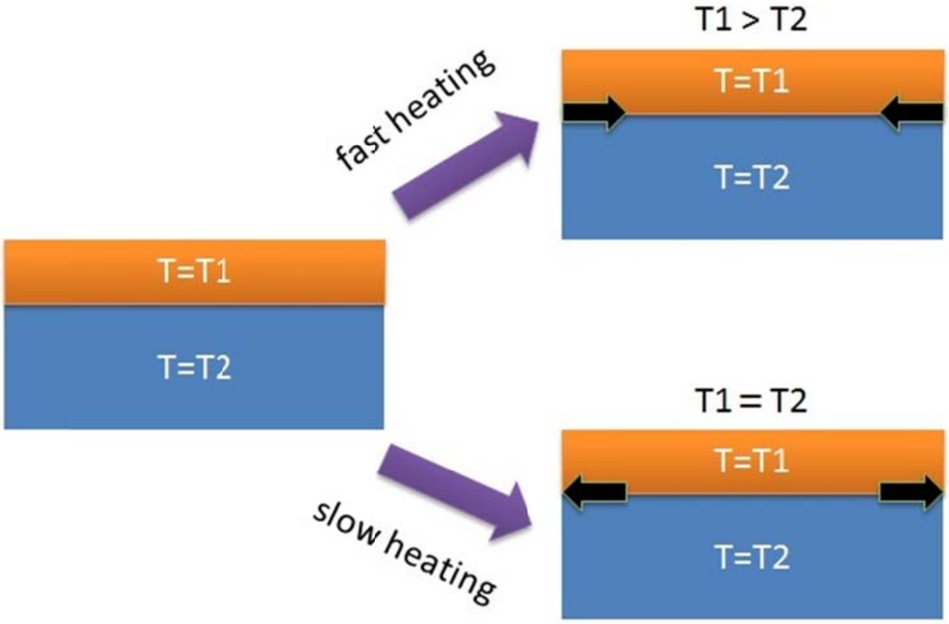

Figure 3-6: Schematics explaining the heating rate on the stress formation of titanium dioxide films.

3.1.4. Photocatalytic Activity

Both of the calcination parameters (i.e. calcination temperature and heating rate) significantly affect the photocatalytic activity of the films. Figure 3-7 and Table 3-1 shows the photocatalytic rates of films calcined at various temperatures and heating rates. Increasing the calcination temperature increase the photocatalytic activity, reaching its peak at 500°C and drops back at 550°C. This behavior can be attributed to the increasing crystallinity of the films with increasing calcination temperatures. At very high temperatures, however, grain size increases and alkali diffusion becomes very significant that it starts heavily deteriorating the photocatalytic activity. Heating rate is also found to have a significant effect on the photocatalytic activity of films, where the effect is stronger at low calcination temperatures. An optimum heating rate is found to be around 5°C/min for all temperatures.

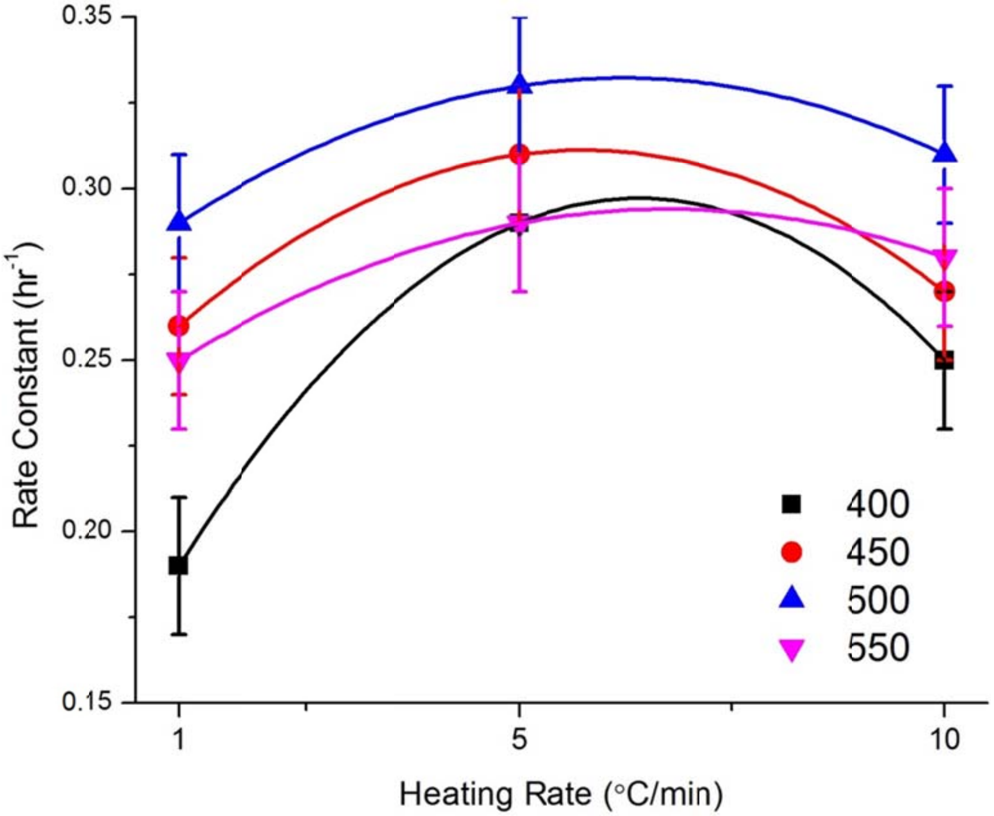

Figure 3-7: Photocatalytic rate constants of sol-gel titanium dioxide films on glass calcined at various temperatures and various heating rates.

Table 3-1: Photocatalytic reaction rate constants vs. heating rate/calcination temperature of titanium dioxide films

Calcination Temperature / Heating Rate	**Photocatalytic Reaction Rate Constant (hr^{-1})**			
	1°C/min	5°C/min	10°C/min	50°C/min
400°C	*0.19±0.02*	*0.29±0.02*	*0.25±0.02*	*0.18±0.02*
450°C	*0.26±0.02*	*0.31±0.02*	*0.27±0.02*	*0.23±0.02*
500°C	*0.29±0.02*	*0.33±0.02*	*0.31±0.02*	*0.29±0.02*
550°C	*0.25±0.02*	*0.29±0.02*	*0.28±0.02*	*0.28±0.02*

3.1.5. Conclusions

Calcination parameters have a significant effect on the structure and photocatalytic activity of titanium dioxide films. Typically, a calcination temperature higher than 350°C is necessary to ensure sufficient bonding of the film to the substrate as well as complete burning of the organic material inside the gel film structure. Complete crystallization of the films takes place only at calcination temperatures above 450°C with moderate heating rates (5-10°C/min). Mechanical properties of the films are strongly dependent on the heating rate where higher heating rates give better hardness values. Effect of calcination temperature on the hardness of the films is minor above 400°C. Best photocatalytic performance was obtained with films calcined 500°C at a heating rate of 5°C/min. Overall, a calcination temperature around 500°C with a heating rate between 5°C/min and 10°C/min gives the best photocatalytic rates with comparable mechanical properties and it is used as a guideline for the rest of the studies.

3.2. Modeling and Simulation of Doping

3.2.1. Introduction

A series of theoretical calculations were performed to understand the doping of anatase structure. Metal-, nitrogen-, and metal-nitrogen-doped anatase structures were simulated to answer the following questions:

- What is the energy cost of metal doping, i.e. substituting a titanium atom in the anatase lattice?
- How does metal doping affect the electronic properties and optical spectra of anatase?
- What is the energy cost of nitrogen doping and can it be lowered by metal co-doping?
- How does nitrogen concentration affect the optical spectra of nitrogen-doped anatase?
- Is it possible to increase the visible light absorption of nitrogen doped films by metal co-doping?

3.2.2. Simulations Parameters

All calculations were performed with the CASTEP code as part of Accelrys Materials Studio software.

In order to find the best parameters (e.g. exchange and correlation functionals, kinetic cutoff energy, k-point sampling) for best accuracy at a reasonable computational cost, a series of computations (i.e. geometry optimizations) were performed on anatase cell and the results are compared to the experimental values. The results are shown in Table 3-2. In general, local density approximation (LDA) gives results in par or better than generalized gradient approximation (GGA) for traditional exchange-correlation functionals. However, the recent correlation functionals such as Wu-Cohen and PBEsol are found to be more accurate at a relatively low extra computational cost. Unless otherwise noted, all simulations were performed using PBE-exchange and WC-correlational functionals within the GGA scheme.

Table 3-2: Accuracy and the computational cost of the selected approximations and exchange-correlation functionals. Calculations were performed with a conventional anatase cell on a dual-core Intel Xeon 2.8 GHz processor. Error is given as the largest deviation from the lattice parameters.

Functional	Exchange-Correlation	Error	Completion Time (seconds)
LDA	CA-PZ	0.51%	12511
GGA	PBE	2.44%	12298
GGA	RPBE	3.97%	17708
GGA	PW91	2.28%	12700
GGA	WC	0.07%	15325
GGA	PBESol	0.11%	15122

3.2.3. Metal Doping

Gibbs free energy changes for metal doping of titanium dioxide can be calculated by considering the reaction

$$TiO_2 + x \cdot M \Leftrightarrow Ti_{1-x}M_xO_2 + x \cdot Ti$$

Assuming that titanium is in equilibrium with the oxygen,

$$Ti + O_2 \Leftrightarrow TiO_2$$

Then,

$$\mu_{TiO_2} = \mu_{Ti} + \mu_{O_2}$$

For oxygen-rich limit

$$\mu_{Ti} = \mu_{TiO_2} - \mu_{O_2}$$

And for Ti-rich limit

$$\mu_{Ti} = \mu_{Ti(bcc)}.$$

Chemical potentials of the dopants can be defined similarly as

$$x \cdot \mu_M = \mu_{M_xO_y} - \frac{y}{2} \cdot \mu_{O_2}$$

For oxygen-rich limit and

$$\mu_M = \mu_{M\,(metal)}$$

for the metal-rich limit.

Since the calculations are done assuming that the system is at absolute minimum temperature, i.e. 0K, the chemical potentials are simply equal to the Gibbs free energy as there is no entropy contribution at this temperature.

Calculated Gibbs free energy changes upon substituting a Ti atom with a dopant in the anatase lattice are given in Figure 3-8. The energy barrier for substituting titanium with another transition metal in the anatase lattice increases almost linearly with the group number of the dopant in the periodic table. Second group (i.e. the group titanium is in) elements (zirconium and hafnium) have the lowest energy barrier. The energy barrier also increases with increasing period number of the dopant elements, though the correlation is not as clear as group-effect. After the transition block, energy barrier tends to decrease with increasing group numbers, in contrast to what is seen in the transition block dopants. Particularly germanium and tin have similar low energy barriers with transition metal dopants such as chromium, molybdenum and manganese. Metals such as silver, gold, platinum, palladium, and copper have such high-energy barriers that they may not enter into the anatase lattice at all.

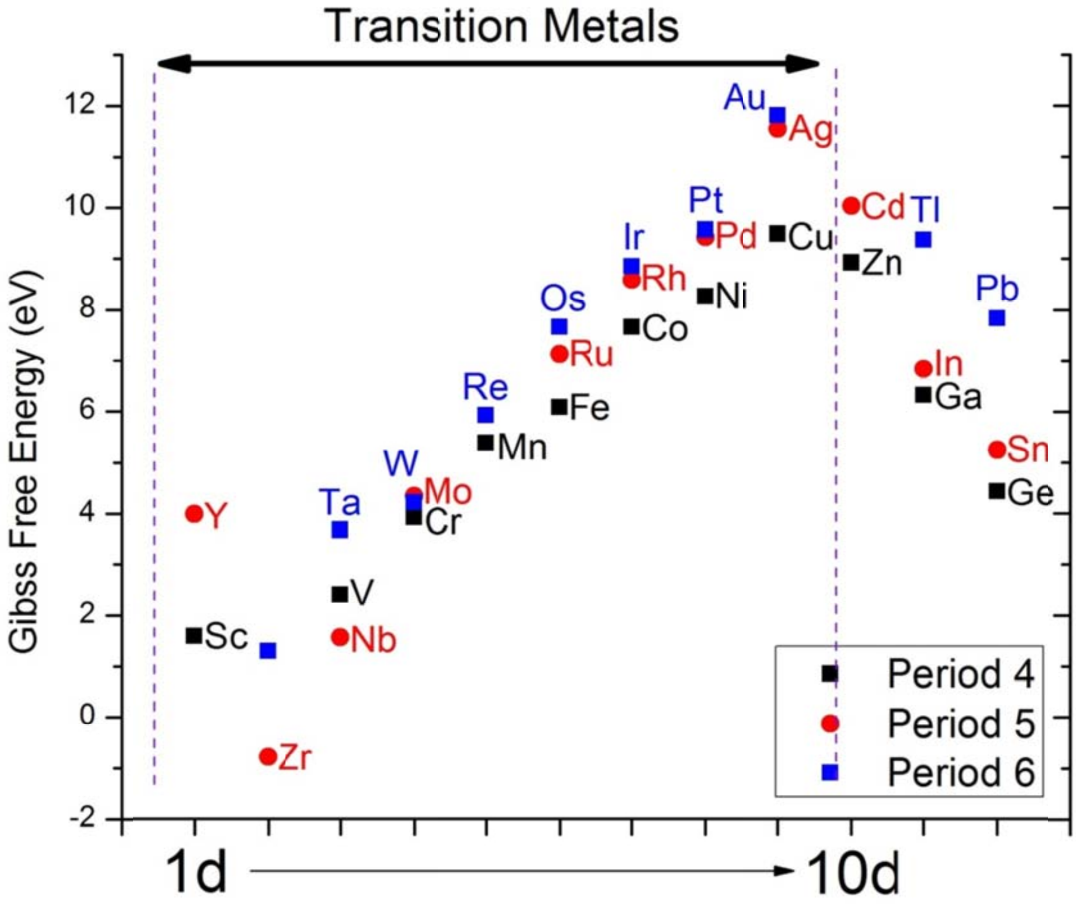

Figure 3-8: Calculated Gibbs free energy changes of doping of various elements into the titanium dioxide (anatase) lattice.

The general trend can be seen in Figure 3-9. Typically, the closer the group number to the group that titanium is in (2d), the lower the energy barrier is. This trend holds for dopants in the transition block, whereas it is reversed outside the transition block.

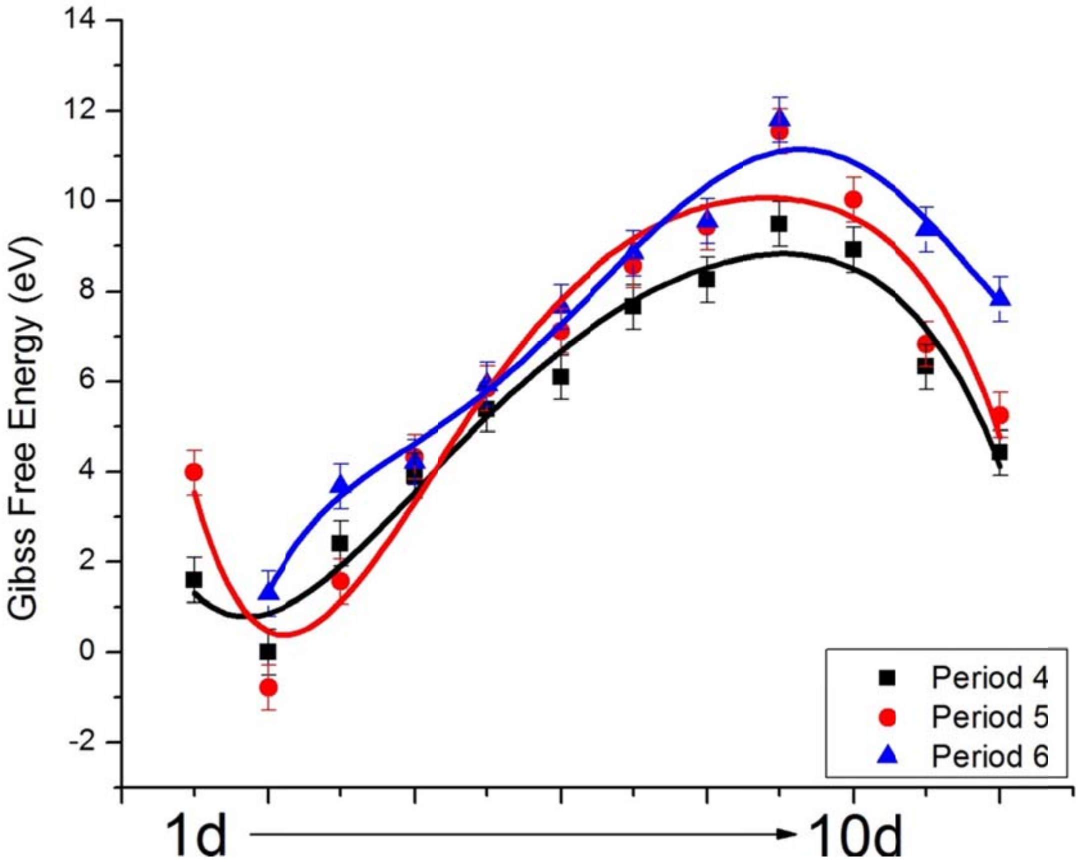

Figure 3-9: Trend in the Gibbs free energy cost of doping with different elements.

Since the simulations were performed assuming a quite high dopant concentration (25 at.%), dopant-dopant interactions can play a role which may change the obtained energy values. In order to test this, energy barrier of the three elements (Cr, Mo, Co) at a lower concentration (6.25%) were calculated. The results show that dopant-dopant interactions are not significant (at least for these elements) and the deviation of the calculated energy barrier with decreased concentration is less than 5%.

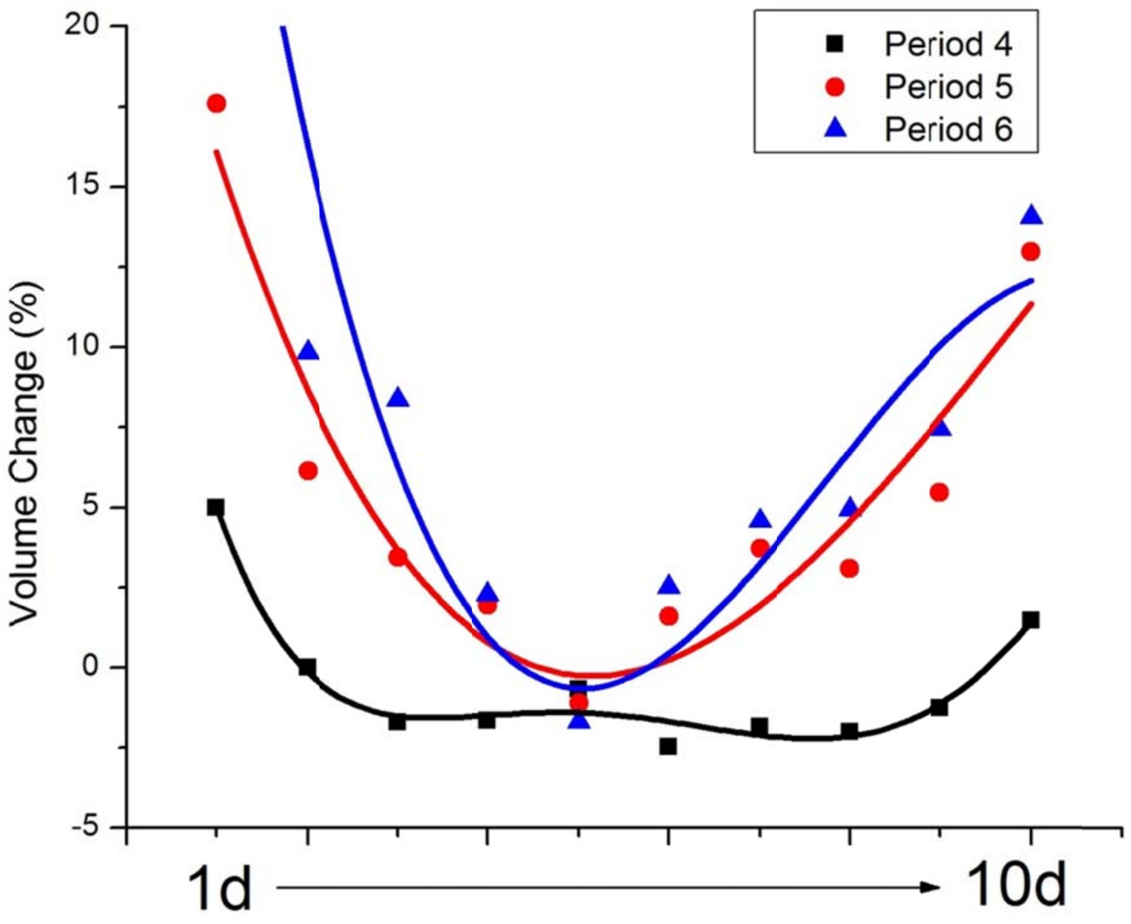

Figure 3-10: Resulting volume changes in the anatase lattice accompanying the doping with different elements in the transition block.

Volume changes caused by doping are shown in Figure 3-10. In general, dopants from the 4th period result in contraction whereas others result in expansion with increasing period number. Amount of volume change decreases from 1d to 5d then increases until 10d. After the transition block, amount of change in the volume by doping decreases with increasing group numbers.

The effect of doping on the magnetic properties is shown in Figure 3-11. Assuming a ferromagnetic ordering, all dopants from the 4th period except nickel and zinc and germanium give a net magnetic spin to the structure. The magnetization was much weaker in other periods with only notable exception of molybdenum which gives a net magnetic moment higher than cobalt. The highest magnetic moments were obtained with manganese, iron, and chromium.

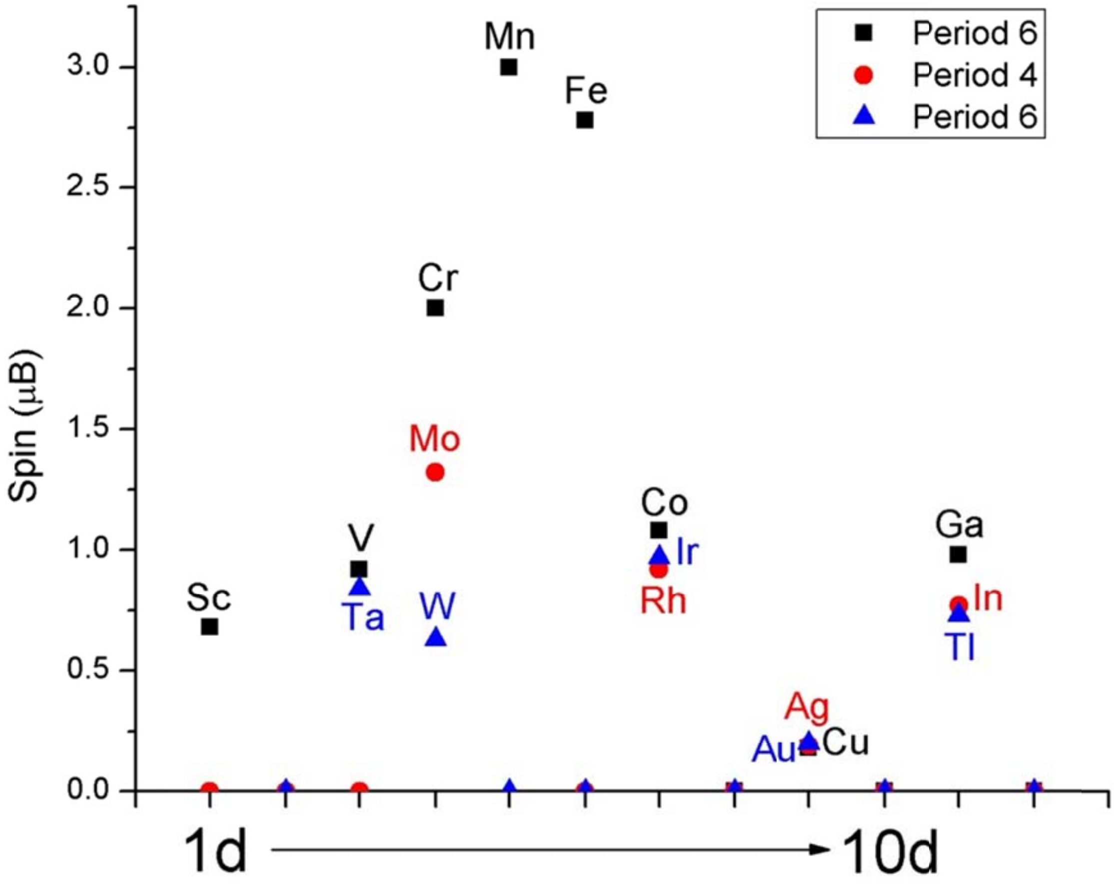

Figure 3-11: Calculated net spin of metal-doped structures.

Calculated optical spectra of the doped systems from Period 4 are shown in Figure 3-12. Scandium, zinc, gallium and germanium caused an overall blue shift of the optical absorption edge whereas vanadium, chromium, manganese, iron, cobalt, nickel and copper caused red-shift of the spectra. However, it should be noted that none of the red shifts are indicating a fundamental band gap narrowing but formation of intra-band gap defect levels. Nickel and copper doping, in particular, cause significant absorption around the near-infrared region.

Table 3-3: Summary of results of the doping of anatase with 4th Period elements.

Dopant	Concentration	Volume Change (%)	Energy of Formation (eV)	Spin (μB)
Sc	0.25	+4.99	+1.59	0.68
V	0.25	-1.71	+2.40	0.92
V	0.12	-0.89	+2.42	1.00
V	0.06	-0.48	+2.43	1.00
Cr	0.25	-1.65	+3.91	2.00
Cr	0.12	-1.42	+4.00	2.00
Mn	0.25	-0.68	+5.38	3.00
Mn	0.12	-0.47	+5.33	3.00
Fe	0.25	-2.47	+6.09	2.78
Co	0.25	-1.85	+7.66	1.08
Ni	0.25	-2.01	+8.26	0.00
Cu	0.25	-1.26	+9.49	0.18
Zn	0.25	+1.47	+8.92	0.00
Ga	0.25	+1.18	+6.32	0.98
Ge	0.25	-0.73	+4.42	0.00

Table 3-4: Summary of results of the doping of anatase with 5th Period elements.

Dopant	Concentration	Volume Change (%)	Energy of Formation (eV)	Spin (µB)
Y	0.25	+17.60	+3.98	0.00
Zr	0.25	+6.14	-0.78	0.00
Nb	0.25	+3.45	+1.56	0.00
Mo	0.25	+1.93	+4.33	1.32
Ru	0.25	+1.60	+7.12	0.00
Rh	0.25	+3.71	+8.58	0.92
Pd	0.25	+3.08	+9.42	0.00
Ag	0.25	+5.47	+11.55	0.19
Cd	0.25	+12.97	+10.03	0.00
In	0.25	+10.01	+6.83	0.77
Sn	0.25	+7.62	+5.25	0.00
Sb	0.25	+8.17	+6.47	0.00

Table 3-5: Summary of results of the doping of anatase with 6th Period elements.

Dopant	Concentration	Volume Change (%)	Energy of Formation (eV)	Spin (µB)
Hf	0.25	+9.83	+1.29	0.00
Ta	0.25	+8.37	+3.67	0.84
W	0.25	+2.28	+4.21	0.63
Re	0.25	-1.69	+5.93	0.00
Os	0.25	+2.50	+7.65	0.00
Ir	0.25	+4.57	+8.85	0.97
Pt	0.25	+4.93	+9.56	0.00
Au	0.25	+7.44	+11.81	0.20
Tl	0.25	+13.01	+9.37	0.73
Pb	0.25	+11.34	+7.83	0.00

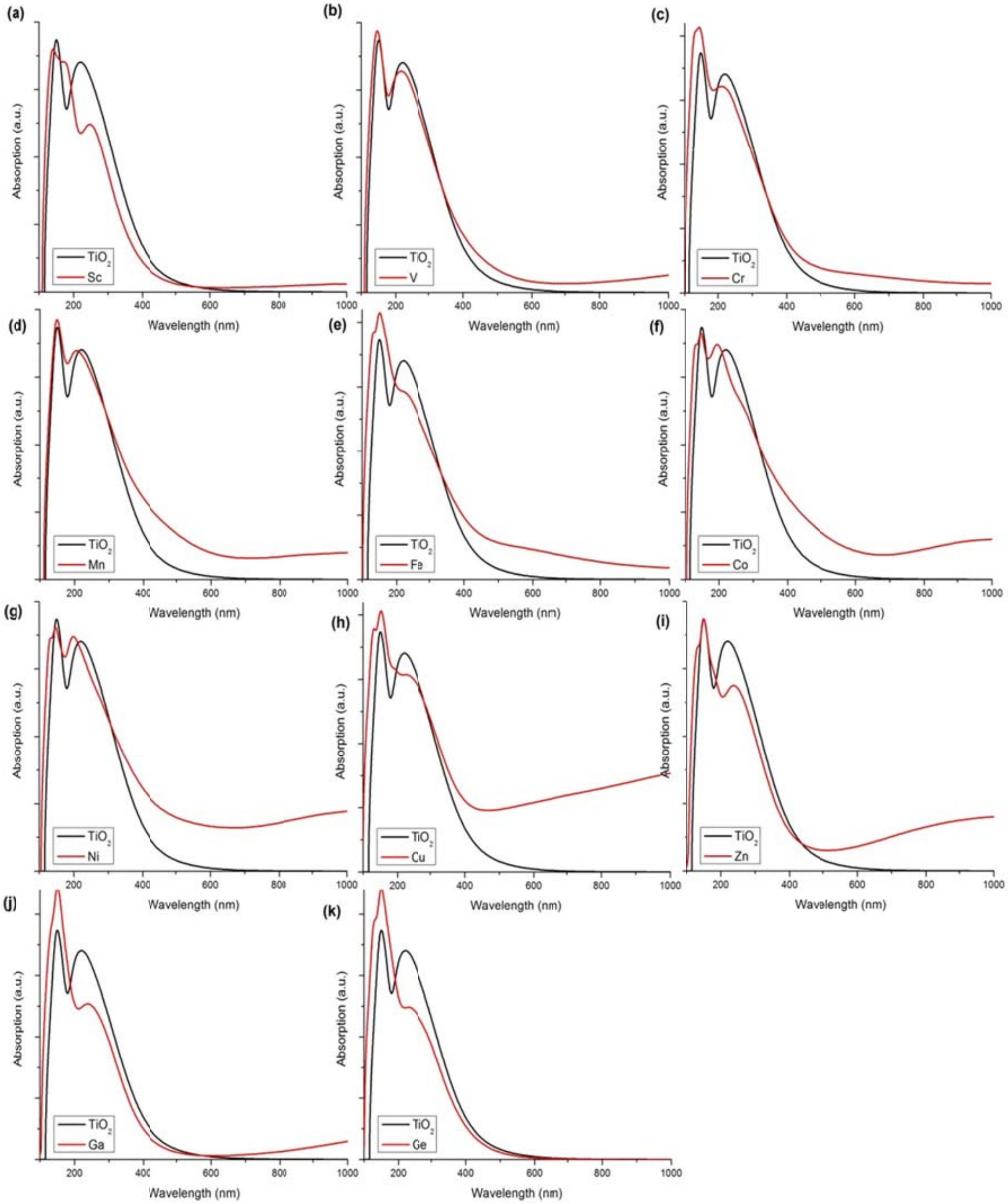

Figure 3-12: Calculated optical spectra of (a) Sc-, (b) V-, (c) Cr-, (d) Mn-, (e) Fe-, (f) Co-, (g) Ni-, (h) Cu-, (i) Zn-, (j) Ga-, and (k) Ge-doped anatase. Calculated optical spectrum of anatase is given at each figure for comparison.

3.2.4. Nitrogen Doping

The energy cost for the reaction

$$4TiO_2 + \frac{1}{2}N_2 \rightarrow 4TiO_{\frac{7}{4}}N_{\frac{1}{4}} + \frac{1}{2}O_2$$

is calculated to be 4.8 eV for oxygen-poor conditions.

Effect of nitrogen doping on the electronic properties of titanium dioxide is shown in Figure 3-13 and 3-14, where density of states plots and optical spectra with varying nitrogen concentration can be seen.

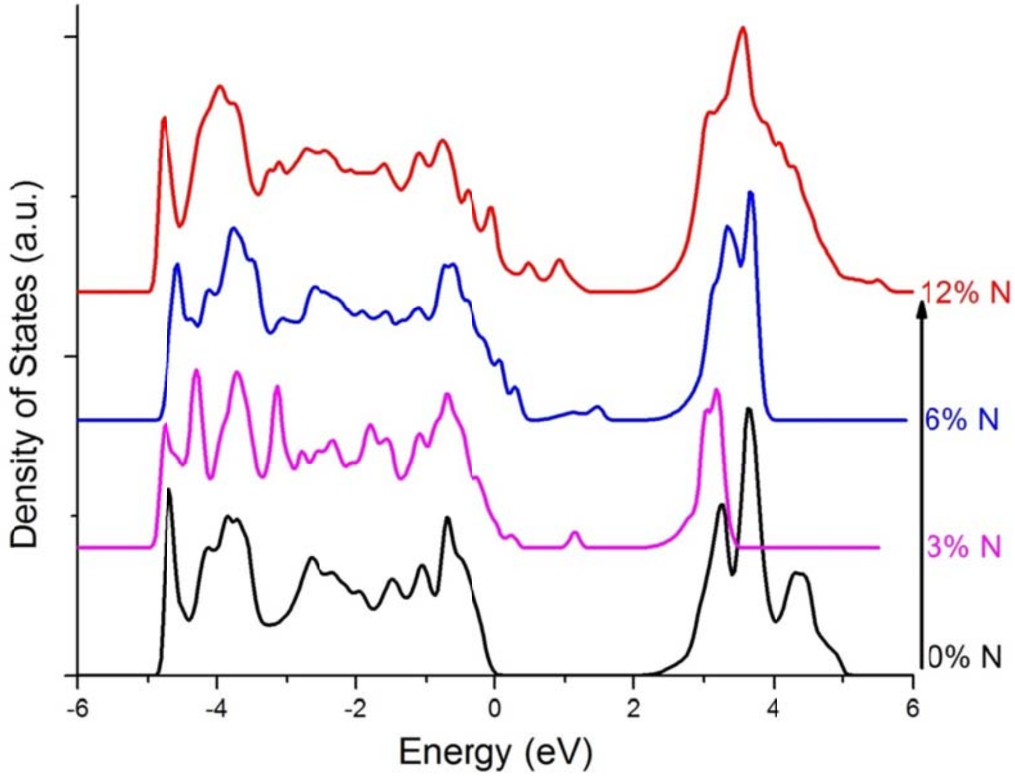

Figure 3-13: Density of states (DOS) plots of N-doped anatase with various nitrogen concentrations.

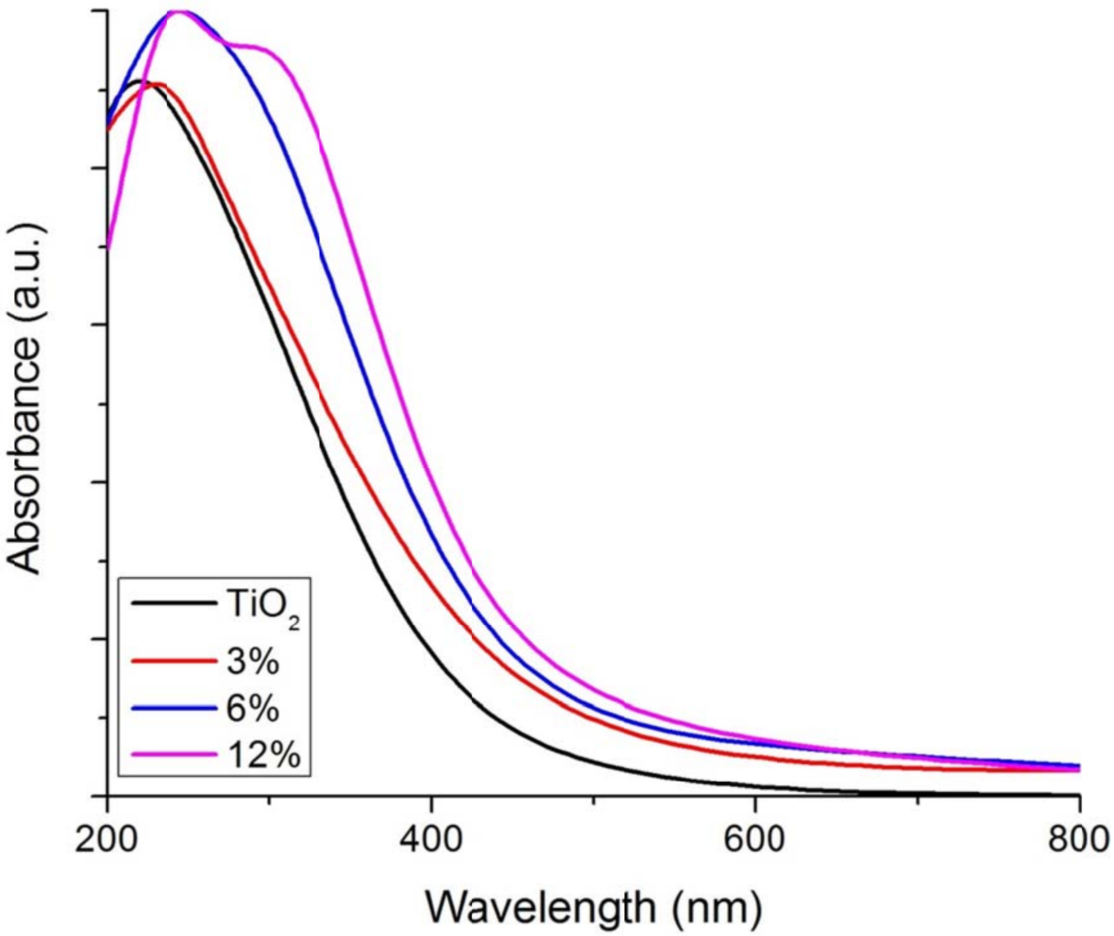

Figure 3-14: Calculated optical absorption spectra of N-doped anatase with various nitrogen concentrations.

3.2.5. Metal-Nitrogen Doping

Nitrogen doping was modeled in the assumption that nitrogen replaces oxygen (substitutional doping) and in the case of metal-nitrogen doping, nitrogen was placed next to the metal dopant (Figure 3-15).

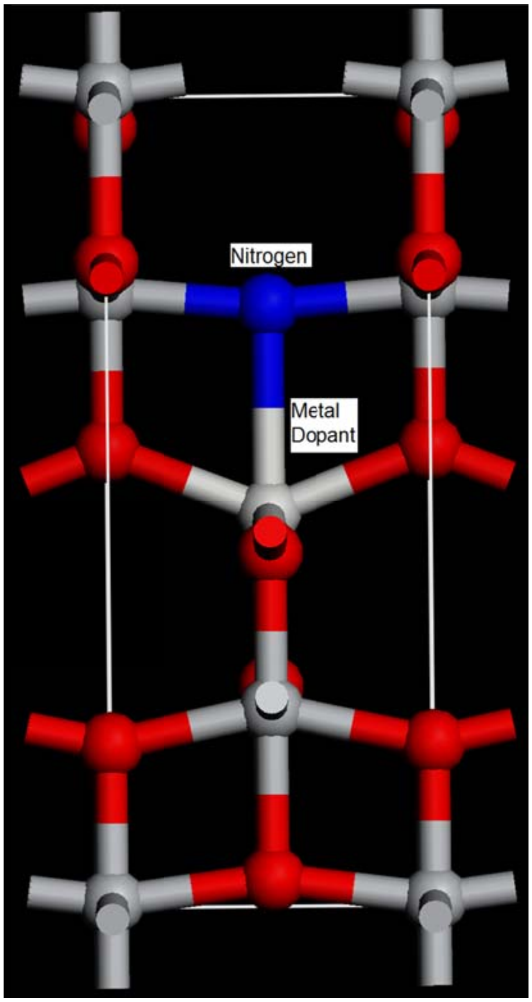

Figure 3-15: Metal-nitrogen doped anatase cell used for calculations.

Energy required for nitrogen doping is shown in Figure 3-16. All of the metal dopants decreased the energy cost of nitrogen doping, and the effect was substantial for vanadium, chromium and iron co-doping.

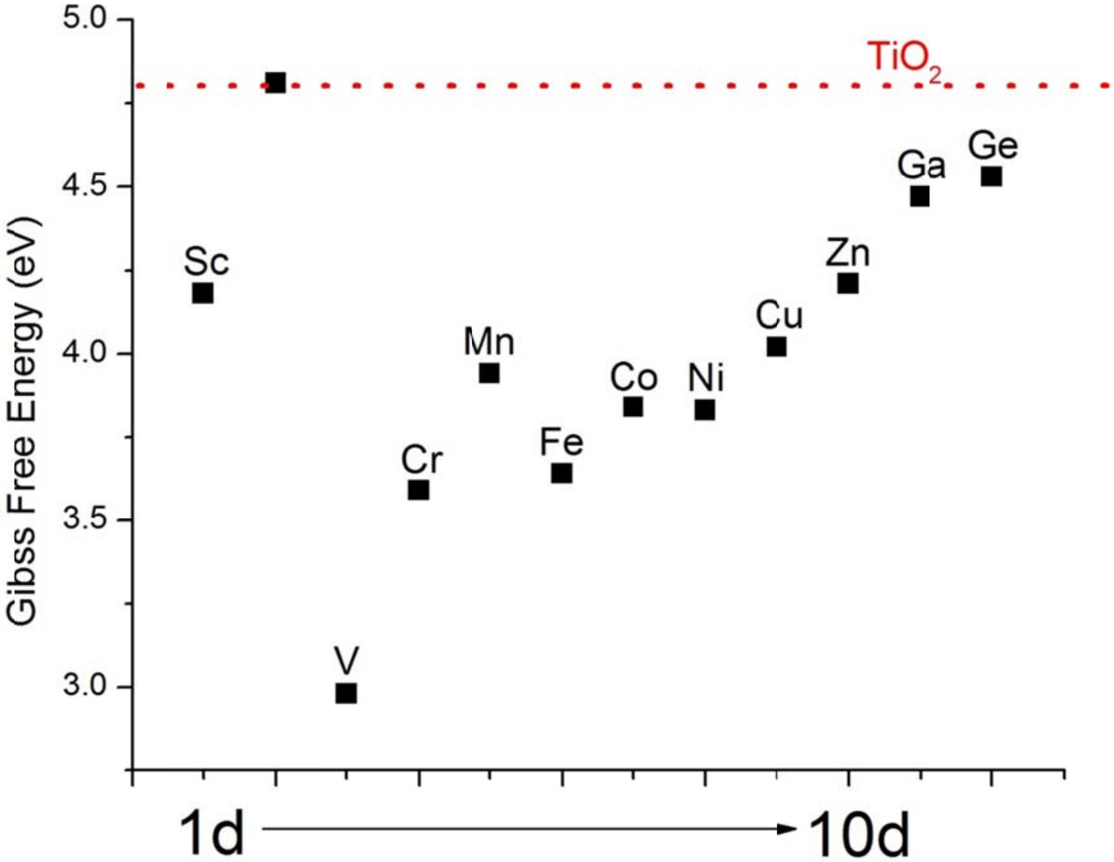

Figure 3-16: Calculated Gibbs free energy changes of metal co-doping into the nitrogen-doped titanium dioxide (anatase) lattice.

Calculated optical spectra of the metal-nitrogen doped anatase with various metal co-dopants are shown in Figure 3-17. Compared to nitrogen-doped anatase at the same concentration; scandium, zinc, gallium and germanium co-doped systems cause an overall blue-shift of the spectrum while the other co-dopants show mixed results. Even though iron, cobalt, nickel, manganese and copper co-doped systems show increased absorption in the visible region, a clear absorption edge has disappeared, forming a flat absorption region, an indication of a series of defect centers which will likely act as recombination centers. With chromium and vanadium, on the other hand, the absorption edge is still clear and resembles the case with titanium dioxide and nitrogen-doped titanium dioxide (Figure 3-14). Thus, from theoretical point of view (considering only the absorption spectra), chromium and vanadium co-doping may be beneficial for photocatalytic activity.

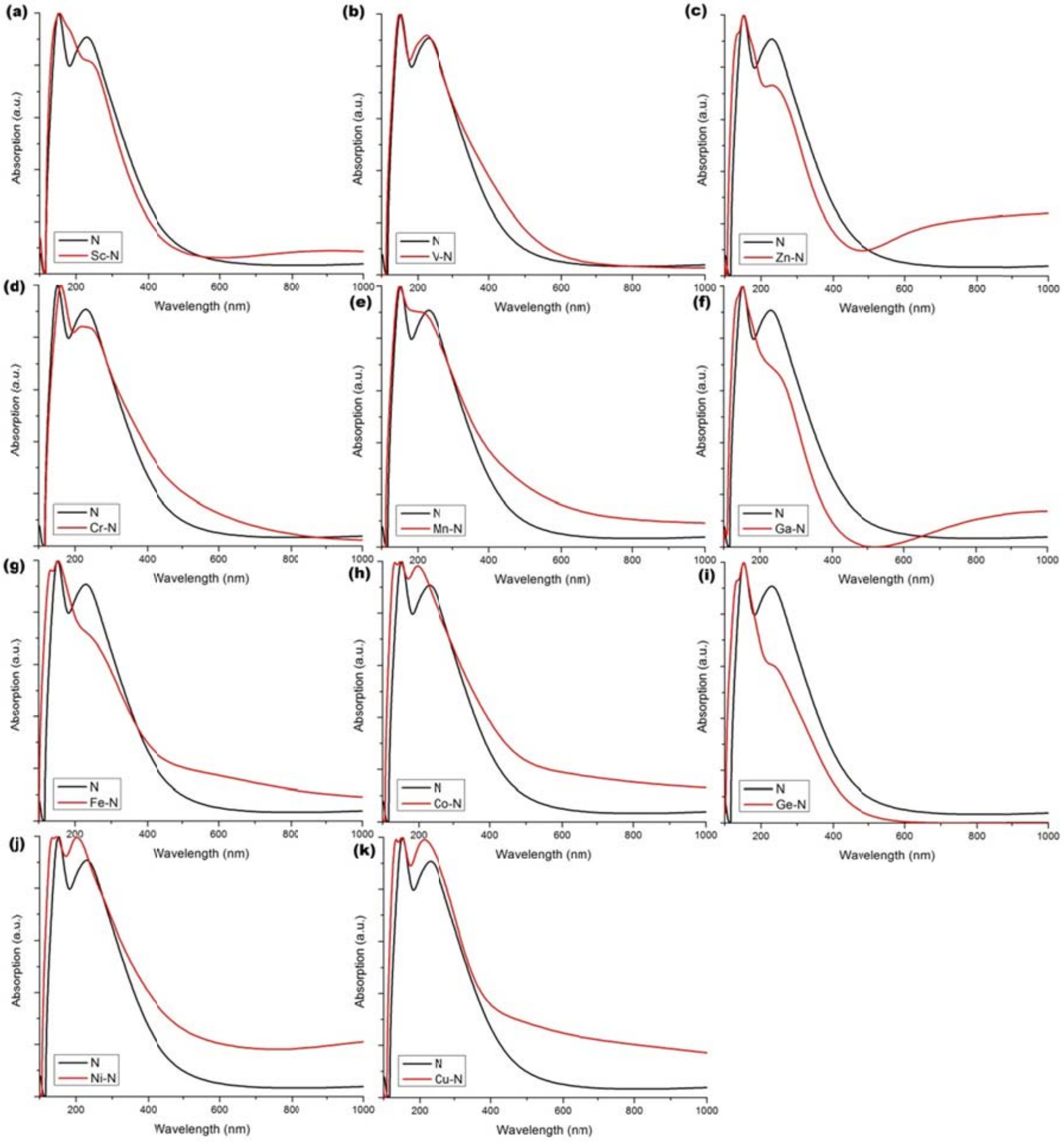

Figure 3-17: Calculated optical spectra of (a) Sc-N, (b) V-N, (c) Zn-N, (d) Cr-N, (e) Mn-N, (f) Ga-N, (g) Fe-N, (h) Co-N, (i) Ge-N, (j) Ni-N, and (k) Cu-N doped anatase. Calculated optical spectrum of nitrogen doped anatase is given at each figure for comparison.

Magnetic behavior is observed with nitrogen-doped structures while the net magnetic moment is suppressed with co-doping with vanadium, copper, zinc and gallium, unchanged with chromium, nickel and germanium co-doping, increased with scandium, manganese, iron and cobalt. Net spin of metal-nitrogen doped anatase structures with various metal co-dopants are shown in Figure 3-18.

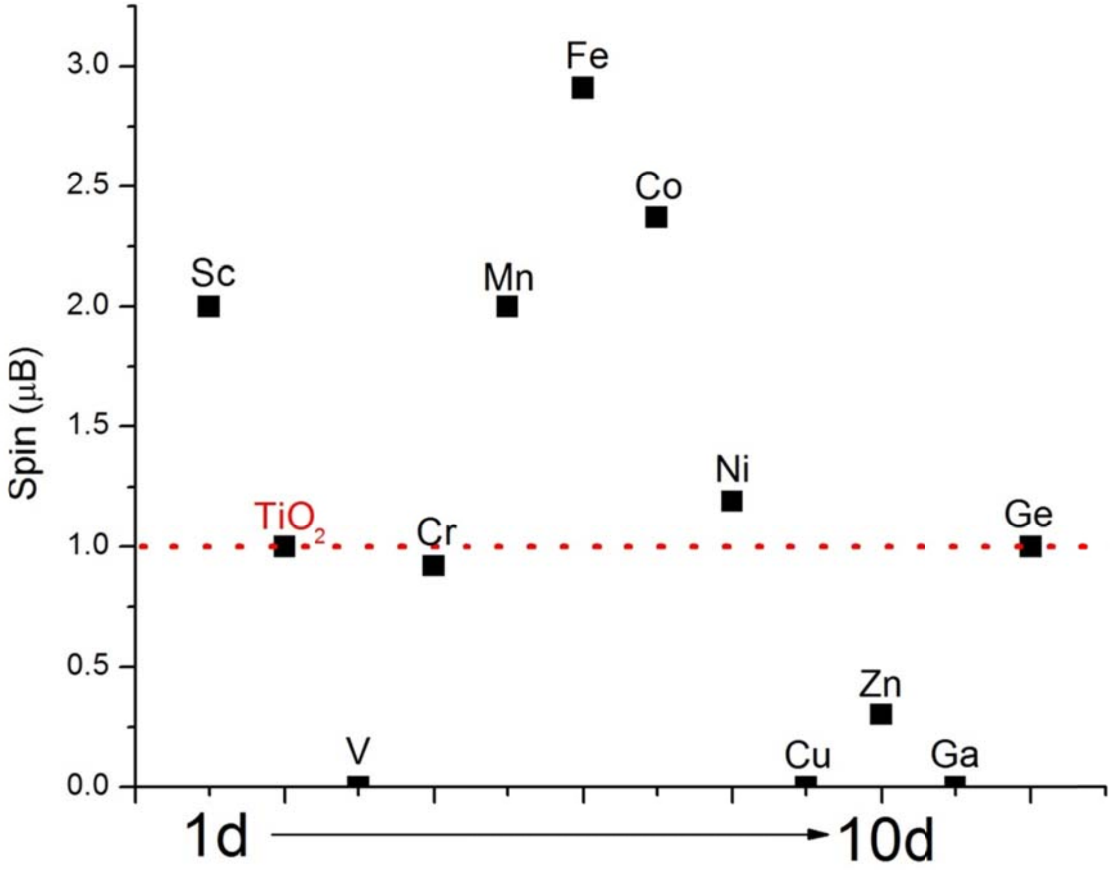

Figure 3-18: Calculated net spin of metal-nitrogen doped anatase with various metals.

Metal-nitrogen bond lengths are given in Figure 3-19. Most of the elements (vanadium, chromium, manganese, iron, cobalt, nickel, copper and germanium) possessed shorter metal-nitrogen bond lengths compared to titanium-nitrogen bond length. Gallium and zinc had similar bond lengths whereas scandium-nitrogen bond length was significantly longer. It is interesting to note that vanadium and chromium stand out having the shortest bond lengths which may be responsible for their "different" optical spectra.

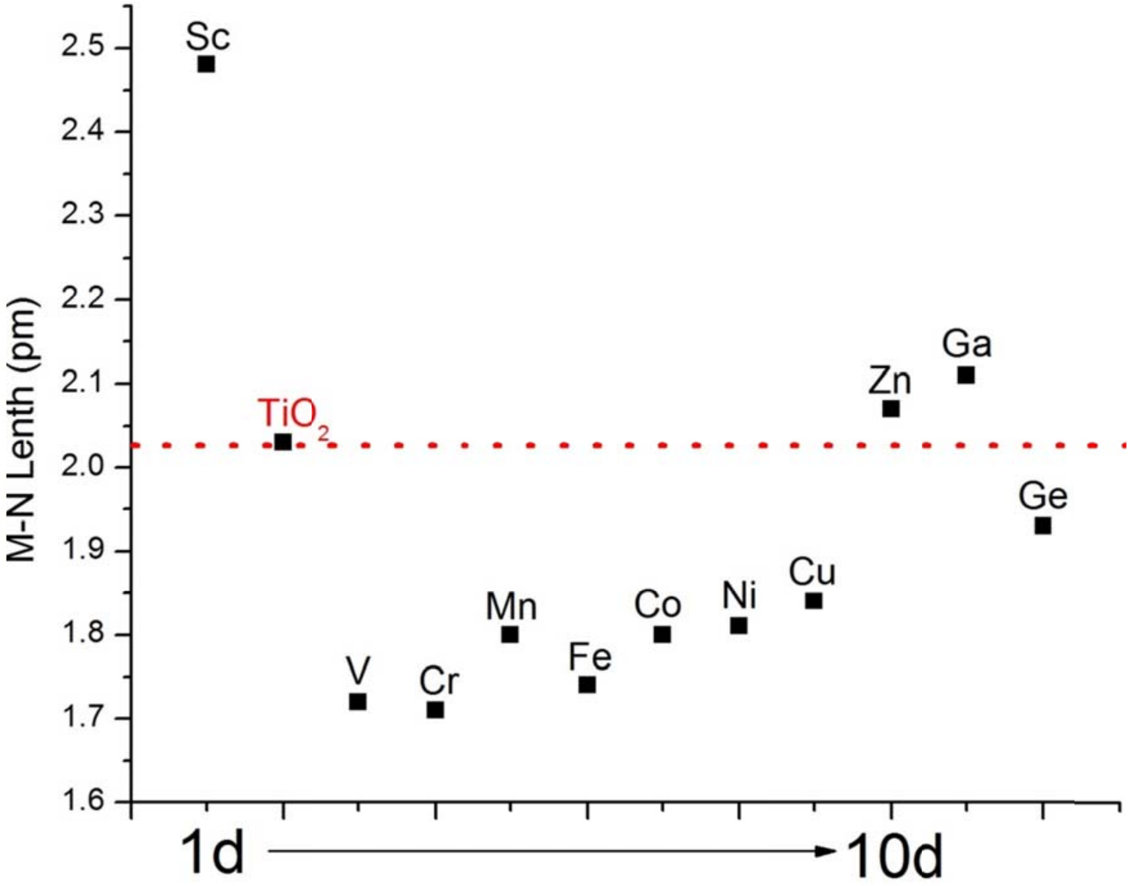

Figure 3-19: Metal-nitrogen bond length in metal-nitrogen doped anatase structures.

3.2.6. Conclusions

Theoretical calculations of doping process with various metal and metal-nitrogen combinations were conducted to gain an understanding of the thermodynamic costs and resulting changes in the electronic structure of anatase. It is found that the energy cost of substituting titanium with a metal dopant is directly related to the position of that particular metal in the periodic table. The period that metal dopant is located has a minor effect while the group number of the metal dramatically affects the energy cost of doping. In the transition block, metals with higher group numbers are found to be the most costly dopants to replace titanium in the anatase lattice (with a peak cost at 9d) whereas the reverse is true for dopants outside the transition block. Interestingly, no clear correlation is found between the energy cost and the volumetric change of the cell caused by doping. None of the metals caused a significant change in the calculated optical spectra.

All of the tested metal co-dopants decreased the energy cost of nitrogen doping into the anatase structure, and improved visible light absorption was observed particularly with chromium and vanadium co-dopants.

3.3. Carbothermally Reduced Titanium Dioxide Films

3.3.1. Introduction

It is known that sol-gel preparation conditions and parameters such as the type and amount of the precursor and solvent used (Tracey, Hodgson et al. 1998), concentration of water in the solution (Hague and Mayo 1994), pH (Ahn, Kim et al. 2003) and chelating agents (Schubert 2005) have dramatic effects on the structure and functionalities of titanium dioxide films. On the other hand, morphology and the mechanical stability of the films are almost entirely determined by the post-deposition thermal treatment, or calcination (Langlet 2003). In many cases, good mechanical integrity needs to be coupled with good photocatalytic and optical properties in order to achieve sufficient lifetime of the coatings, since their functionalities can be lost if the films are deteriorated due to wear or environmental degradation.

In this part of the study, a set of titanium dioxide films were carbothermally reduced at a wide range of temperatures and the resulting oxygen-deficit films were analyzed in terms of their crystal structure, morphology UV and visible light photocatalytic activity and mechanical properties. The results were compared to an identical set of films calcined with the same parameters at an oxidative atmosphere.

3.3.2. Experimental

Films were prepared by dip-coating (MTI Dip Coater HL-01); for this purpose, Si (100) substrates were dipped into the prepared solution and withdrawn at a constant speed of 100mm/min. Si (100) wafers were used because they provide the same SiO_2 surface as glass, but their flatness, purity and relatively small thermal expansion mismatch with TiO_2, making them ideal model substrates. The humidity was varied between 20% and 30% during coating. Following the coating procedure, samples were taken to a tube furnace for calcination at temperatures between 400°C and 1000°C (in 100°C steps) either in static air or under nitrogen flow (270 cc/min) for 2 hours with a heating rate of 25 °C/min.

3.3.3. Results and Discussion

The film thickness exhibited by ellipsometric measurements on samples calcined at 900°C was approximately 30-35 nm for both air and nitrogen heat-treated samples. Figure 3-20 shows the refractive index values of the representative films as obtained from ellipsometric analysis. Films calcined at 900°C in air had a significantly higher refractive index compared to the one calcined under nitrogen at the same temperature, indicating higher density for air-calcined films. For films calcined under nitrogen, an inverse relationship was found between the refractive index and the calcination temperature.

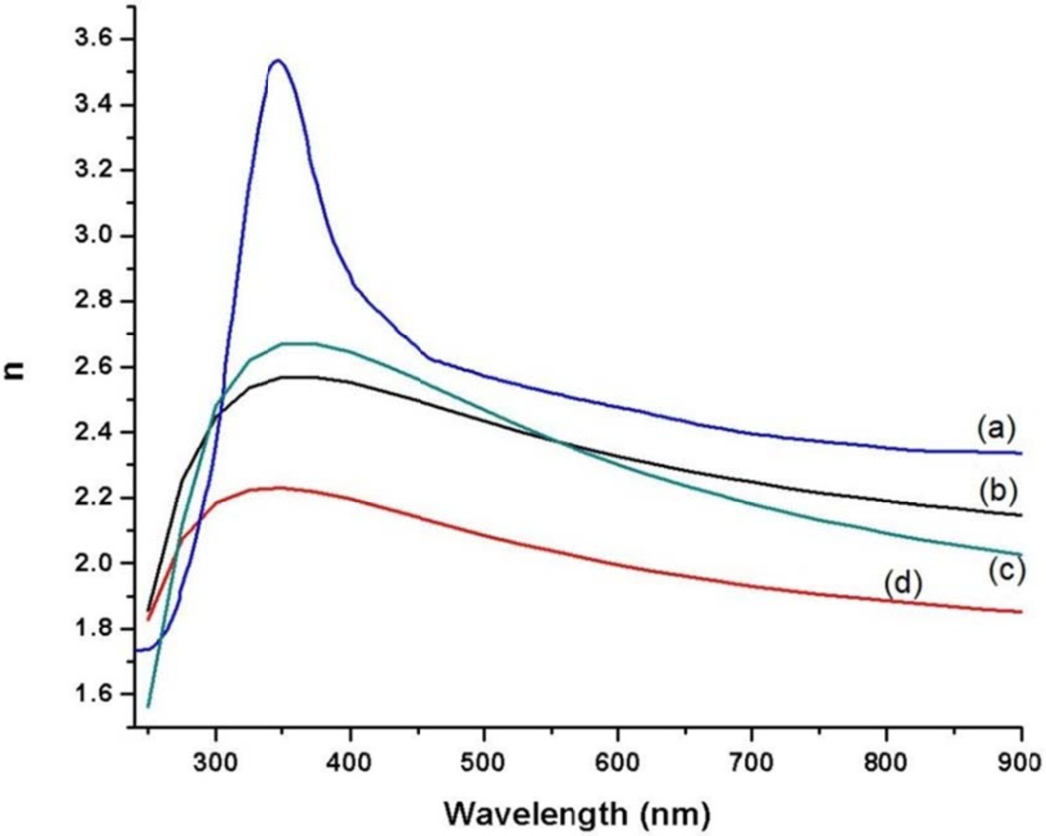

Figure 3-20: Refractive index (n) vs. wavelength plots of films calcined at (a) 900°C in air, (b) 700°C under N_2, (c) 800°C under N_2, and (d) 900°C under N_2 .

Figure 3-21 shows the XRD pattern of films calcined in (a) air and (b) nitrogen. No peaks were detected from the films calcined at 400°C regardless of the calcination atmosphere, whereas only nitrogen calcined films at 500°C didn’t show any peaks. Air calcined films are composed of anatase up to 800°C, after which rutile peaks are detected along with anatase. At 1000°C, transformation to rutile is complete. Rutile is the only crystal phase detected from nitrogen-calcined films at all temperatures.

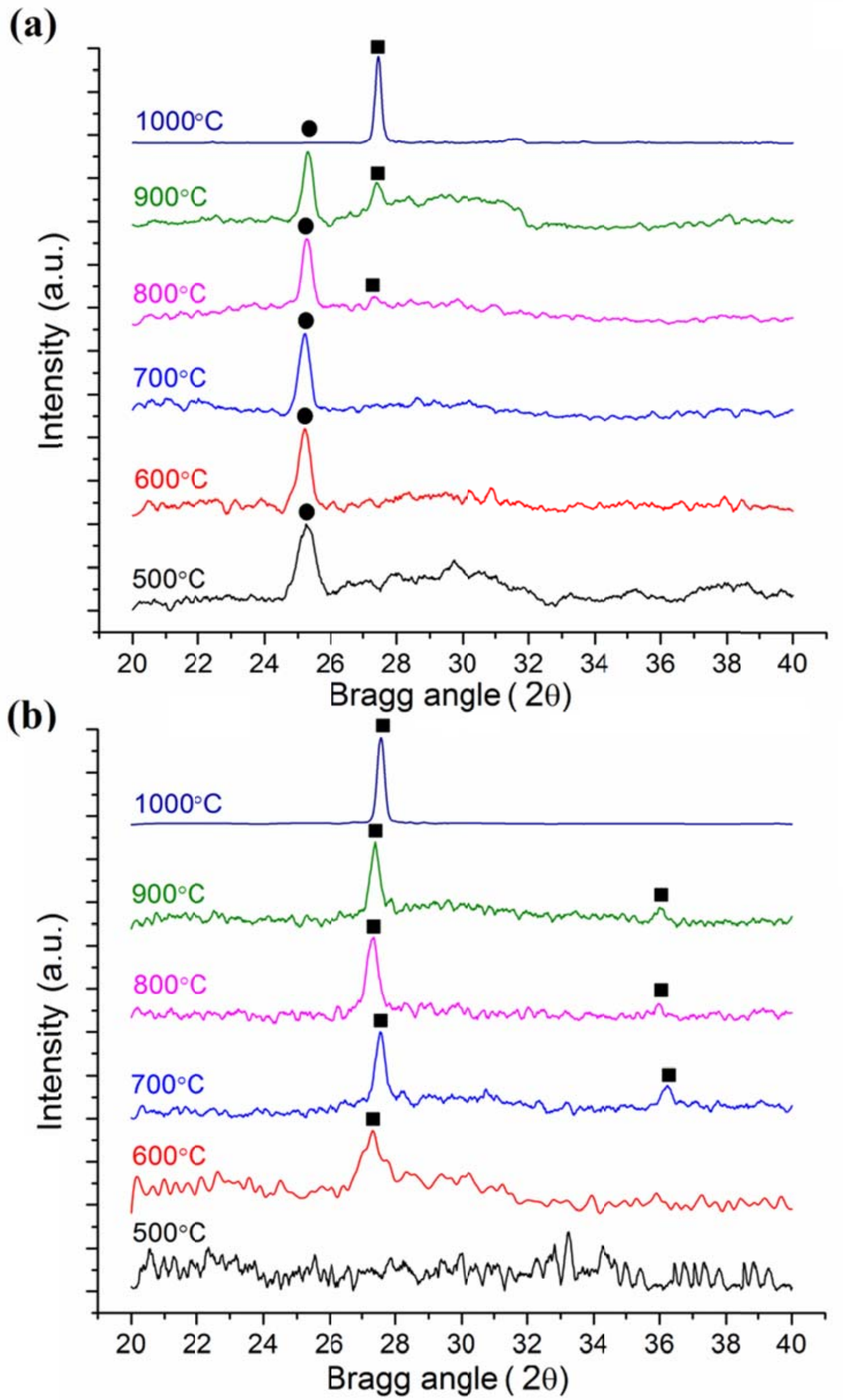

Figure 3-21: XRD patterns of the films calcined at various temperatures (a) in air and (b) under nitrogen. ●: anatase, ■: rutile.

Crystal size of the films calculated from their respective XRD patterns by Scherrer equation is reported in Table 3-6. It is important to note that there is only a small change in the crystal size up to 900°C with the film thickness being the most probable limiting factor for grain growth. A significant growth is shown by a drastic increase in the peak intensity and decrease in background noise at 1000°C, when formation of rutile occurs. Note that the Scherrer equation is not applicable to strongly anisotropic films with an average lateral crystal size larger than the film thickness.

Table 3-6: Summary of XRD crystal size measurements.

*** = Amorphous film or Scherrer equation is not applicable.**

Temperature	**Crystal Size**	
	Air	**N_2**
400°C	16 nm	*
500°C	22 nm	*
600°C	23 nm	18 nm
700°C	23 nm	27 nm
800°C	27 nm	27 nm
900°C	*	28 nm
1000°C	*	*

Raman spectra of the films are shown in Figure 3-22. Films calcined in air showed anatase bands at 144cm^{-1} (B_{1g}), 198cm^{-1} (B_{1g}, A_{1g}), 398cm^{-1} (B_{1g}) and 640cm^{-1} (E_g) (Ocaña, Garcia-Ramos et al. 1992) beginning from the lowest calcination temperature of 400°C. Contrary to the Raman analysis, XRD was unable to detect crystallinity for the film calcined at 400°C in air, which can be explained by the particular sensitivity of Raman spectroscopy to nanocrystals in thin films (Yakovlev, Scarel et al. 2000). This shows the necessity of using complementary techniques for characterizing such thin films. Position of the lowest frequency anatase band (144 cm^{-1}) is an important indicator of the particle size in TiO_2 films due to phonon confinement effect (Balaji, Djaoued et al. 2006). Oxygen deficiency and stress levels can also affect the position of Raman bands, although the contribution of the former should be negligible in our samples because they were calcined in an oxygen-rich atmosphere (air). The lowest frequency anatase band positions for air-calcined samples are shown in Figure 3-22d. Smaller blue shifts were observed with increased calcination temperature due to increased particle size. At the maximum calcination temperature (1000°C), only rutile bands 442 cm^{-1} (E_g) and 610 cm^{-1} (A_{1g}) (Ocaña, Garcia-Ramos et al. 1992) were detected, in agreement with the XRD findings. For films calcined under nitrogen, it was difficult to separate the rutile peaks at low calcination temperatures because of the overlapping positions of the rutile bands with the weak Si bands coming from the substrate (433 cm^{-1} and 621 cm^{-1}). At the maximum calcination temperature (1000°C), signals coming from rutile were stronger, showing rutile bands at 439 cm^{-1} and 610 cm^{-1}. Slight red-shift of the E_g mode of rutile in nitrogen-calcined films can be explained by the disruption of the planar O-O interactions due to oxygen vacancies (Parker and Siegel 1990).

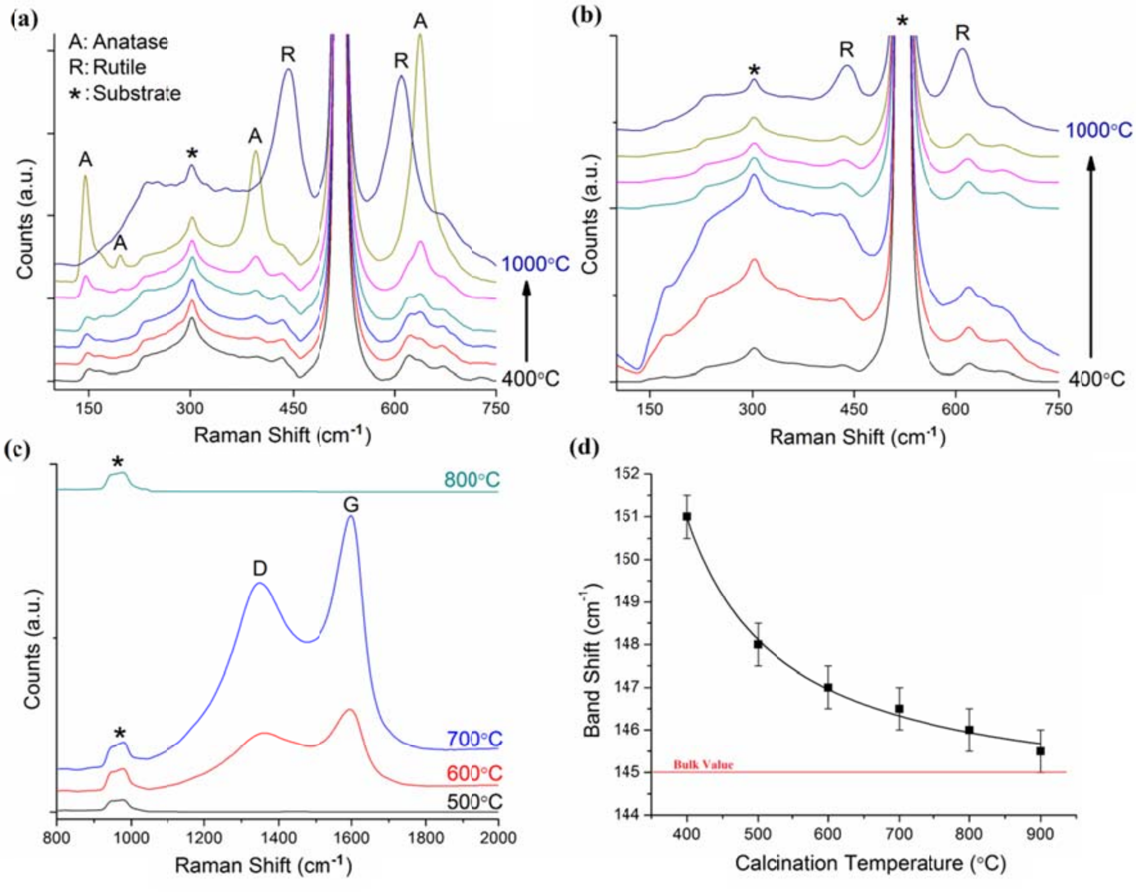

Figure 3-22: Raman spectra of the films calcined at various temperatures in (a) air and (b) nitrogen. Carbon range of the Raman spectra of nitrogen-calcined films is shown in (c). Spectra in (c) have been normalized using the peak of Si at 960 cm^{-1}. (d) The lowest frequency anatase band positions for air-calcined samples with respect to calcination temperature.

As evidenced by the XRD and Raman spectra, calcination environment has a dramatic impact on the structure of TiO_2 films. Calcination under nitrogen hindered the crystallization of the films, possibly due to the incomplete decomposition of organic titanium compounds (e.g. acetylacetonates). For samples calcined at 600°C and 700°C, organic matter had seemingly decomposed into carbon, for which D and G bands (Tan, Dimovski et al. 2004) were detected (Figure 3-22c). Lack of carbon above 700°C in nitrogen-calcined films can be explained by the fast decomposition of low-carbon yield organics before densification of the film takes place. Another possibility is a reaction between carbon and TiO_2 leading to oxygen deficit films. While the exact reason is not clear, loss of carbon at higher calcination temperatures under nitrogen for carbon coated TiO_2 has been reported (Tsumura, Kojitani et al. 2002). Preferred occurrence of rutile in nitrogen-calcined samples can be explained by two reasons: (a) since the anatase to rutile transformation requires shrinkage of the lattice, removal of oxygen atoms facilitates this transformation (Shannon and Pask 1965), (b) partial hydrogenation of the TiO_2 (due to the delayed decomposition of acidic precursor), which further promotes rutile formation (Barnard and Zapol 2004). No carbon peaks have been observed after calcination in air, suggesting complete burn off of the organic material. Carbon formed in nitrogen-calcined films could act as a reducing agent in the presence of nitrogen (Jha and Yoon 1999), creating oxygen-deficient TiO_2 films.

SEM inspection of the films (Figure 3-23) has shown differences in morphology between air- and nitrogen-calcined samples. Air-calcined films were typically composed of closely packed TiO_2 grains (ca. 20 nm) at 600°C, which began sintering at 900°C forming a mix of small (ca. 40 nm) and large (ca. 200 nm) particles and finally forming large flat grains(ca. 0.5 µm in x-y direction) at 1000°C. Formation of textured (as shown by XRD) and separated rutile crystals with at the maximum calcination temperature can be explained by the dissolution of some of TiO_2 in the SiO_2 (Emili, Incoccia et al. 1985). Films calcined under nitrogen were porous with a smaller average grain size at all temperatures with grain growth that was less dramatic compared to the air-calcined samples, which was an important finding given that rutile had been shown to grow faster than anatase in many cases (Chen and Mao 2007). On the other hand, crystal growth in thin films is significantly affected by the underlying substrate. This effect can be clearly seen in Figure 3-24, where crystals were significantly larger around the edge of a micro-crack compared to the crystals in the middle of the film. At the maximum calcination temperature (1000°C), porosity disappeared, but the crystal size remained small. TEM analysis performed on the samples calcined at 900°C is shown in Figure 3-25. It can be seen that the air-calcined film had well developed crystals whereas at the same temperature nitrogen-calcined film had much smaller crystals with rough crystal faces, possibly due to reaction with carbon.

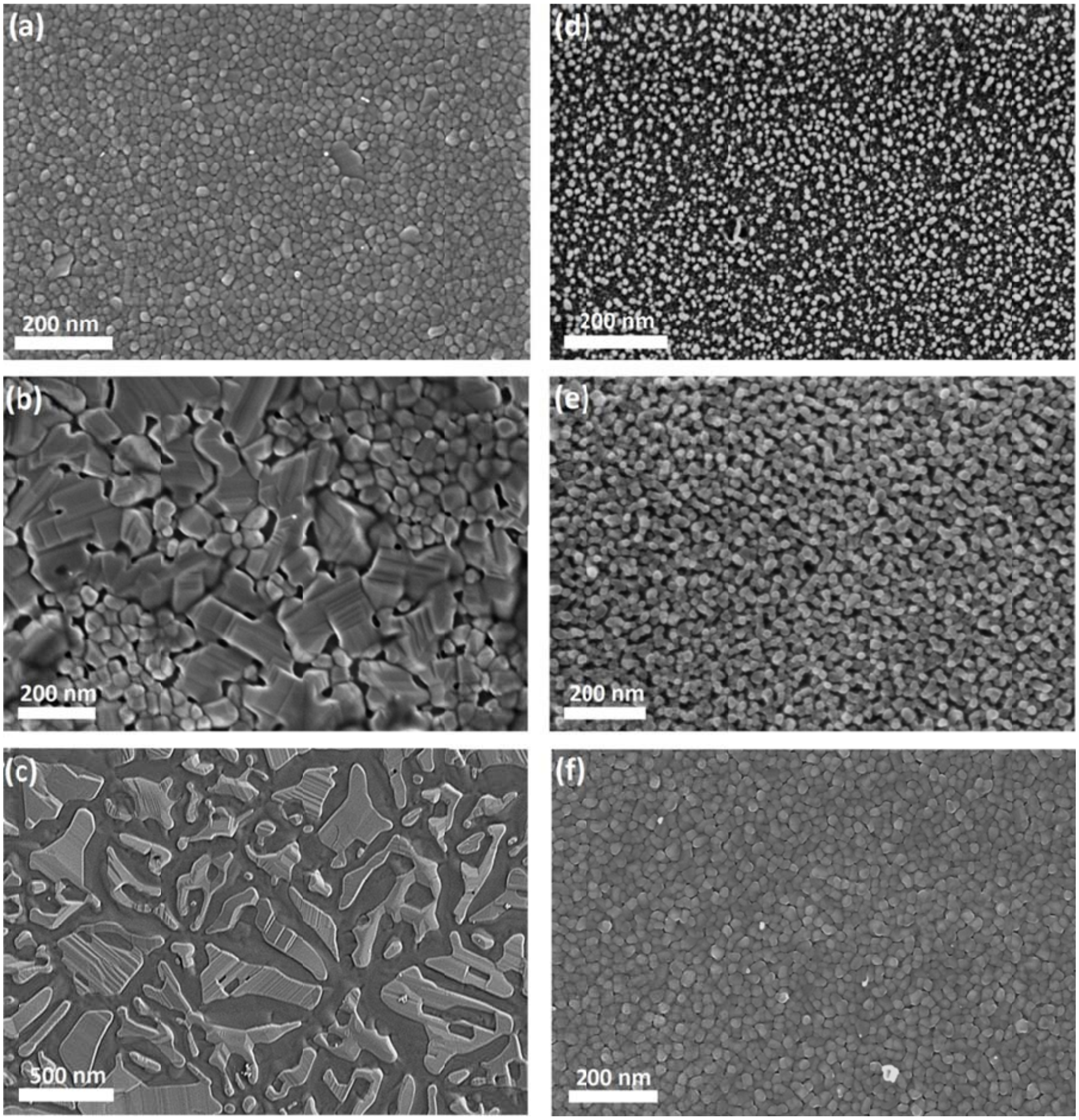

Figure 3-23: Morphological evolution of the films calcined at 600°C (a, d), 900°C (b, e) and 1000°C (c, f). a, b, c belong to the films calcined under nitrogen.

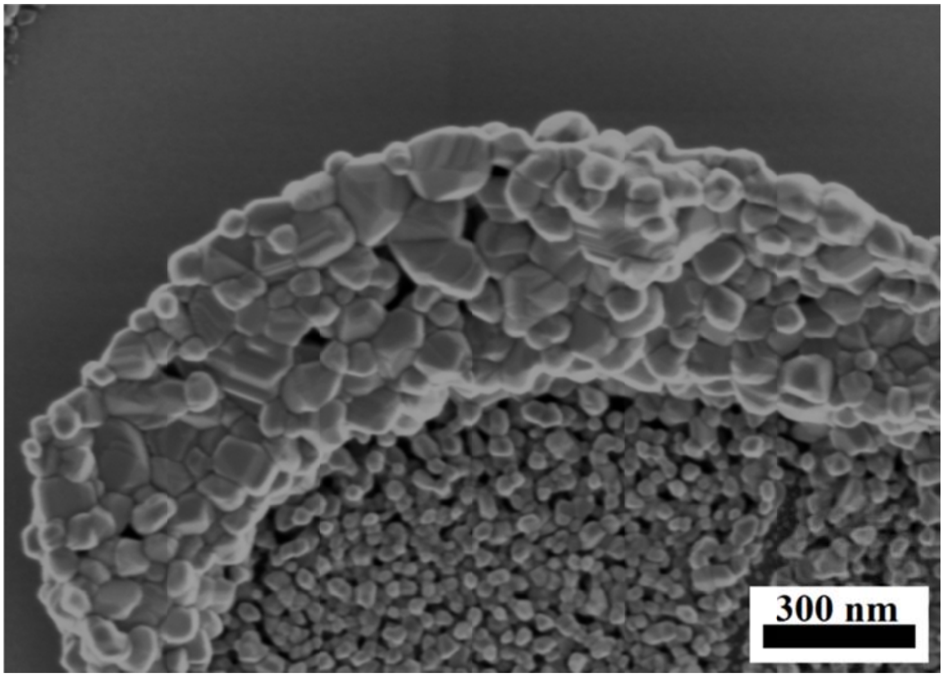

Figure 3-24: SEM image around a micro-crack showing the extensive growth of TiO_2 particles on the edge.

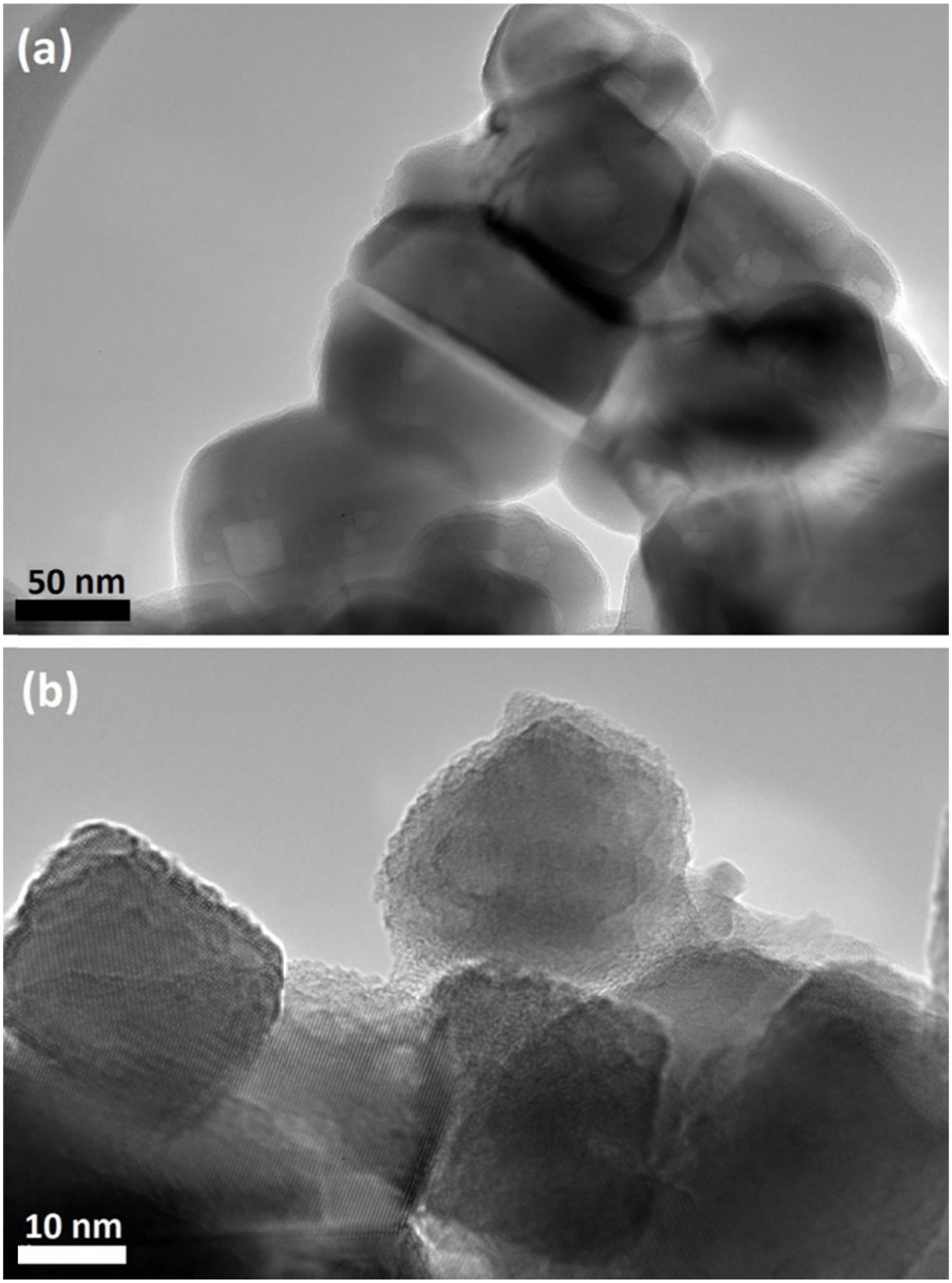

Figure 3-25: TEM images of the films calcined at 900°C in (a) air and (b) nitrogen.

Total reflectance spectra of the films are shown in Figure 3-26. Overall, films calcined under nitrogen were significantly less reflective compared to the air calcined films. This behavior should be arising from (a) presence of optically absorbing carbon, and (b) rougher surface, (c) entrapment of light within the porous structure. Films calcined between 400°C and 700°C in air had similar spectra, whereas at 800°C and 900°C there is a significant red-shift with increased reflectivity, which is expected because of the higher refractive index and smaller band gap of rutile compared to anatase. At 1000°C, incomplete coverage of the Si wafers due to a dramatic increase in the grain size in lateral dimension (as evident from the SEM inspection) and the possible growth of silica under layer caused a different pattern. Nitrogen-calcined films became more absorbing with increased calcination temperature until 700°C due to formation of carbon in the film. At 800°C and 900°C, the films were slightly more reflective, owing to the disappearance of carbon from the film and the densification of the structure. At 1000°C, the film was significantly more reflective due to disappearing porosity.

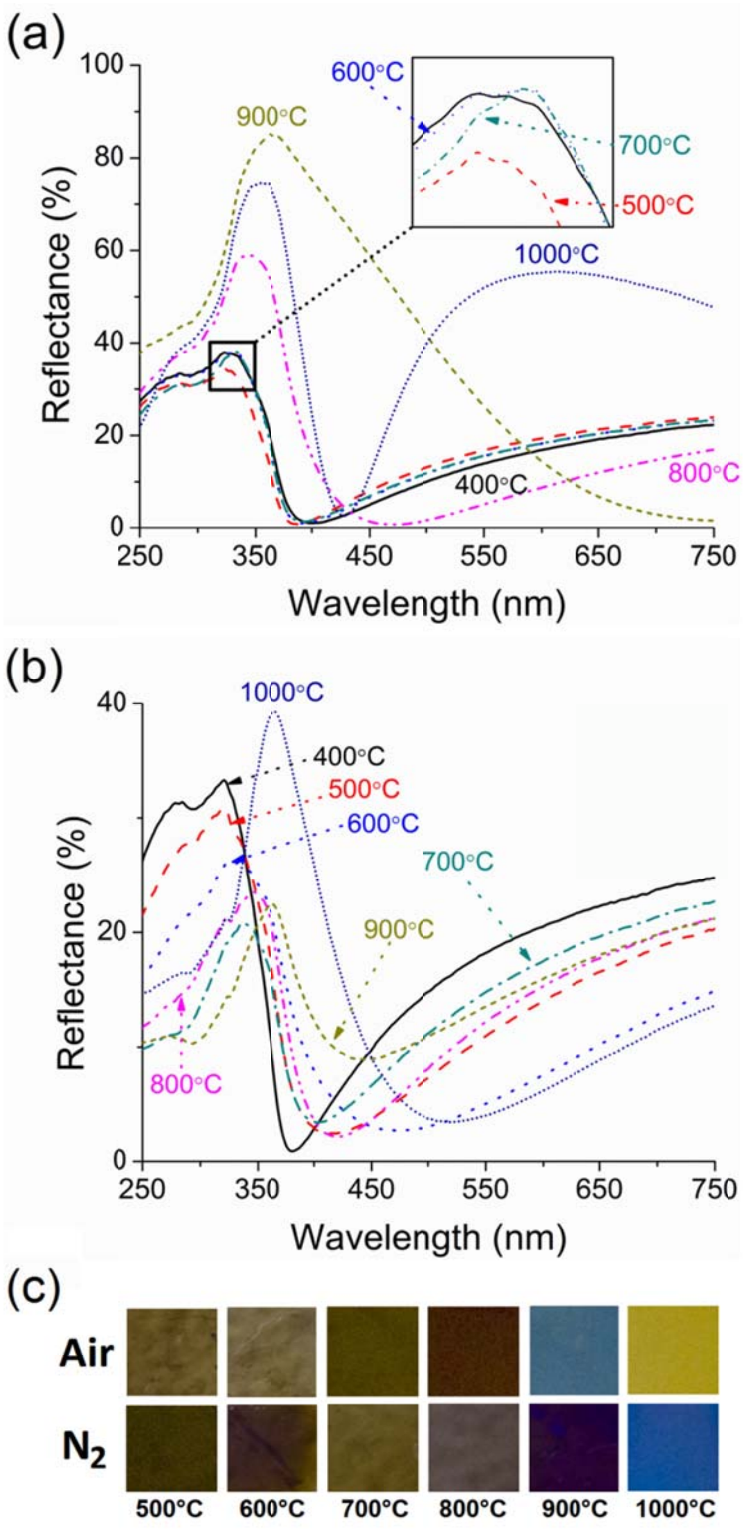

Figure 3-26: **Optical spectra of TiO_2 films calcined in (a) air and (b) nitrogen. Sample photographs are shown in (c).**

Reflection maximums (absorption minimum or edge) of the films are plotted in Figure 3-27 in order to better understand the densification behavior and electronic structure of TiO_2 films. Reflection maximum of the films shifted to lower energies, i.e. longer wavelengths, indicating a narrowing of the band gap and increase in refractive index due to densification. At low calcination temperatures (400°C-600°C), films calcined in air had smaller reflection maximums due to their better crystallinity. Upon crystallization, nitrogen-calcined films had lower values compared to air-calcined samples, which can be explained by their higher rutile content which has a higher refractive index compared to anatase. There is almost a linear decrease in the reflection maximum of air-calcined films between 700°C and 1000°C which can be attributed to the increased rutile content. For nitrogen-calcined films, the decrease in the reflection maximum is probably related to the formation of oxygen vacancies and densification of the rutile film.

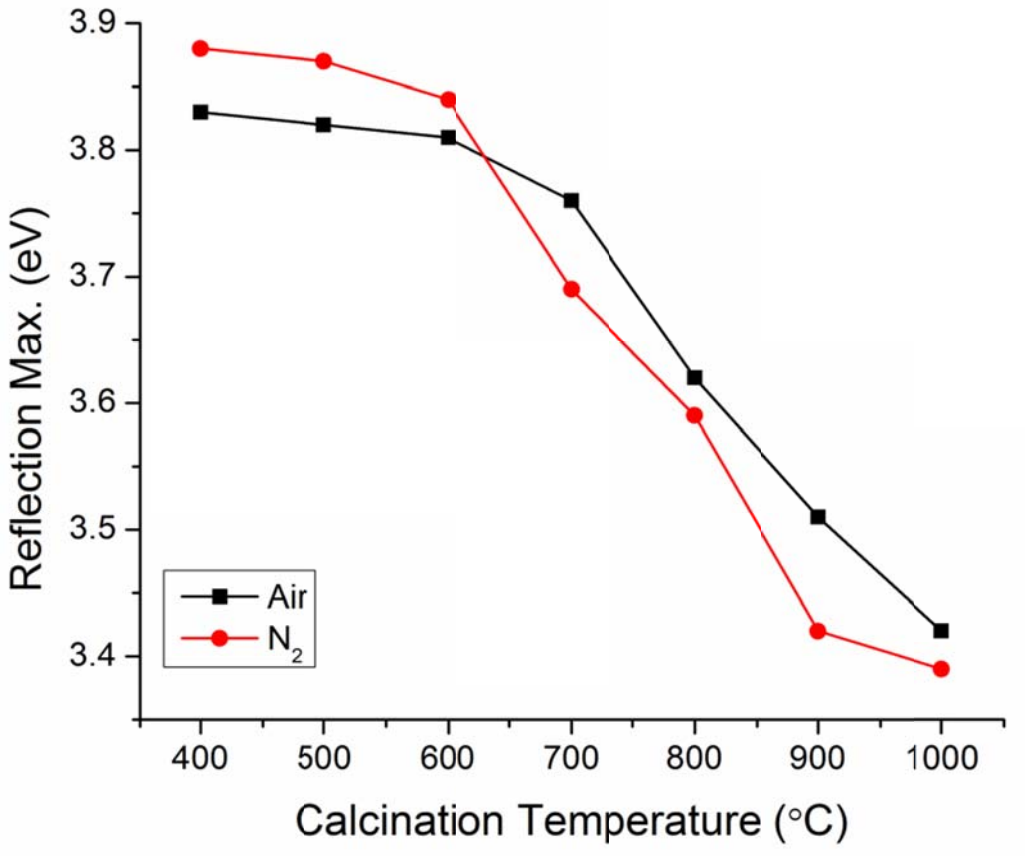

Figure 3-27: Reflection maximums of films with respect to the calcination temperature and environment.

Photocatalytic activity of the films under UV light and visible light is shown in Figure 3-28. Methylene blue was chosen as a model pollutant to assess the photocatalytic activity. It should be emphasized that degradation pathways of methylene blue are different under UV and visible light irradiation, in which the former one proceeds by photo-oxidation whereas the latter involves photo-sensitized decomposition and photo-oxidation depending on the nature of the catalyst (Konstantinou and Albanis 2004).

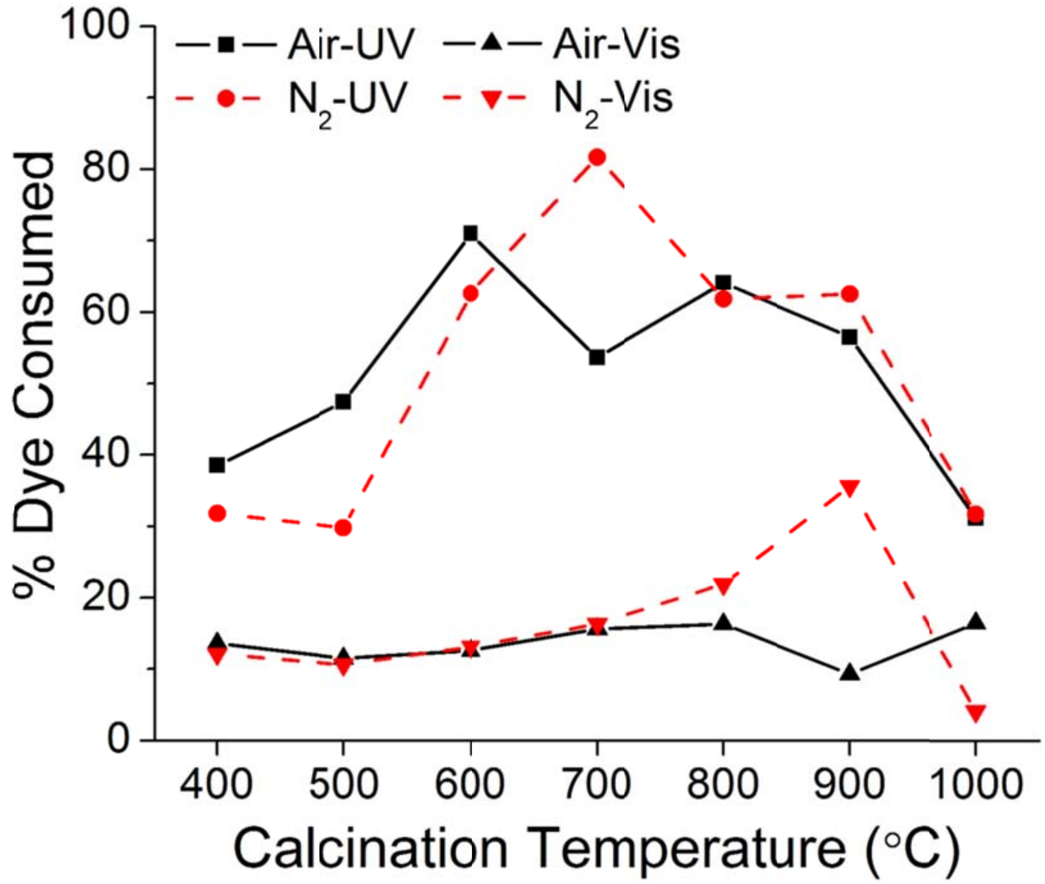

Figure 3-28: Photocatalytic activity of the films as obtained from methylene blue decomposition test.

Degradation of methylene blue in low concentrations (few ppm) follows a first-order reaction rate given by (Konstantinou and Albanis 2004):

$$\ln\left(\frac{C_0}{C}\right) = k \cdot t \quad (1)$$

where C, C_0, k, and t are the MB concentration, initial MB concentration, rate constant, and time, respectively. Calculated rate constants are given in Table 3-7.

Table 3-7: Calculated first-order photocatalytic rate constants of the films.

Calcination Temp. (°C)	Rate Constant (hr^{-1})			
	UV-Air	UV-N_2	Vis-Air	Vis-N_2
400	*0.10*	*0.08*	*0.03*	*0.03*
500	*0.13*	*0.07*	*0.02*	*0.02*
600	*0.25*	*0.20*	*0.03*	*0.03*
700	*0.15*	*0.34*	*0.03*	*0.04*
800	*0.20*	*0.19*	*0.04*	*0.05*
900	*0.17*	*0.20*	*0.02*	*0.09*
1000	*0.07*	*0.08*	*0.04*	*0.01*

Photocatalytic activity of TiO_2 films depend on several factors including but not limited to crystal structure (Bickley, Gonzalez-Carreno et al. 1991), particle size (Zhang, Wang et al. 1998), film thickness (Yu, Zhao et al. 2000), oxygen vacancies (Nakamura, Negishi et al. 2000), optical absorption, surface area and surface chemistry (Ohtani, Okugawa et al. 1987). At low calcination temperatures (400°C-600°C), better crystallization of air-calcined samples ensured a higher photocatalytic response compared to the nitrogen-calcined samples, as amorphous TiO_2 is known to be a poor photocatalyst (Ohtani, Ogawa et al. 1997). At 700°C and above, nitrogen-calcined samples had slightly better photocatalytic activity compared to air-calcined samples. Although films calcined under nitrogen between 700°C and 900°C had similar particle size, optical absorption and the same crystal structure, the one calcined at 700°C exhibited the most photocatalytic activity. This behavior can possibly be attributed to the beneficial effect of carbon on the adsorption of methylene blue (Tsumura, Kojitani et al. 2002). Photocatalytic activity of the films was significantly degraded when the calcination temperature reached 1000°C in both atmospheres. This can be explained by the decreased surface area and {110} orientation of the rutile crystals as the {110} face of rutile is an active reducer whereas oxidation reactions preferentially occur on the {011} face (Ohno, Sarukawa et al. 2002).

Degradation of methylene blue under visible light occurs by photo-sensitization for non-visible light active photocatalysts (i.e. air calcined films in this study) whereas it is a combination of photo-oxidation and photo-sensitization for visible light active photocatalyst (nitrogen-calcined films in this study). Degradation of methylene blue by TiO_2 under UV light can generally be expressed as

$$MB \xrightarrow{h\nu} MB^{\bullet +} \quad (2)$$

$$MB \xrightarrow{h\nu + TiO_2} MB^{\bullet +} \quad (3)$$

where reaction (2) and (3) are the photolysis of MB by UV irradiation and the photo-oxidation driven by TiO_2, respectively. Reaction (2) was ruled out by normalization of the data with respect to a blank sample irradiated with UV light in the absence of TiO_2. On the other hand, visible light bleaching, in addition to the reaction (3), involves the sensitization of MB to its triplet state (reaction 4) followed by electron injection to TiO_2 conduction band (reaction 5) (Mrowetz, Balcerski et al. 2004):

$$MB \xrightarrow{h\nu} MB^{*} \quad (4)$$

$$MB + TiO_2 \rightarrow MB^{\bullet +} + TiO_2(e^-) \qquad (5)$$

Visible light degradation of MB is driven mainly by reactions (3) and (5), where reaction (3) is non-existent in non-visible light active catalysts. Reaction (5) strongly depends on the absorption behavior of MB on the catalyst in order to provide an efficient electron injection (Park and Choi 2004). Since a significant change in the conduction band position is not expected in our films, the differences in the visible light activity of films can be attributed to the visible light photo-oxidation (reaction 3) and/or increased absorption of MB to the film surface.

Visible light photocatalytic activity of most of the samples was low compared to their activity under UV-light, with the exception of the sample calcined at 900°C under nitrogen, which produced a significant visible-light photocatalytic activity. The improved visible-light photocatalytic activity was attributed to the oxygen-deficient structure of TiO_2 (Nakamura, Negishi et al. 2000; Justicia, Ordejón et al. 2002) in nitrogen-calcined films. As explained before, the increased activity can be attributed to either reaction (2) or (4-5). A higher content of OH groups can be attained by non-stoichiometric TiO_x ($0 < x < 2$) (Carp, Huisman et al. 2004), which improves the rate of reaction (5) due to increased adsorption of a cationic dye such as MB. However, we have not detected any difference in their adsorption behavior between films calcined at 700°C, 800°C, 900°C, (MB concentrations were measured after films were kept in dark for 1 hr to equilibrate adsorption before illumination) yet there are significant differences in their respective photocatalytic activity under visible light. Therefore, the difference should be coming from reaction (3), i.e. photo-oxidation process by TiO_2. Although rutile has been reported to have higher visible light photocatalytic activity compared to anatase (Yin, Hasegawa et al. 2004), we don't think this was the reason for this behavior as other films with rutile didn't perform as well. On the other hand, the absorption edge of the film calcined at 900°C under nitrogen was more red-shifted compared to others (Figures 6-7b and 8), which can explain its higher photocatalytic activity in the visible light. However, the exact mechanism for this behavior still requires further study.

In general, all of the films have shown good adhesion to the substrate with resistance to peeling off by a scotch tape. No film bulging or delaminating was observed after indentation and scratch testing. Nanoindentation results (Figure 3-29) have shown that films calcined in air had higher overall hardness and modulus compared to the ones calcined under nitrogen. The lower hardness of nitrogen-calcined samples was possibly as a result of the porous nature and a lower crystallinity of the films as evidenced by the SEM images. Also, films calcined at low temperatures (<800°C) had better mechanical properties while an almost complete elastic recovery was observed for amorphous films. Nanoindentation results of thick anatase and rutile films prepared by magnetron sputtering have been reported before, where hardness of anatase and rutile were found to be 8 GPa and 17 GPa, respectively (Zywitzki, Modes et al. 2004). Mechanical properties of the films calcined at lower temperatures are close to that of anatase. Rutile was reported to have a significantly higher modulus (260 GPa) compared to anatase (170 GPa) (Zywitzki, Modes et al. 2004). However, since the films in this study were very thin (30 nm), the results reflect the substrate influence where reported modulus and hardness values for Si (100) are around 165-178 GPa and 12-13.3 GPa, respectively (Li, Bhushan et al. ; Juliano, Domnich et al. 2004; Gaillard, Rico et al. 2009).

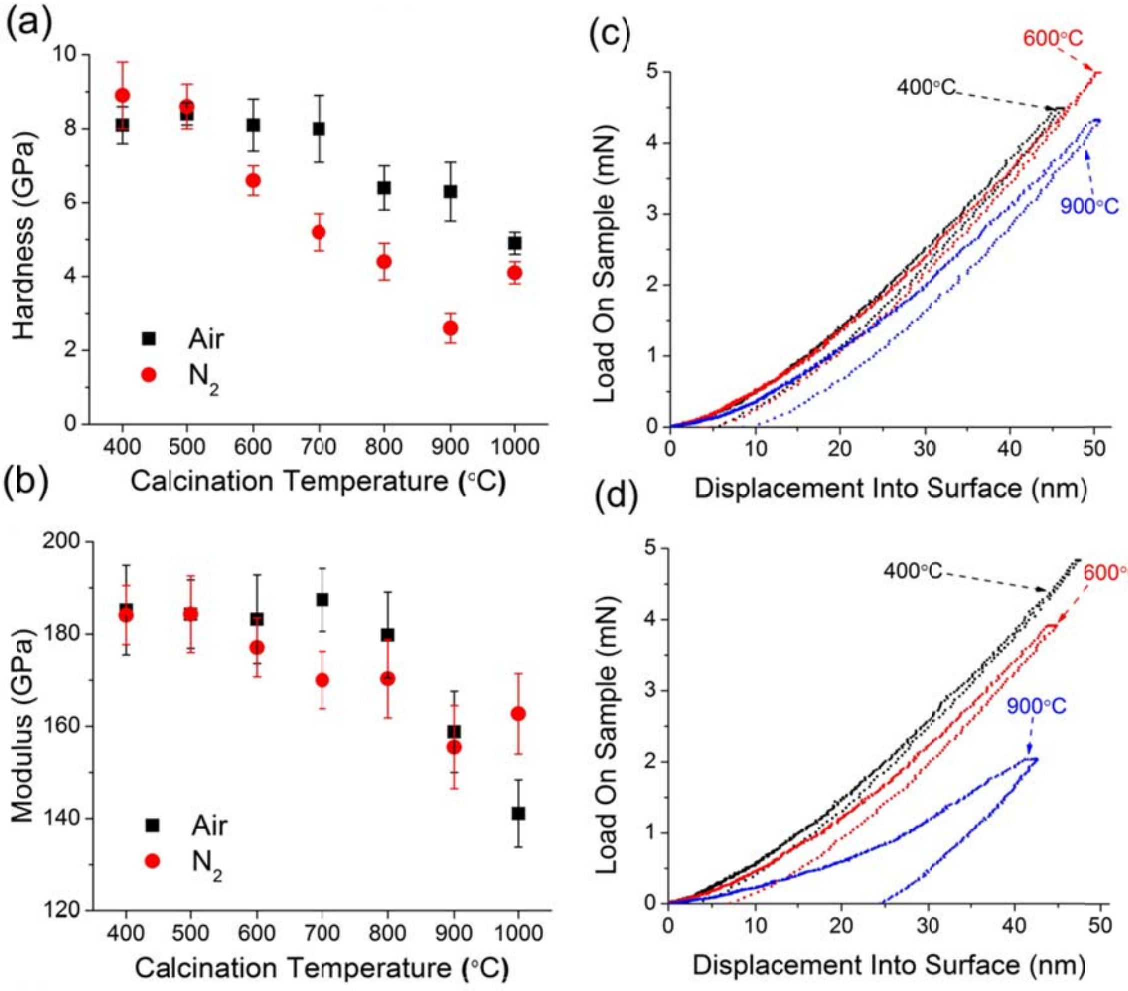

Figure 3-29: (a) Indentation hardness and (b) modulus of the films with respect to the calcination temperature and environment. Load-displacement curves of the films calcined at 400°C, 600°C and 900°C under (c) air and (d) nitrogen.

Deterioration of mechanical properties in films calcined under nitrogen may also be attributed to the tensile stresses which arose due to the oxygen vacancies (Bhatia and Sheldon 2008), which also explains the porous nature of the films. Presence of soft graphitic carbon in these films (Fig.2c) may provide another reason for lower mechanical properties. Large residual inelastic deformation of the film calcined at 900°C under nitrogen (Figure 3-29d) can be attributed to the high porosity. Partial recovery of the film hardness after calcination at 1000°C in nitrogen can be explained by the formation of a sintered nanocrystalline film with less porosity (Figure 3-23f). Thus, calcination at lower temperature leads to improved mechanical properties and should be used when abrasion resistance is of critical importance (e.g. window glass).

3.3.4. Conclusions

Titanium dioxide films were carbothermally reduced at a wide range of temperatures and the resulting oxygen-deficit films were analyzed in terms of their crystal structure, morphology UV and visible light photocatalytic activity and mechanical properties. It is found that calcination of titanium dioxide films in a reducing atmosphere leads to formation of rutile phase, while this does not result in decreased photocatalytic activity in contrast to the fact that anatase is usually a better photocatalyst than rutile. Visible light active titanium dioxide films are obtained at sufficiently high calcination temperatures in reducing atmosphere. However, this resulted in significant degradation of mechanical properties which may or may not be important depending on the requirements of the particular practical application. It is also important to note that the required calcination conditions for visible light activity can only be applied to a limited number of glass types as the majority of glass substrates experiences significant deformation at those temperatures.

3.4. Metal Doped Titanium Dioxide Films

3.4.1. Introduction

Six different metal-doped titanium dioxide films on soda-lime glass substrates were synthesized. The effects of individual metal dopants on the structure, photocatalytic and mechanical properties were analyzed while particular attention was given to the interaction of metal dopants with the poisoning effect of sodium diffusing from the substrate.

3.4.2. Experimental

Pure and doped TiO_2 coatings were prepared using the following sol-gel method: 50 g anhydrous 2-propanol (Alfa-Aesar), 50 g anhydrous 1-butanol (Alfa-Aesar), 20 g titanium iso-propoxide (Sigma Aldrich, 98%) and the dopant source ($AgNO_3$, $CoCl_2$, $Cu(C_5H_7O_2)_2$, $GaCl_3$, $MoCl_5$,or $TaCl_5$) were mixed and subsequently stirred on a magnetic stirrer for 30 minutes. Dopant concentration in all films was fixed at 1% mol. Then a mixture of 3 g de-ionized (DI) water (Millipore, 18MΩ) and 1.3 g HNO_3 (Sigma-Aldrich, 70%) was added drop-wise to the solution and stirred for 2 hours.

Films were prepared by dip coating (MTI Dip Coater HL-01). For this purpose, soda-lime glass microscope slides (Erie Scientific, 14.25 at.% Na_2O) were cleaned thoroughly by sonication in anionic detergent (Branson OC) solution at 60°C followed by extensive rinsing in de-ionized water, dipped into the prepared solution and withdrawn at a constant speed of 100 mm/min. To prevent sodium diffusion from the substrate, SiO_2 coated slides were prepared similarly via sol-gel process and calcined at 500°C for 1 hour before the TiO_2 coating procedure. The resulting SiO_2 layer was approximately 100 nm. Following the coating procedure, samples were calcined in a muffle furnace for 30 min at 500°C with a heating rate of 5 °C/min.

Raman spectra were measured using a 514.5 nm Ar-ion laser as the excitation source (Renishaw RM1000). Optical spectra were collected by a UV-Vis Spectrophotometer (Thermo Scientific Evolution 600). SEM images of the films were collected using a Zeiss Supra 50VP. Film thickness was measured with a spectroscopic ellipsometer (J.A. Woolam M-2000U/EC-400) at an incident angle of 70°. Infrared spectra of the films were recorded with Varian Excalibur FTS-300 FTIR Spectrometer with an external reflectance accessory at an angle of 80°.

Photocatalytic activity of the films was evaluated by methylene blue degradation test. For this, coated slides (2.5 cm x 2.5 cm) were placed in dishes containing 15 ml 2 ppm aqueous methylene blue solution and kept in dark for 30 min, and then illuminated with UVC light (16 W, λ = 254 nm) for 3 hrs. Representative samples were taken every hour from the solutions and dye concentration was measured using a UV-Vis Spectrophotometer (Thermo Scientific Evolution 600).

3.4.3. Results and Discussion

Thickness of the films varied between 100 nm and 110 nm as determined by spectroscopic ellipsometry. For this purpose, similarly prepared films on Si (100) substrates were used. An uncoated wafer was subjected to the same calcination treatment to separately measure the oxide layer developed on the surface. Measured thickness was confirmed by cross-section analysis using SEM as shown in Figure 3-30.

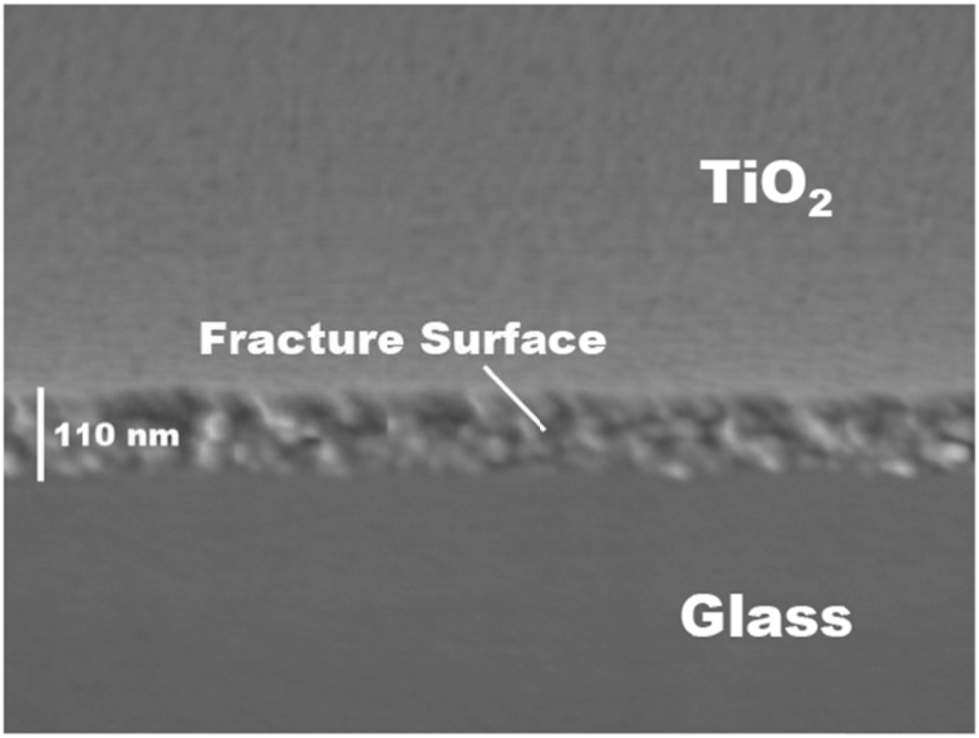

Figure 3-30: SEM image of a fracture surface of TiO_2 film on Si (100). The image was taken at a 75° angle, so the real thickness is given as $t = t_o \times \cos(75) = 101$nm, where t and t_o denotes real and observed thickness, respectively.

XRD analysis was performed on films prepared on silicon wafers as we were not able to obtain a sufficient signal from glass or glass/SiO_2 substrates due to the background signal (broad hump around the strongest TiO_2 peaks) from the amorphous substrate. Figure 3-31 shows the representative diffractograms of the samples. Note that only the range between $2\theta = 23$ and $2\theta = 28$ was analyzed since the strongest peaks of anatase and rutile are within this range. As the films were very thin, other peaks were difficult to separate from the background.

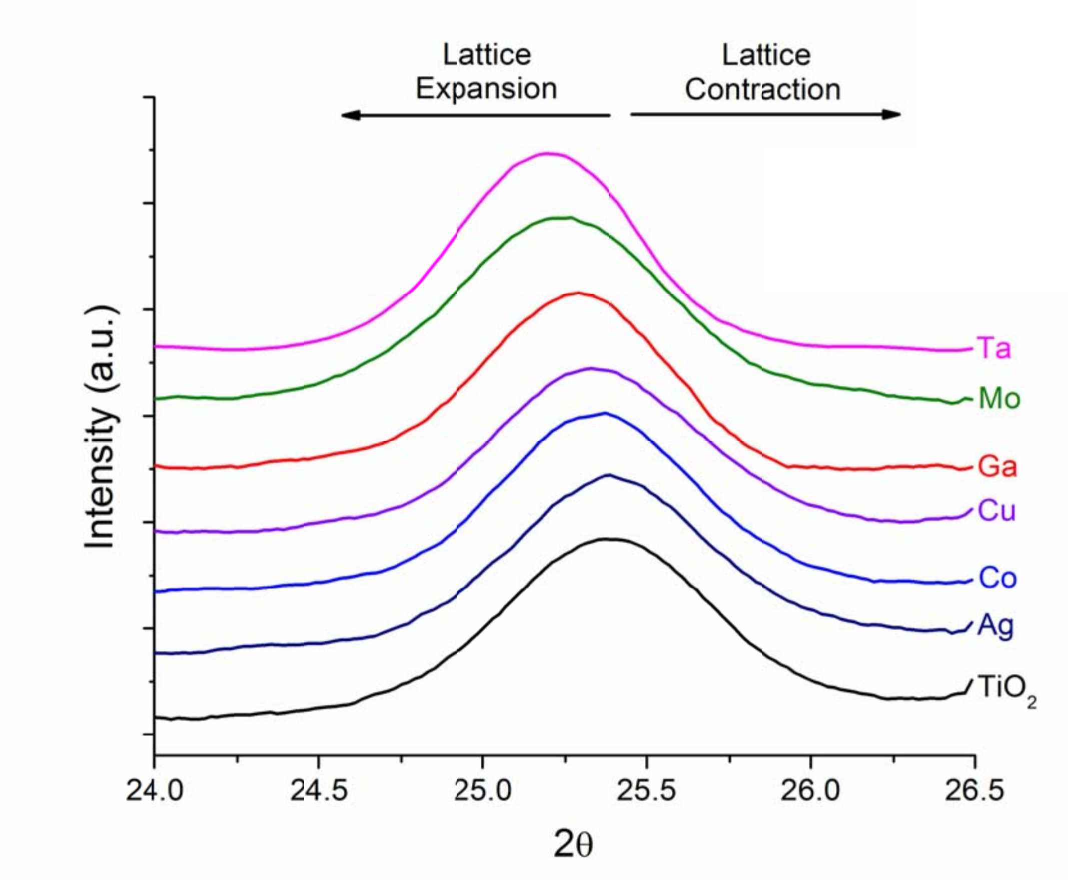

Figure 3-31: XRD patterns of the anatase (110) peak for un-doped and doped TiO_2 films.

Crystallite size of the films was calculated by Scherrer's equation:

$$D = \frac{K\lambda}{\beta \cos\theta}$$

where K, λ, β and θ are the shape factor (0.9 for spherical crystals), x-ray wavelength (0.154 nm), FWHM (in radians), and Bragg angle, respectively. Stress/strain and instrumental broadenings were neglected. Calculated values for the crystallite size of the samples and the anatase (110) peak positions are reported in Table 3-8.

Table 3-8: Crystallite size, anatase (110) peak position and ionic radiuses of the dopants

Sample	Crystallite Size (nm)	Peak Position (2θ)	Cation Radius (pm)
TiO_2	12.1	25.40	Ti^{4+} = 60.5
Ag- TiO_2	15.7	25.40	Ag^{+} = 115, Ag^{2+} = 94
Co- TiO_2	13.2	25.36	Co^{2+} = 65
Cu- TiO_2	14.7	25.28	Cu^{+} = 77, Cu^{2+} = 73
Ga- TiO_2	12.3	25.28	Ga^{3+} = 62
Mo- TiO_2	12.6	25.24	Mo^{5+} = 61, Mo^{6+} = 59
Ta- TiO_2	12.8	25.20	Ta^{5+} = 64

Overall, undoped films had smaller crystallites compared to the doped films although the difference between the films with the largest crystallites (Ag-TiO_2 or undoped TiO_2= 15.7 nm) and that of smallest crystallites (undoped = 12.1 nm) was very small. The anatase peak shifted to lower angles in doped films, indicating a slight expansion of lattice by the dopant ions. Ionic radiuses of the dopants (Table 3-8) are usually larger than that of titanium, so depending on the amount of dopant dissolved in the anatase lattice, an expansion can occur. Although the most significant expansion of the anatase lattice is expected from Ag-doping because of the very large ionic radius of Ag^{+}, the very same reason also prevents Ag from entering the lattice, thus no peak shift was observed in the XRD spectra. Similar behavior for noble metals with large ionic radius has been reported before (Sakthivel, Shankar et al. 2004).

Raman spectra of the films on SiO_2 coated glass are shown in Figure 3-32a. Bands at 149 cm^{-1}, 196 cm^{-1}, and 639 cm^{-1} are assigned to the E_g modes (144, 197, 639 cm^{-1}), 396 cm^{-1} is assigned to the B_{1g} mode (399 cm^{-1}) and 515 cm^{-1} is the superposition of B_{1g} (519 cm^{-1}) and A_{1g} (513 cm^{-1}) modes of anatase (Ohsaka, Izumi et al. 1978). We were not able to detect any clear bands from the films prepared on soda-lime glass, indicating that these films were poorly crystallized due to sodium diffusion. Detrimental effect of sodium on the crystallization of TiO_2 films was reported before (Tada and Tanaka 1997).

FTIR reflection spectra of the films along with SiO_2 coated glass are shown in Figure 3-32b. Bands at 570 cm^{-1}, 825 cm^{-1}, and 1274 cm^{-1} are assigned to the transverse-optical (TO) rocking motions of ν(Si-O-Si), TO symmetric ν(Si-O-Si) stretching, and TO asymmetric ν(Si-O-Si) stretching vibrations, respectively. 1110 cm^{-1}, 1185 cm^{-1} and 1274 cm^{-1} bands are assigned to the longitudinal-optic (LO) – TO splitting of the vibrational modes of Si-O-Si bonds due to the Berreman effect (Berreman 1963) arising from the oblique incidence of infrared light (Innocenzi 2003).In all films, the 1110 cm^{-1} band disappeared and the 1185 cm^{-1} band became more distinct, possibly due to two broad TiO_2 bands located at 1051 cm^{-1} and 1143 cm^{-1}(Maity, Rana et al. 2001). A new band appeared at 981 cm^{-1} in Mo-, Co-, Ga-, and Cu-doped films which can be attributed to the Ti-O-Si bonds(Dutoit, Schneider et al. 1995). The intensity of this band was considerably higher in Mo-doped films which can be due to a hidden band coming from Mo-O species which are active in the 800-1200 cm^{-1} region (Maity, Rana et al. 2001).

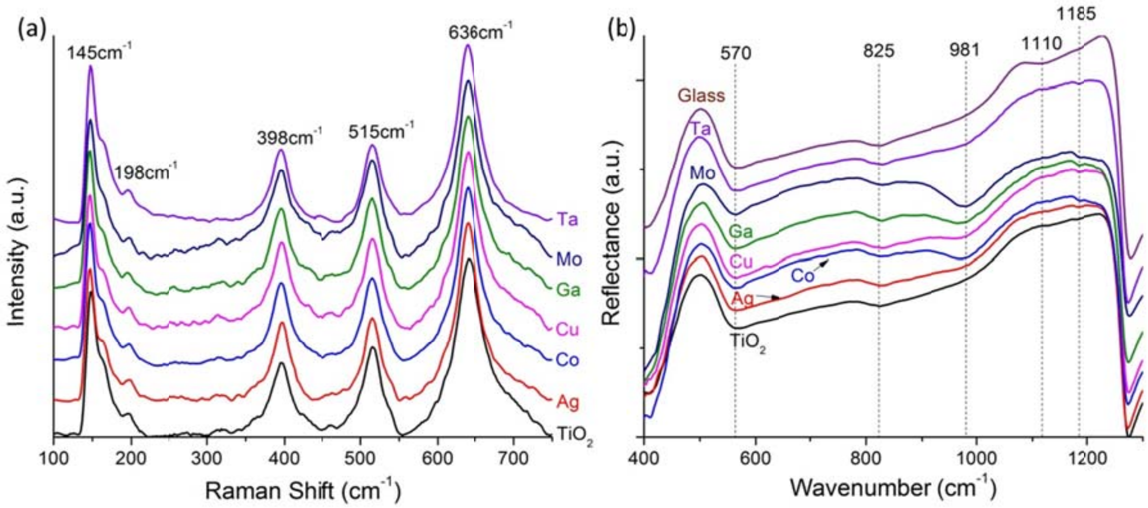

Figure 3-32: Raman spectra of un-doped, Ag-, Co-, Cu-, Ga-, Mo-, and Ta-doped films (a) and FTIR reflection spectra near grazing angle (80°) of the films on SiO_2 coated glass (b).

On soda-lime glass, most dopants caused slight blue-shift of the absorption edge of films on glass. In particular, the calculated band gap of Ag-doped films showed a significant increase. Such an increase in the band gap can be caused by quantum size effect, formation of a new compound, or change in the crystal structure. Quantum size effect has shown to be relevant to very small TiO_2 particles (< 3 nm) (Monticone, Tufeu et al. 2000), which is not possible in our case and formation of a new compound between Ag and TiO_2 is not likely due to the differences in the ionic radius of Ag and Ti. On the other hand, silver-sodium inter-diffusion can cause more sodium to diffuse into the film and promote formation of sodium titanates instead of TiO_2.

For all doped films prepared on SiO_2 pre-coated glass substrates, except Mo-TiO_2, the absorption edge showed slight red shifts. Ag- and Cu-doped films on SiO_2 coated glass had the smallest calculated band gaps. Red-shift in the absorption edge of Ag-doped

TiO_2 was reported before (Rengaraj and Li 2006; Zhang, Wang et al. 2008). Rengaraj et al. (Rengaraj and Li 2006) have reported a band gap value of 3.07 eV for 1% Ag-doped films which is in agreement with our results (3.08 eV). It has been reported that silver tends to form oxides AgO and Ag_2O in TiO_2 at low concentrations (0.3% mol), whereas surface Ag^0 is dominant at higher Ag concentrations (5% mol) (Xin, Jing et al. 2005). The lack of a plasmonic band in the optical spectra suggests that Ag was not in the metallic form but formed an oxide. Having a narrow band gap of 1.3 eV (Tjeng, Meinders et al. 1990), Ag_2O can cause a shift in the spectra of TiO_2 to higher wavelengths (Park and Kang 2008). Similarly, Cu solubility in TiO_2 has shown to be less than 0.35 mol%, after which Cu precipitates as CuO on the grain boundaries (Larsson, Andersson et al. 1996; Kim, Kim et al. 1999; Shin, Paek et al. 2006). The red shift caused by Cu-doping can be explained by the narrow band gap of CuO (1.4eV) (Ghijsen, Tjeng et al. 1988). CuO was reported to be reduced to Cu_2O when deposited on glass substrates without pre-coating treatment (Gartner, Scurtu et al. 2004). Since Cu_2O has a wider band gap (2.1eV) compared to CuO, the red-shift on glass substrates was weaker. Red-shifts were reported for Co- (Brezová, Blazková et al. 1997; Dvoranová, Brezová et al. 2002), Ga- (Whang, Kim et al. 2005; Zhou, Zhang et al. 2006), and Ta-doped TiO_2 before.

Optical spectra of the films around their absorption edge and calculated optical band gaps are shown in Figure 3-33 and Table 3-9, respectively. Optical band gaps were calculated by finding the intercept of the plot of $(\alpha h\nu)^{1/2}$ against hv (Marquez and et al. 1992) in the region 3.7 – 4.0 eV, where $(\alpha h\nu)^{1/2}$ is linear (Figure 3-33). Absorptance was calculated by measuring transmittance and total reflectance and assuming a total thickness of 200 nm (100 nm x 2) for doped and undoped films. Plain or SiO_2 coated glasses were used as baselines.

Table 3-9: Calculated band gaps of the films.

Substrate /Element	**Calculated Band Gap (eV)**						
	TiO_2	Ag	Co	Cu	Ga	Mo	Ta
Glass	3.29	3.52	3.38	3.20	3.41	3.29	3.25
SiO_2	3.29	3.08	3.14	3.11	3.14	3.33	3.20

All of the films were transparent in the visible range with an apparent absorption tail between 310 nm and 320 nm. Relatively lower wavelength position of the tails is arising from the finite thickness of the films, which resulted in the escape of some UV light at these wavelengths. A band gap value of 3.29 eV was calculated for un-doped TiO_2, which is in fairly good agreement with the reported anatase band gap value of 3.20 eV. There was no difference in the calculated band gap values of undoped films on glass and SiO_2 coated glass, in agreement with previously reported results (Lee and Lee 2007). Although films on glass are previously shown to be amorphous or poorly crystallized, no significant difference in the absorption edge of similar sized amorphous and crystalline (anatase) TiO_2 is expected (Ohtani, Ogawa et al. 1997).

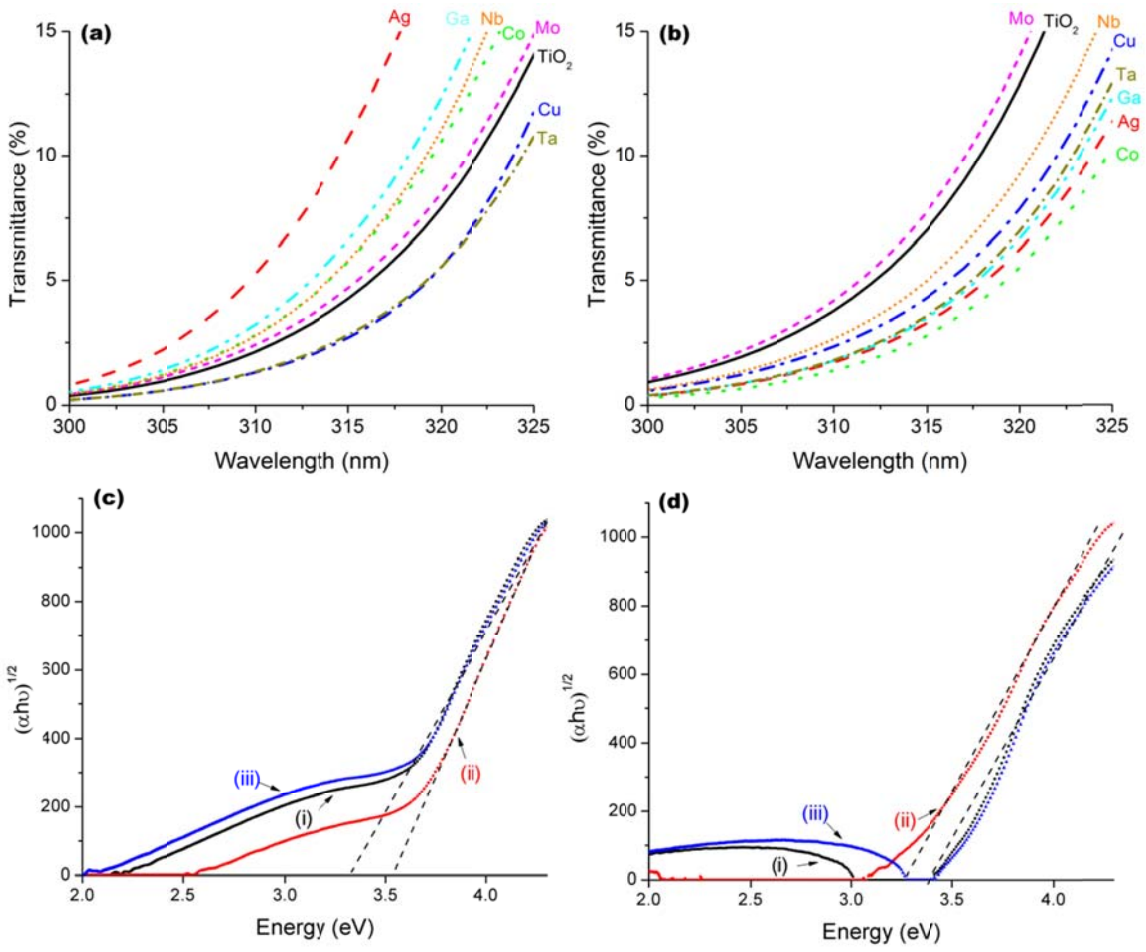

Figure 3-33: Optical spectra of the undoped and doped TiO$_2$ films on (a) glass and (b) SiO$_2$ coated glass near the absorption edge. Representative Tauc plots of (i) undoped, (ii) Ag-and (iii) Mo-doped films on (c) glass and (d) SiO$_2$ coated glass.

Methylene Blue (MB) was chosen as model pollutant for photocatalytic degradation tests. Photocatalytic degradation of MB is a first order reaction and the rate is proportional to the concentration of the dye at low concentrations (Houas, Lachheb et al. 2001) where rate constant (*k*) is given as

$$k = \frac{\ln\left[C_0\right] - \ln\left[C\right]}{t} ,$$

where C and C_0 are the concentration at time t and the initial concentration, respectively. Calculated rate constants and photocatalytic activity are reported in Table 3-10 and Figure 3-34, respectively. The lower photocatalytic rate constant of the commercially available Pilkington Activ sample compared to several of our metal-doped samples is primarily due to variations in thickness. Pilkingon's coatings are approximately 30nm thick, compared to our films with a thickness of 100-110 nm. Commercial products generally use thinner products to help retain the mechanical properties of the surface.

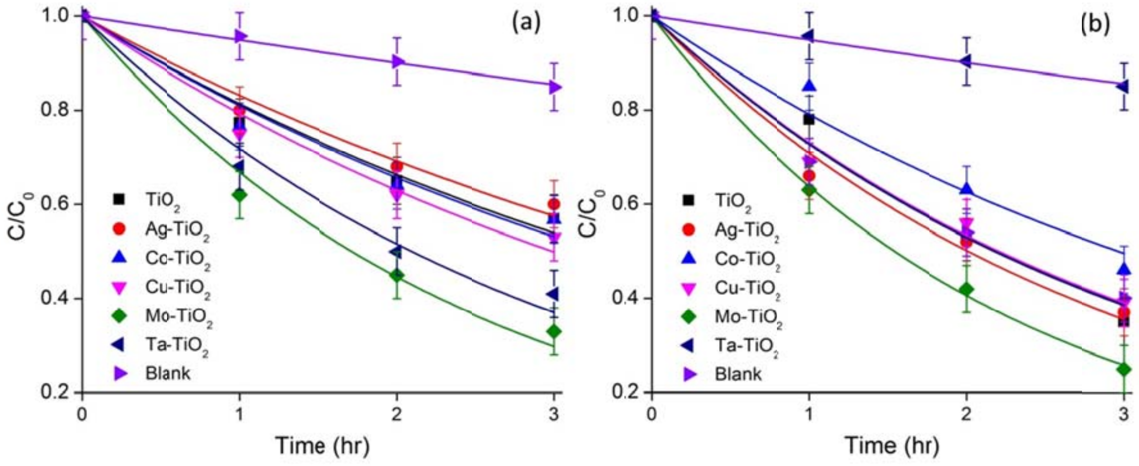

Figure 3-34: Photocatalytic activity of TiO_2 films on (a) glass and (b) SiO_2-coated glass.

Table 3-10: Methylene Blue photocatalytic decomposition rate constants (hr^{-1})

	TiO_2	Ag	Co	Cu	Ga	Mo	Ta	Blank	PA*
Glass	0.206	0.184	0.211	0.232	0.302	**0.404**	0.331	0.052	0.193
SiO_2	0.319	0.345	0.234	0.314	0.331	**0.451**	0.318		

*: Pilkington Activ

Photocatalytic activity of films on plain glass was generally inferior to the films on SiO_2 coated glasses, showing the deteriorative effects of sodium. However, this effect was much less pronounced in Mo- and Ta- films where improvement obtained by SiO_2 barrier was less than 10% compared to almost 70% improvement observed in un-doped films. In all cases Mo- and Ta-doped films performed better than undoped films. In order to understand the beneficial effects of Mo-doping on sodium poisoning of TiO_2 films on glass, a new set of samples were prepared with an increased Mo-content (5%). Increasing the Mo-content promoted the crystallization of TiO_2 films to a mixture of anatase and brookite along with some sodium molybdate as seen from the Raman spectra (Figure 3-35) while the photocatalytic activity was decreased probably due to the formation of recombination centers and/or inactive sodium molybdate phase. It is important to note that photocatalytic activity of this heavily Mo-doped film on plain glass was still better than its undoped counterpart. Another interesting finding was the observation of sodium chloride crystals on films (inset in Figure 3-35). Evidently $MoCl_5$/Mo doping had a beneficial effect of neutralizing sodium by forming sodium chloride and sodium molybdate. Formation of sodium chloride crystals was assumed to follow the reaction steps described below. Water in the environment reacts with the glass network to results in Na^+ leaching where some of the principal reactions can be given as (Grambow and Müller 2001)

$$(\equiv \mathrm{Si\text{-}O}^{\delta-} Na^{\delta+}) + \mathrm{H_2O} \rightarrow (\equiv \mathrm{Si\text{-}OH}) + \mathrm{OH}^- + \mathrm{Na}^+ \quad (1)$$

$$\mathrm{OH}^- + (\equiv \mathrm{Si\text{-}O\text{-}Si} \equiv) \rightarrow (\equiv \mathrm{Si\text{-}OH}) + (\equiv \mathrm{SiO}^-) \quad (2)$$

$$(\equiv \text{Si-O}^-) + \text{H}_2\text{O} \rightarrow (\equiv \text{Si-OH}) + \text{OH}^- \qquad (3)$$

which produces the following overall reaction:

$$\text{Na}^+(\text{glass}) + \text{H}^+(\text{env.}) \rightarrow \text{Na}^+(env.) + \text{H}^+(glass),$$

where ‘env’ indicates environment. Leached Na^+ reacts with $MoCl_5$ according to the proposed reaction:

$$7 \cdot \text{Na}^+ + \text{MoCl}_5 + 8 \cdot \text{OH}^- \rightarrow 5 \cdot \text{NaCl} + \text{Na}_2\text{MoO}_4 + 4 \cdot \text{H}_2\text{O},$$

forming sodium molybdate and sodium chloride crystals. Required water for reactions 1-3 can be supplied by humidity in air and by the decomposition of organic material inside the film matrix (alcohols, acetylacetone, etc.).

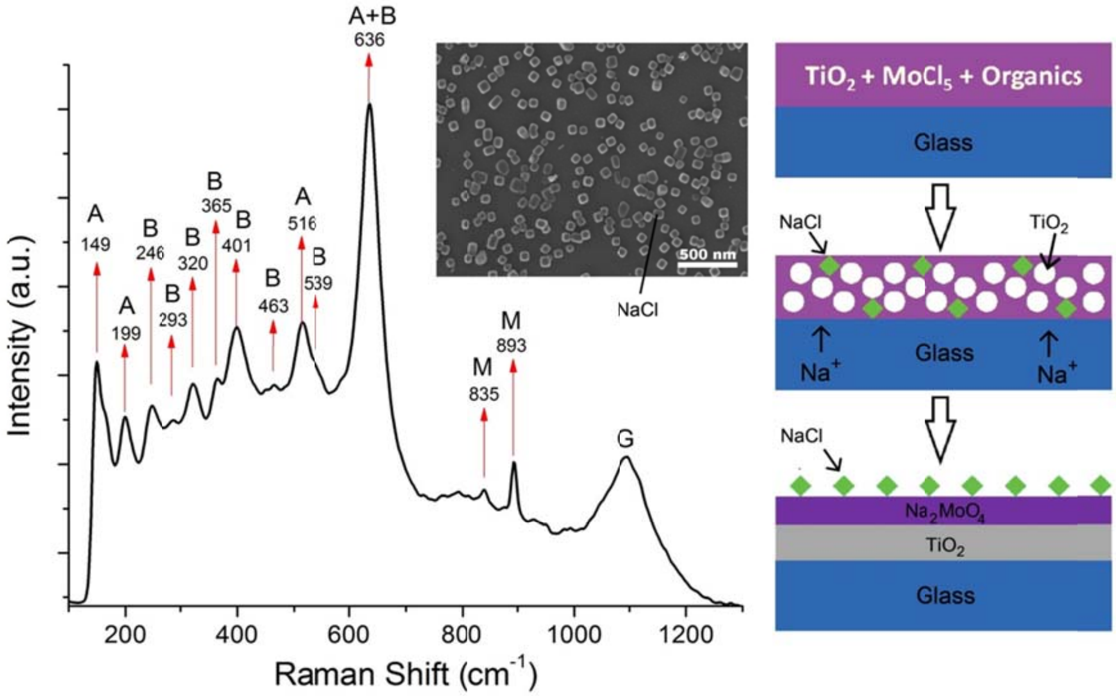

Figure 3-35: Raman spectrum of the 5% Mo-doped TiO_2 film. Surface of the film as pictured by SEM is shown in the inset. Proposed mechanism of the process is shown on the right. A: anatase, B: brookite, M: sodium molybdate, G: glass.

This reaction prevents sodium-titanium interactions. Formation of sodium chloride crystals was observed only on Mo- and to a limited extent on Ta-doped films but not on Co- and Ga-doped films.

Photocatalytic activity of the Mo-, Ag-, Ta-, and Ag-doped films with various dopant concentrations are shown in Figure 3-36. Overall, all dopant are beneficial in the low dopant concentration range (< 1%) and detrimental with increasing dopant concentrations.

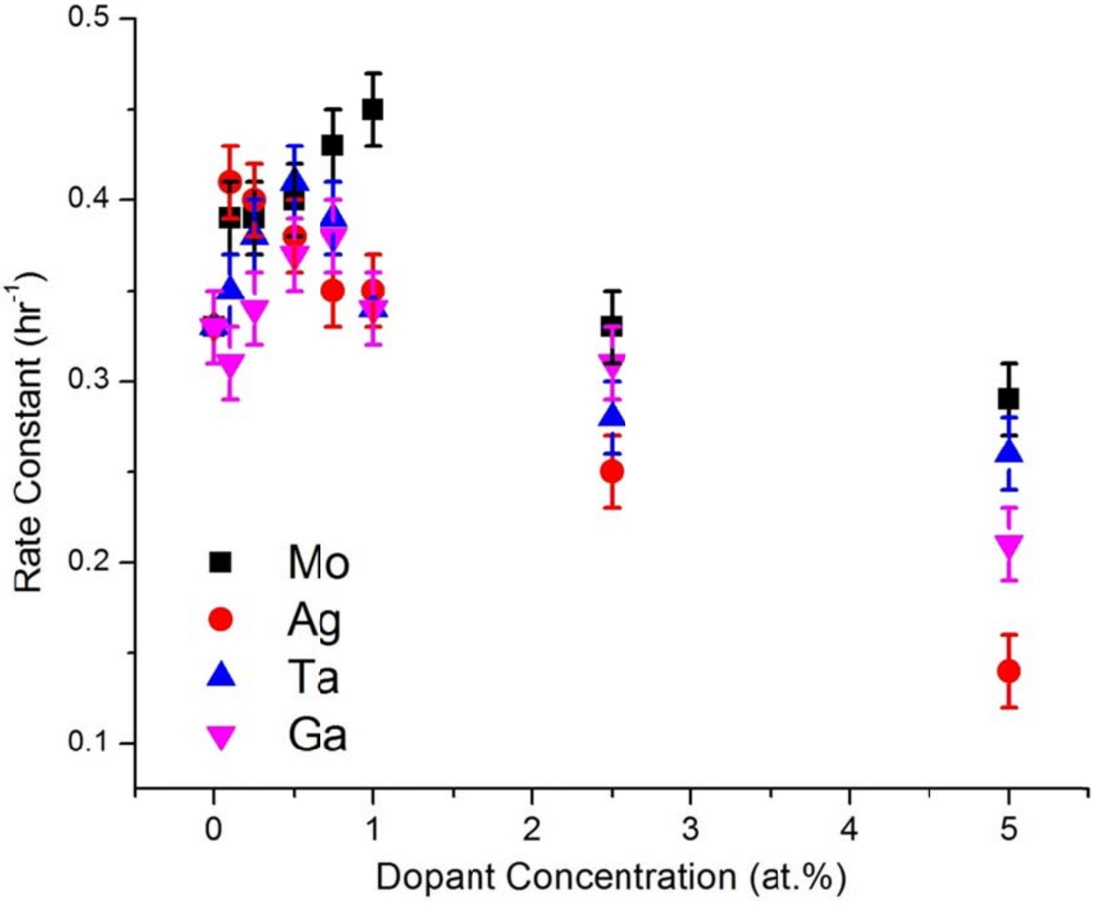

Figure 3-36: Photocatalytic activity of metal-doped films with various metal dopant concentrations.

Nanoindentation hardness values of metal-doped films are shown in Figure 3-37. Gallium doped films show almost 25% increase in the hardness whereas the effect is small cobalt and copper doped films. A slight decrease in the hardness of the molybdenum and tantalum doped films was detected compared to undoped films. Silver doping was found to cause a substantial decrease in the nanoindentation hardness of the films.

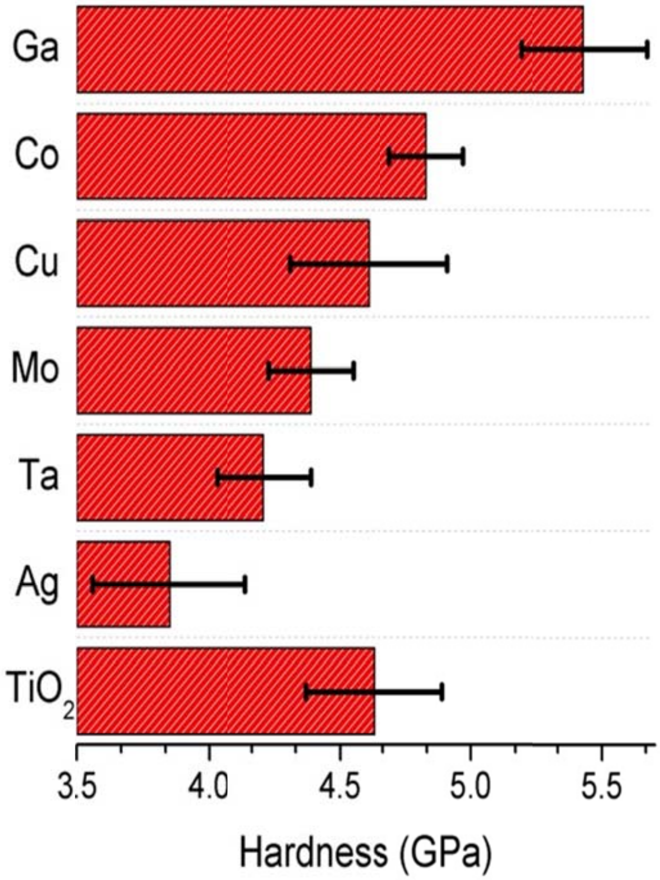

Figure 3-37: Nanoindentation hardness values of the metal doped films. Undoped film's value is given for comparison.

3.4.4. Conclusions

The effects of silver, cobalt, copper, gallium, molybdenum, and tantalum doping on the prevention of sodium poisoning of sol-gel titanium dioxide films by comparing the photocatalytic activities on glass and SiO_2 pre-coated glass. While sodium poisoning degraded the photocatalytic activity of undoped titanium dioxide films by 70%, it was only 10% for Mo- and Ta-doped titanium dioxide films. Molybdenum was superior to other dopants in terms of photocatalytic activity, both in the presence of sodium and in a sodium-free environment.

An optimum concentration was found for the majority of the metal dopants, which is between 0.1% at. and 1.0% at. Gallium doped films showed significant improvement in the mechanical properties compared to undoped films.

3.5. Nitrogen Doped Titanium Dioxide Films

3.5.1. Introduction

Nitrogen-doped titanium dioxide films are known to possess some visible light activity whereas the effects of nitrogen concentration on a variety of properties of titanium dioxide are not clear. A set of nitrogen doped titanium dioxide films with different nitrogen concentrations were investigated in terms of their optical absorption behavior, photocatalytic activity (UV and visible) and mechanical properties.

3.5.2. Experimental

Nitrogen-doped films were prepared by dip-coating (MTI Dip Coater HL-01); for this purpose, silica substrates were dipped into the prepared solution and withdrawn at a constant speed of 100mm/min. The humidity was varied between 20% and 30% during coating. Following the coating procedure, samples were taken to a tube furnace for calcination at 650°C for 1 hour in air followed by calcination at the same temperature under ammonia flow for various amounts of time.

3.5.3. Results and Discussion

Figure 3-38 shows the optical spectra of the films calcined at 650°C for 1 hour in air followed by calcination at the same temperature under ammonia flow for various amounts of time (30 min – 4 hr). According to the XPS measurements, nitrogen concentration was found to be around 10% for film calcined under ammonia for 4 hours. Nitrogen concentration has a direct effect on the optical absorption behavior of titanium dioxide films where increasing amount of red-shift in the absorption spectra is observed at increasing nitrogen concentrations. It is also important to note that despite the increased absorption of nitrogen-doped films in the visible light region, there is no significant change in the position of absorption edge which can be explained by formation of intra-band gap defects instead of a major band gap change. This was predicted theoretically.

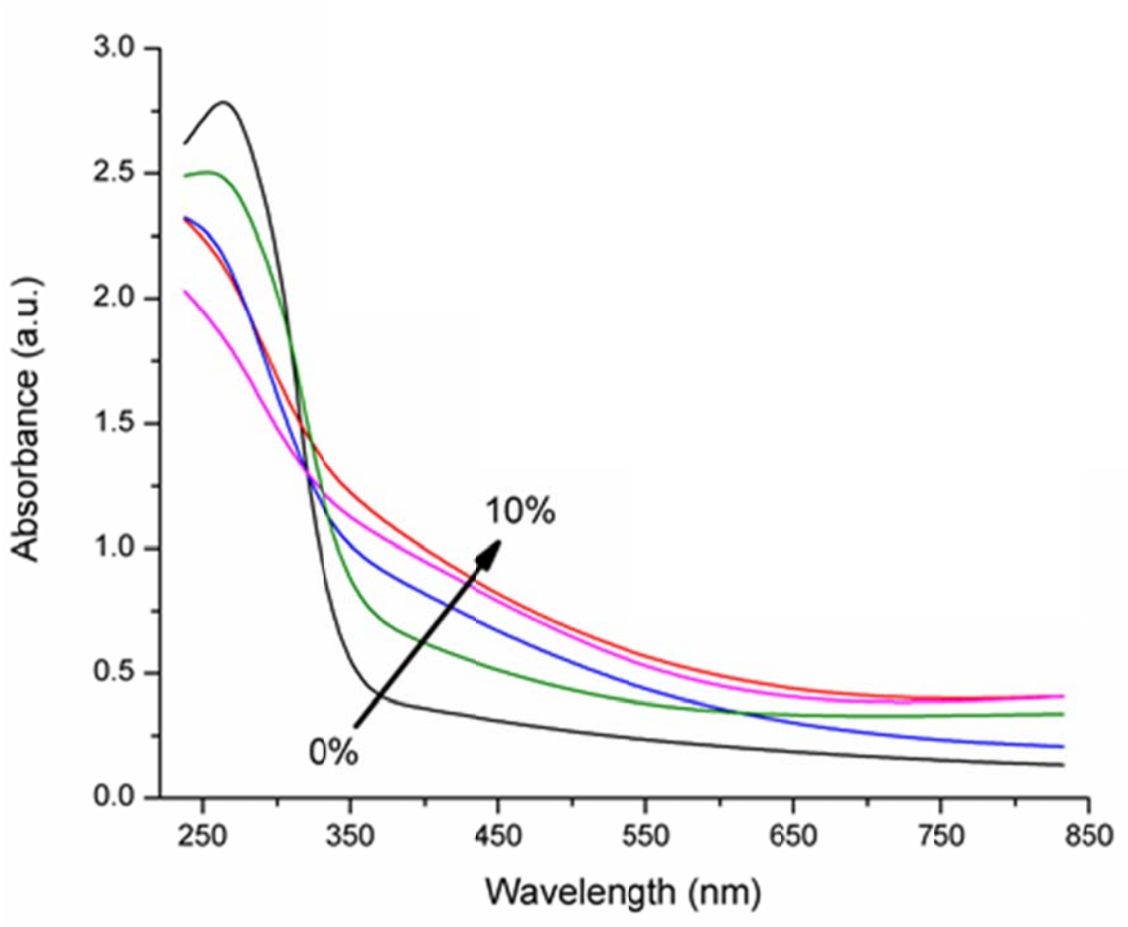

Figure 3-38: Optical absorption spectra of N-doped films with increasing nitrogen concentration.

.

Photocatalytic activity of the films with different nitrogen concentrations under UV and visible light irradiation are shown in Figure 3-39. It can be seen that nitrogen doping creates some visible light activity which increases up to a certain concentration after which it starts dropping. On the other hand, UV-light photocatalytic activity of titanium dioxide films is degraded with increasing nitrogen concentration. Thus, visible light photocatalytic activity comes at the expense of UV-light activity, which can be attributed to the increasing amount of recombination centers created in the titanium dioxide films due to nitrogen doping.

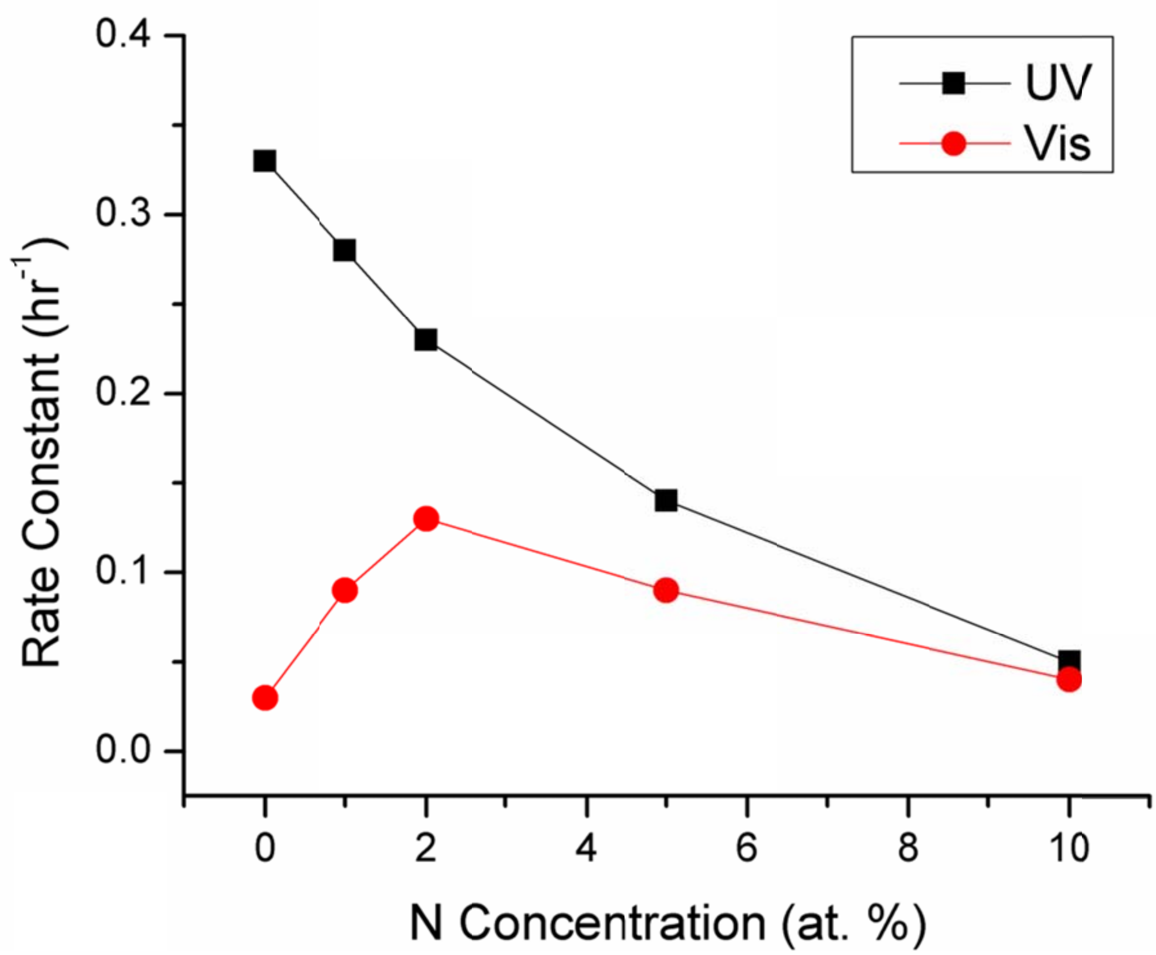

Figure 3-39: Photocatalytic rate constant vs. nitrogen dopant concentration under UV and visible light.

Titanium nitride is one of the hardest materials with a wide range of use in several applications. Thus, the mechanical properties of nitrogen-doped titanium dioxide films may be superior to those of undoped ones. Figure 3-40 shows the nanoindentation results of nitrogen-doped titanium dioxide films with various nitrogen concentrations. In contrast to expectations, nitrogen doping did not create a harder film but a lowered hardness was obtained till a certain amount of nitrogen concentrations and it increased back to the original value at 10% nitrogen. It is possible that hardness may gradually increase above this concentration to the value of pure titanium nitride whereas no photocatalytic activity was expected within this range. Thus, in a typical nitrogen-doped titanium dioxide film, hardness is expected to be somewhat lower than the undoped films in which the amount is depending on the concentration of nitrogen.

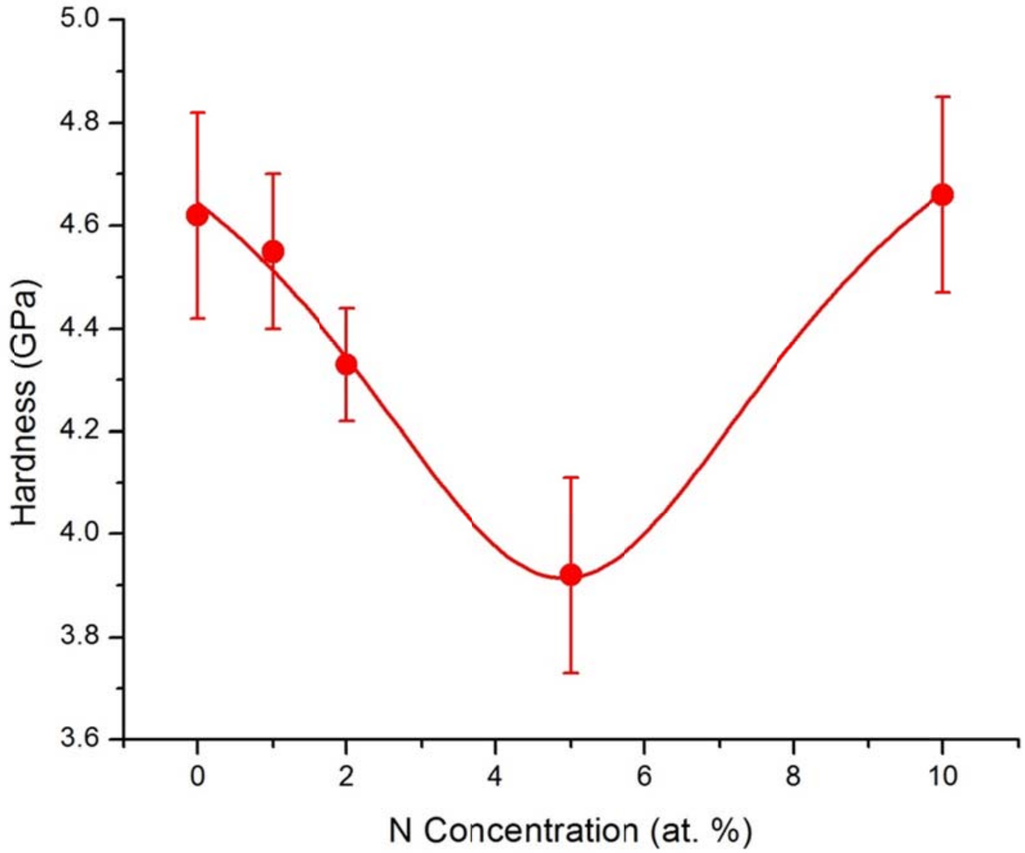

Figure 3-40: Nanoindentation hardness of titanium dioxide films vs. nitrogen dopant concentration.

3.5.4. Conclusions

Nitrogen-doped titanium dioxide films were studied for visible-light photocatalytic activity as these films absorb part of the visible spectrum. Although certain amount of visible light activity was observed with nitrogen doping, this effect was not directly proportional to the optical absorption. Visible light activity was optimum at a certain nitrogen concentration above which this positive effect diminished. On the other hand, visible light activity came at the cost of UV-light activity and this behavior was amplified with increasing nitrogen concentrations. Mechanical properties of nitrogen doped films were, overall, inferior to undoped titanium dioxide films; which was surprising since titanium nitride is an extremely hard material. The beneficial effect of nitrogen doping was only seen at relatively higher nitrogen doping concentrations which was detrimental to both visible and UV light activity.

3.6. Metal-Nitrogen Doped Titanium Dioxide Films

3.6.1. Introduction

Metal-nitrogen co-doping is investigated with various metal-nitrogen combinations while the concentration of the metal was kept at 5 at.% and nitrogen concentration was estimated to be around 10 at.%. Vanadium and chromium co-dopants were investigated in detail.

3.6.2 Experimental

Metal-nitrogen-doped films were prepared by dip-coating (MTI Dip Coater HL-01); for this purpose, silica substrates were dipped into the prepared metal-doped titanium dioxide solution and withdrawn at a constant speed of 100mm/min. The humidity was varied between 20% and 30% during coating. Following the coating procedure, samples were taken to a tube furnace for calcination at 650°C for 1 hour in air followed by calcination at the same temperature under ammonia flow for 4 hr.

3.6.3. Results and Discussion

Figure 3-41 shows the photocatalytic activity of metal-nitrogen doped titanium dioxide films under ultraviolet irradiation. Compared to undoped titanium dioxide, nitrogen doping alone was detrimental to the UV-light photocatalytic activity whereas only slight recovery of the lost activity was possible with metal co-doping except the Cr-doped film, which was investigated in detail to understand the observed phenomenon. Overall; co-doping with cobalt, copper, manganese and yttrium are found to be detrimental, silver, iron and nickel have no effect, tantalum, bismuth gallium, tungsten, molybdenum, niobium, vanadium and chromium are beneficial for UV-light photocatalytic activity compared to nitrogen doped films.

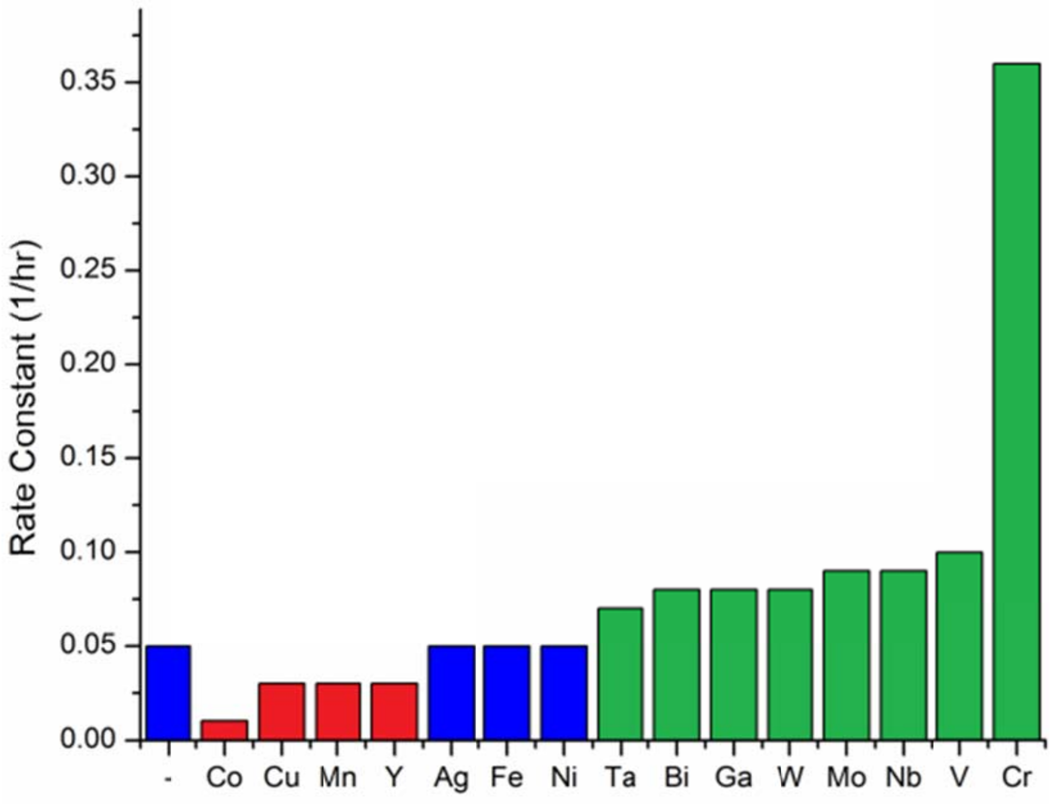

Figure 3-41: Photocatalytic rate constants of metal-nitrogen doped titanium dioxide films with different metal co-dopants under ultraviolet light.

Visible-light photocatalytic activities of the films (Figure 3-42) are significantly lower compared to the UV-light activity, as expected. In this case, co-doping with cobalt, copper, silver and yttrium have detrimental effects, chromium and iron have no significant effect, niobium, bismuth, nickel, tungsten, gallium, molybdenum, vanadium and tantalum have beneficial effects on the visible light photocatalytic activity.

Comparing the UV- and visible-light photocatalytic activities, it can be deduced that tantalum, vanadium, molybdenum and chromium are beneficial in the overall performance of titanium dioxide films. In particular, chromium is very beneficial in that it gives the very same photocatalytic activity with nitrogen-doped titanium dioxide under visible light whereas it performs seven times better under UV light.

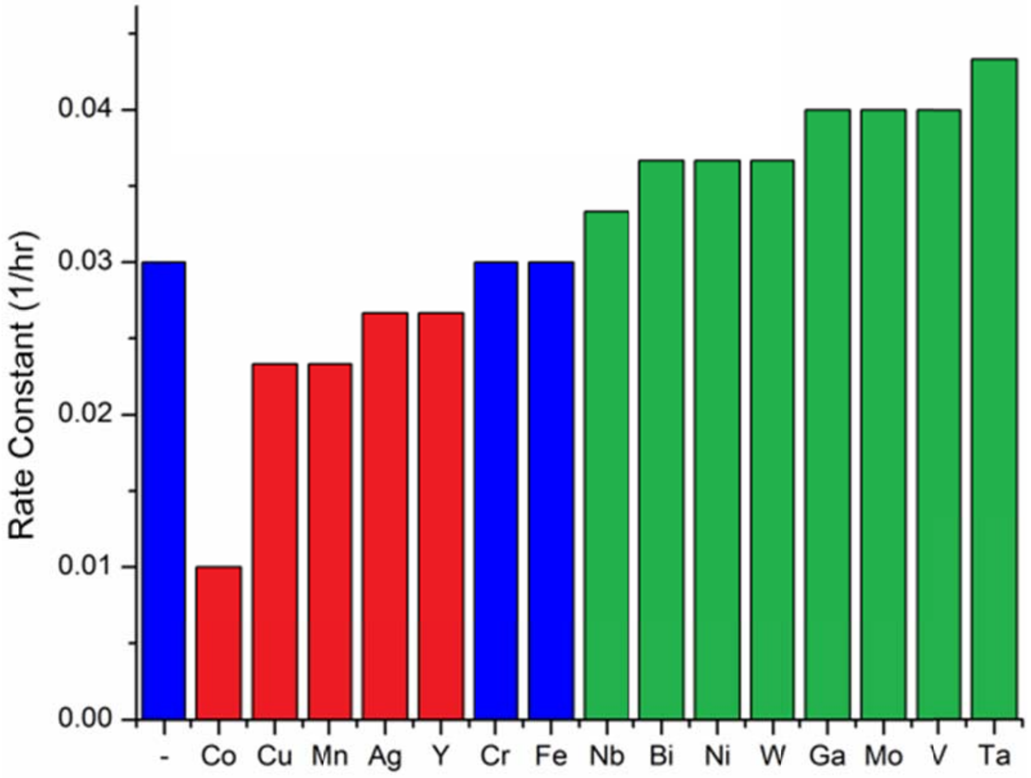

Figure 3-42: Photocatalytic rate constants of metal-nitrogen doped titanium dioxide films with different metal co-dopants under visible light.

Mechanical properties (nanoindentation hardness) of metal-nitrogen doped films with different metal co-dopants are shown in Figure 3-43. Compared to nitrogen-doped films (no metal co-dopants), copper, nickel, manganese and gallium are found to be detrimental to the overall hardness of the films whereas cobalt, vanadium, iron, tantalum, chromium, yttrium, molybdenum, tungsten and niobium are beneficial. Silver and bismuth co-dopants have negligible effect on the film hardness.

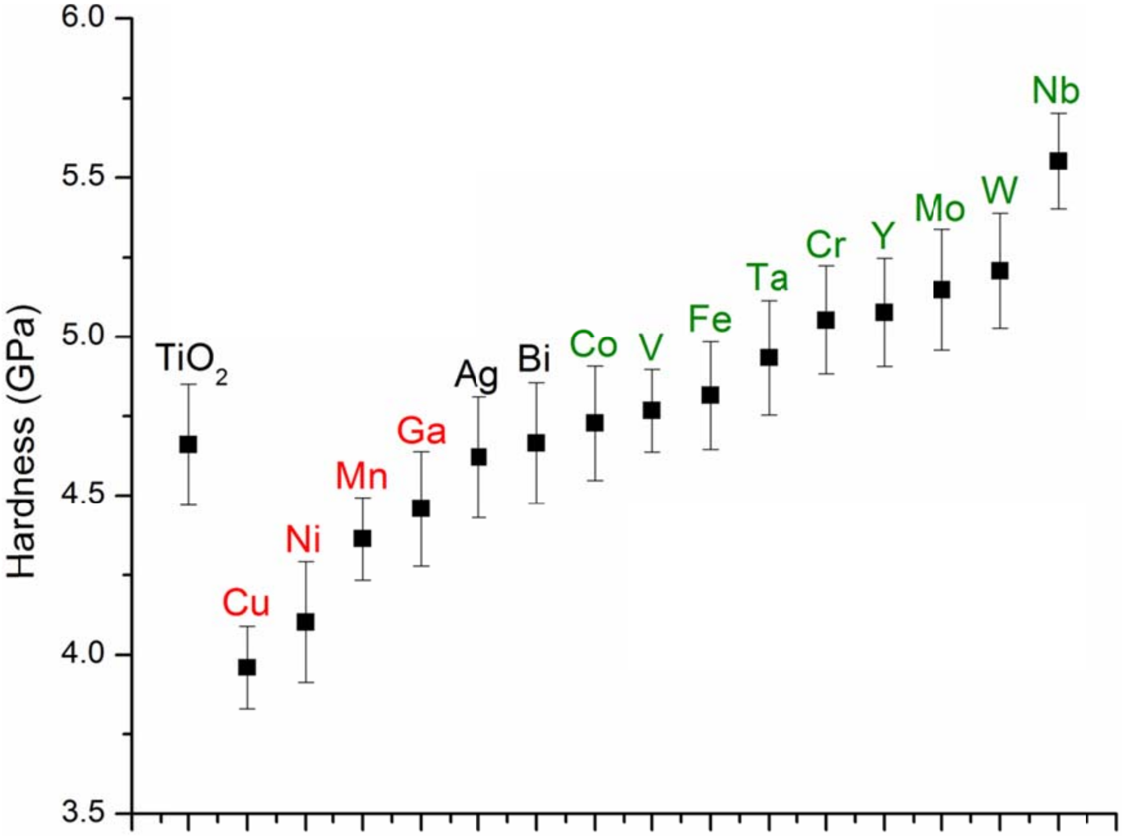

Figure 3-43: Nanoindentation hardness of the metal-nitrogen doped films. Nitrogen-doped film (no metal co-dopant) is given for comparison.

3.6.3.1. Cr-N-doped Titanium Dioxide Films

All films were determined to be anatase by x-ray diffraction (XRD) analysis. There was no significant change in the XRD spectra of ammonia-annealed films, though some slight decrease in the intensity of anatase peaks was observed. Film composition was calculated from x-ray photoelectron spectroscopy (XPS) analysis, and the resulting stoichiometry of the films was found to be $Ti_{1-x}Cr_xO_{2-y}N_y$ ($0.04 < x < 0.06$, $0.25 < y < 0.30$).

Photocatalytic activity of the prepared films under visible and UV light is shown in Figure 3-44. The activity under visible light was, as expected, lower than under ultraviolet light. Neither undoped nor Cr-doped TiO_2 films were active under visible light. N- and Cr-N-doped films were active in the visible light and performed similarly under visible light. In the UV-light range, however, Cr-N-doped films were significantly more active compared to the N- or Cr-doped films. The UV light activity of the Cr-N-doped films was similar to that of the undoped films.

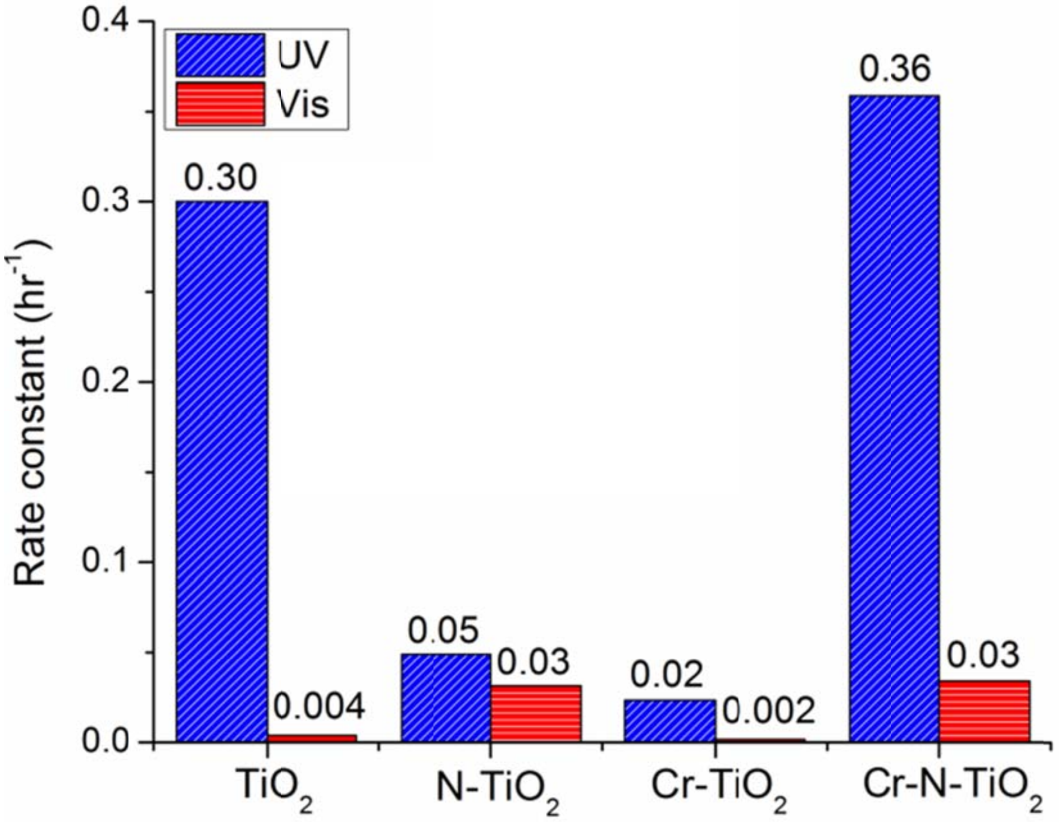

Figure 3-44: Photocatalytic rate constants (methylene blue decomposition) of undoped, N-, Cr-, and Cr-N-doped films under UV and visible light. Individual rate constants are given on top of the respective bars.

The results of XPS analysis are shown in Figure 3-45. The positions of the Cr 2p spin-orbit components (Figure 3-45a) are in agreement with the previously reported values for Cr-doped anatase, which were assigned to trivalent chromium (Osterwalder, Droubay et al. 2005). There are two notable changes in the Cr-N-doped films with respect to the Cr doped TiO_2: (i) an relative increase in the intensity of the Cr $2p_{1/2}$ peak and (ii) an overall shift of the Cr 2p levels to lower binding energies. The shift to lower binding energies has been attributed to the formation of Cr-N-O bonds (Paulauskas, Brady et al. 2006). Cr $2p_{3/2}$ position (575.5 eV) is rather close to the one that corresponds to CrN (575.8) and less likely to belong to metallic Cr (574 eV) or Cr_2N (577.7 eV) (Aouadi, Schultze et al. 2001).. It is also interesting to note that the Cr 2p levels shift to lower binding energies rather than forming a shoulder, which indicates the dramatic effect of the nitridation process on the Cr species. The shift to lower energy can be attributed to increased covalent character of the bond, which will be discussed later. The N 1s peaks (Figure 3-45b) are quite similar for both N-TiO_2 (396.0 eV) and Cr-N-TiO_2 (395.9 eV), and are assigned to substitutional nitrogen (Di Valentin, Pacchioni et al. 2005). Ti $2p_{3/2}$ peak (Figure 2c) at 458.7 eV in TiO_2 and Cr-doped TiO_2 was assigned to the Ti^{4+} state. The peak is broader in Cr-doped TiO_2 than in undoped TiO_2, with a relative increase in the intensity of its shakeup satellite at 464.5 eV. There is a second level in nitrided films at 457.1 eV, which is assigned to a lower oxidation state of Ti (i.e. Ti^{3+}). In the Cr-N-TiO_2 film, this level is lower in intensity indicating a lower concentration of Ti^{3+}, which is due to the strong coupling of Cr and N, as will be shown later. XPS valence bands (Figure 3-45d) gave evidence of a widening valence band with Cr-doping with respect to anatase film. Cr-N-co-doped film has an even wider valence band indicating a further decrease in the band gap (assuming similar conduction band positions).

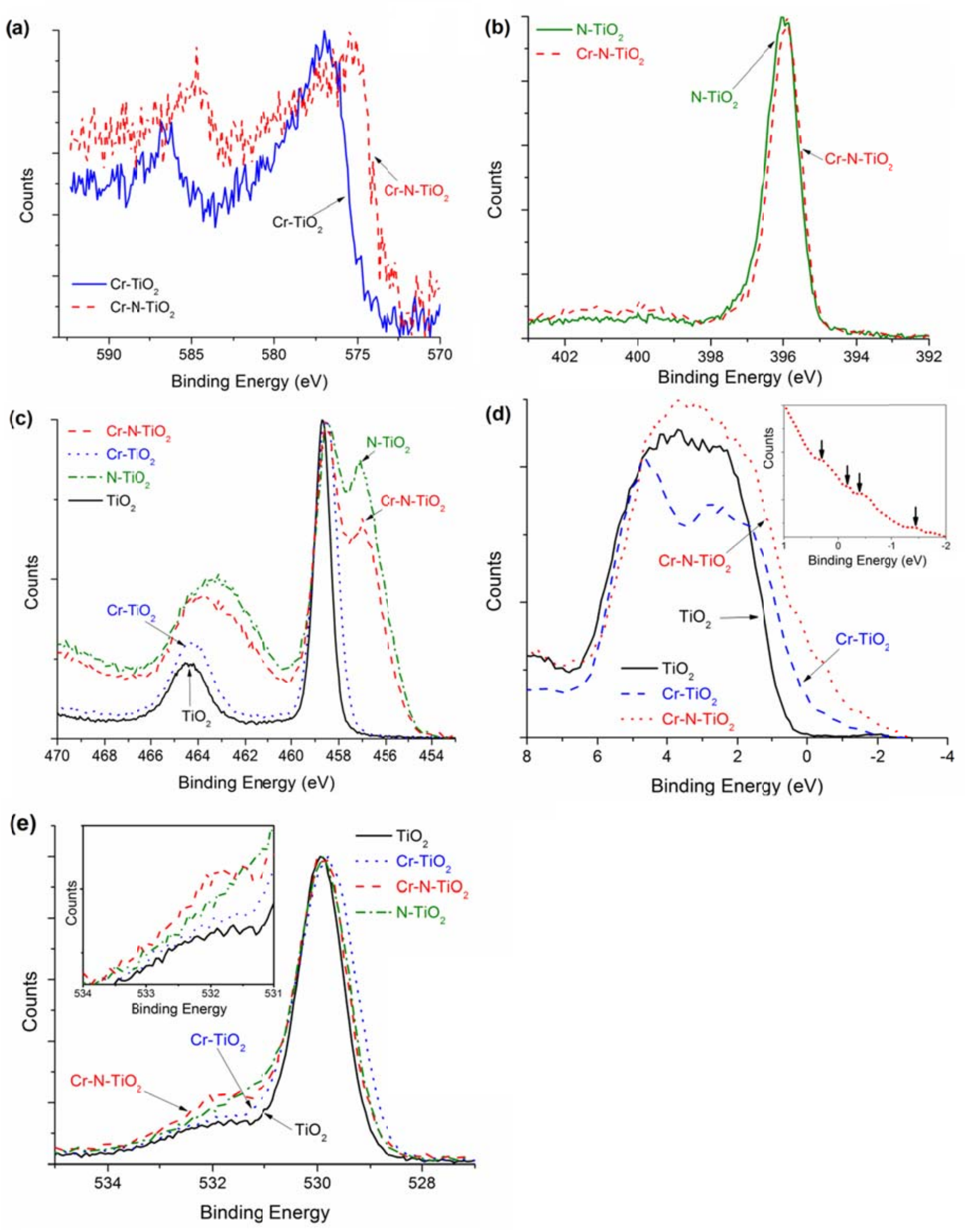

Figure 3-45: XPS spectra of the films around (a) Cr 2p, (b) N 1s, (c) Ti 2p, (d) valence band (inset: Cr-N-TiO$_2$ closer view) , and (e) O 1s.

3.6.3.1.1. Cr-Doped TiO_2: Non-compensated Case

In order to determine the global ground state, calculations were carried out with three different initial spins of Cr: non-spin (0), low spin (+1) and high spin (+3). The ferromagnetic low spin state with a total spin magnetic moment of 2 µb was found to be the global minimum, in agreement with the findings of Ye et al (Ye and Freeman 2006).

Formation energy of the Cr-doping is calculated here by assuming the reaction

$$TiO_2 + xCr = Ti_{1-x}Cr_xO_2 + xTi \quad (1)$$

for which the formation energy is given as

$$\Omega = \mu_{Ti_{1-x}Cr_xO_2} + x\mu_{Ti} - \mu_{TiO_2} - x\mu_{Cr}$$

where μ_A is the chemical potential of A. In the Ti-rich limit, chemical potential of Ti is given as

$$\mu_{Ti} = \mu_{Ti(hcp)},$$

and for the O-rich limit

$$\mu_{Ti} = \mu_{TiO_2} - \mu_{O_2}.$$

For Cr, we assumed

$$\mu_{Cr} = \mu_{Cr(fcc)} \quad \text{(Ti-rich)}$$

$$\mu_{Cr} = \frac{1}{2}\mu_{Cr_2O_3} - \frac{3}{4}\mu_{O_2} \quad \text{(O-rich).}$$

Results of calculations are given in Table 3-11.

Table 3-11: DFT calculation summary of non-compensated Cr-doped TiO_2

	ΔH_f (eV)		Total Magnetic Moment (per Cr)	Cr Mulliken Charge
	Ti-rich	O-rich		
$Ti_{30}Cr_2O_{64}$	4.22	-0.62	2.0	+1.05

Cr substitution was found to be energetically more favorable in the O-rich state compared to the Ti-rich state. Although the values obtained are based on the thermodynamic assumption of zero Kelvin, thus neglecting any entropy contribution, the successful incorporation of dopants is determined primarily by their energies. In order to test the accuracy of our assumption, corresponding calculations were performed for TiO_2 anatase and results are given in Table 3-12. The predicted lattice parameters and the bulk modulus values were in excellent agreement with the experimental values, producing errors less than 1%. Formation energy was calculated to be 9.48 eV, in close agreement with the experimental value of 9.73 eV. It is important to point out the sensitivity to the choice of exchange functional.

Table 3-12: **Calculation results for TiO_2 anatase**

	a=b (Å)	c (Å)	Bulk Modulus (GPa)	ΔH_f (eV)
Calculated	3.776	9.563	179.6	9.48
Experimental	3.784	9.515	178	9.73
Error ±	0.21%	0.50%	0.90%	2.60%

A plot of the electronic density of states (DOS) for ferromagnetic Cr-doped TiO_2 is shown in Figure 3-46a. There is a significant crystal field splitting of non-degenerate Cr t_{2g} and Cr e_g states. The Fermi level lies just above the valence band, which is formed principally from O 2p and Cr t_{2g} states. Calculations utilizing hybrid functionals such as B3LYP by Di Valentin et al. have indeed confirmed the splitting of t_{2g} and e_g states in Cr-doped TiO_2 (Valentin, Pacchioni et al. 2009).

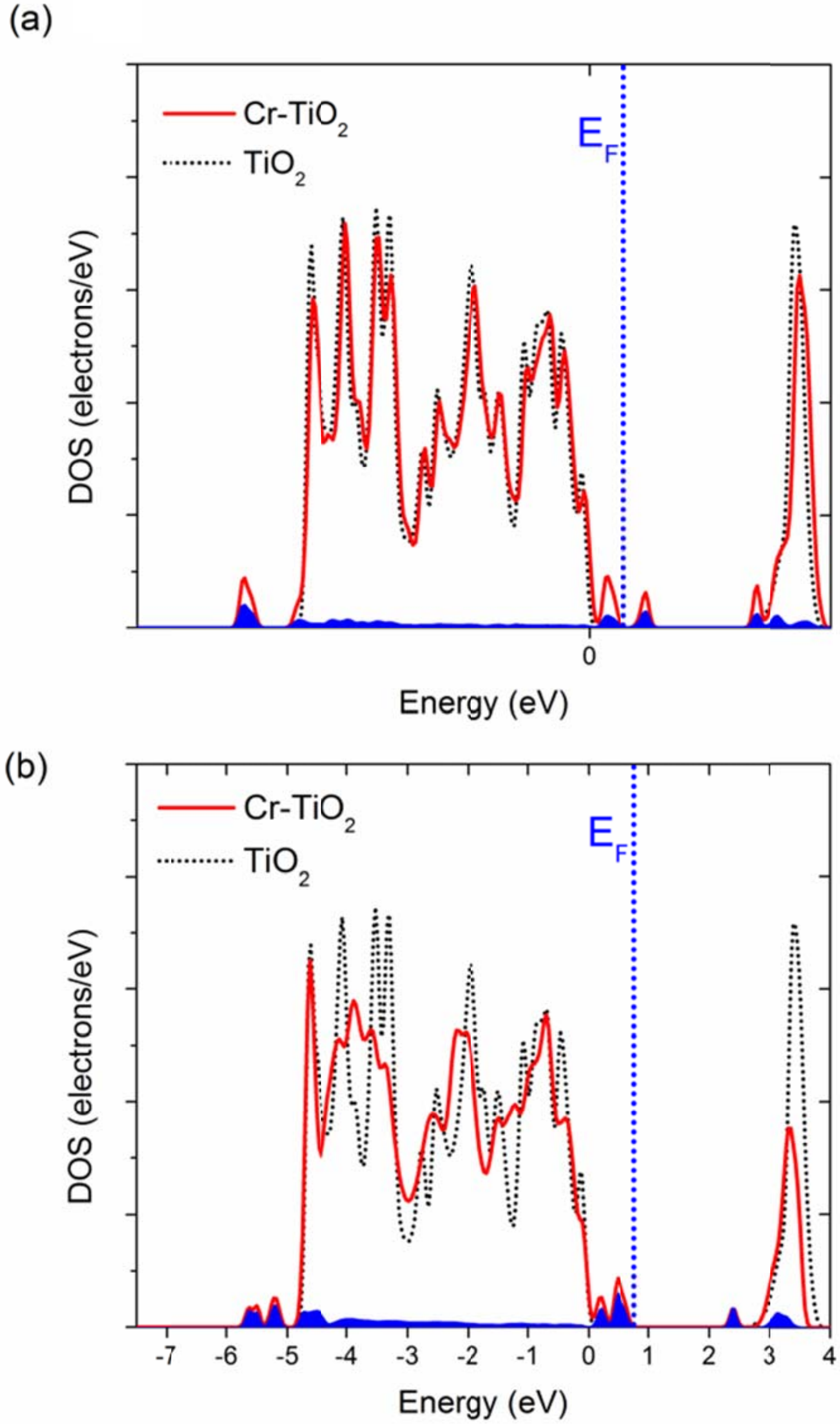

Figure 3-46: DOS plots of Cr-doped TiO$_2$ in the (a) uncompensated and (b) compensated state. DOS plot of undoped anatase is given as the dotted line. Partial DOS arising from Cr d orbitals are shown as filled plots.

According to Mulliken analysis, Ti and Cr have charges of +1.33 and +1.05, respectively. In reality, Cr is expected to have the same nominal charge state with Ti in non-compensated doping. Although the trivalent state is more likely to occur in TiO_2, both Cr^{4+} and Cr^{3+} have previously been observed in Cr-doped anatase by XANES spectra (Pan and Wu 2006). Cr^{6+} is omitted in this study as an interstitial position is likely for the small hexavalent ion, which significantly disrupts the charge balance and requires a very large supercell with Ti vacancies for charge compensation.

3.6.3.1.2. Cr-Doped TiO_2: Compensated Case

Ideally, for every two Cr^{3+} substitutions in TiO_2, one compensating oxygen vacancy has to be created to preserve the balance of valence (another possibility is the creation of interstitial Ti, which is unlikely due to the highly charged state of the defect). Preserving the charge balance by defects is particularly true for acceptor doped TiO_2 as its valence band may not be receptive to holes to preserve the charge balance (Smyth 2000). For the calculations, a (3 x 3 x 1) supercell with 106 atoms was utilized and two Cr atoms and one oxygen vacancy were introduced. The Cr atoms were initially placed far from each other. The initial position of the oxygen vacancy was varied and each constructed starting structure was subjected to coarse geometry optimization with different initial spins until the global ground state was found. The minimum energy structure was then geometry optimized with a finer accuracy. The global ground state was found to be ferromagnetic with a total magnetic moment of 3 μb per Cr atom. The predicted increase in the magnetic moment upon the introduction of an oxygen vacancy is in agreement with the reported experimental observations (Xiao and et al. 2008). The computed DOS plot is shown in Figure 3-46b. The Cr 3d states were found to be split, similar to the uncompensated case. On the other hand, defect levels are shallower in the compensated case and Fermi level was found to be just above the levels associated with the valence band. Extension of the valence band with neighboring levels just above the original valence band resembles the case of N-doped TiO_2,(Asahi, Morikawa et al. 2001) whereas Cr-doped TiO_2 lacks the visible light photocatalytic activity present in to N-doped TiO_2.

Optical calculations were carried out on both compensated ($Ti_{14}Cr_2O_{31}$) and uncompensated ($Ti_{15}CrO_{32}$) cases and the results were compared to experimental findings. In Figure 3-47, optical absorbance spectra of the anatase and 5% chromium doped anatase along with the calculated absorbance of compensated and uncompensated Cr-doped anatase (6.3% and 5.6% Cr, respectively) are shown. Experimental evidence suggests a small shift of the absorption edge with formation of a strong tail between 350 nm and 550 nm. Although both cases predict the tail, the uncompensated state fails to reproduce the shift in the main absorption edge while compensated state reproduces the experimental findings. This behavior can be clearly seen from the plot in Figure 3-47c, which shows “difference spectra” calculated by subtracting the absorbance of undoped TiO_2 from that of the doped materials.

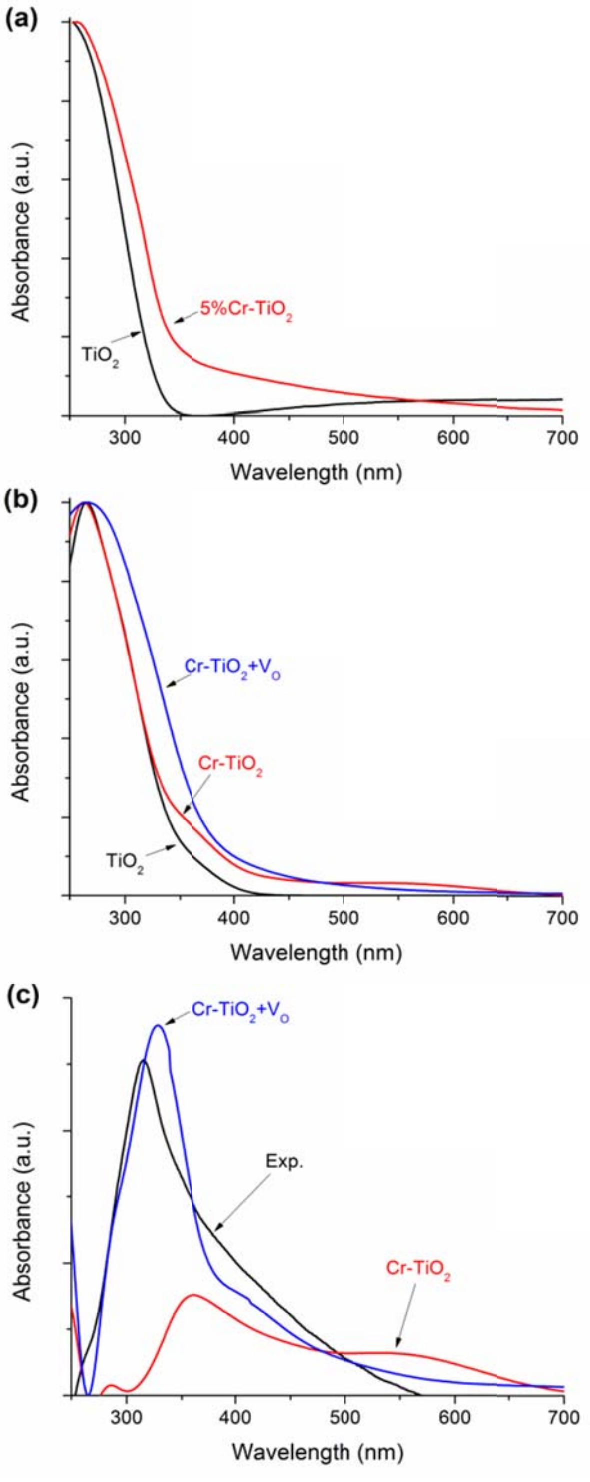

Figure 3-47: (a) Experimental and (b) calculated optical spectra of (compensated and uncompensated) Cr-doped TiO$_2$. (c) Optical "difference" spectra, where undoped TiO$_2$ spectrum was subtracted from Cr-doped TiO$_2$ spectrum. Individual spectra were normalized to their respective peak positions before further processing.

3.6.3.1.3. Cr-N-Doped TiO_2

Modeling of Cr-N-doping is much more difficult compared to Cr-doping alone as the former requires testing of a combination of initial geometries, especially when an oxygen vacancy is involved. In order to minimize the computational cost, we used the following scheme. First, the optimized geometry of uncompensated Cr-doped TiO_2 ($Ti_{15}CrO_{32}$) was taken and one oxygen atom from different positions were substituted with nitrogen. These initial positions were subjected to full geometry optimization and the one with the minimum energy was taken to be the ground state. Oxygen vacancies were modeled by removing an oxygen atom from a site close to and another far from the Cr-N defect center and comparing the energies of the optimized structures. The nitrogen positions inspected in detail are shown in Figure 3-48.

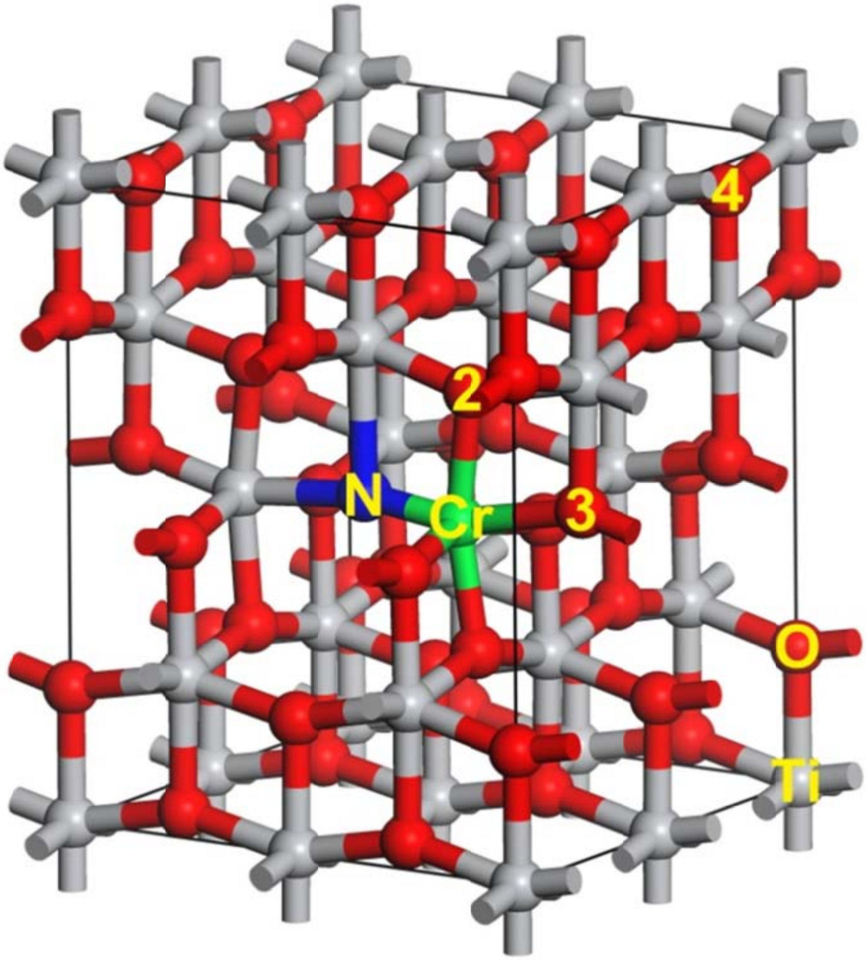

Figure 3-48: 2 x 2 x 1 anatase supercell for calculations. Additional nitrogen positions considered are numbered, i.e. P2, P3, and P4.

A substitutional nitrogen can occupy a position close to, or far away from, the Cr position depending on the chemical interaction between them. According to the calculations carried out by selecting various initial positions, nitrogen was found to prefer a position close to the substitutional Cr. An N atom occupying an oxygen site next to Cr was found to have an energy advantage of 1.39 eV relative to an N atom far away from the Cr. This is quite surprising as an electrostatic repulsion is expected between both negatively charged defect centers Cr_{Ti}^{-} and N_{O}^{-}. A possible explanation for this preference is when adjacent, these two dopants form a bond with covalent character. The present calculations indeed produced a very strong Cr-N bond in the TiO_2 lattice with a length of 1.601 Å compared to 2.051 Å for Ti-N bond. The Cr-N bond length in this case, is comparable to the Cr-N bond length in chromium nitride (1.589 Å). Long et al. have reported a Ti-N bond length of 2.026 and compared this result to W-N bond length of 1.851 in W/N co-doped TiO_2 and concluded that strong W-N bonds might be important for the high photocatalytic activity of W/N co-doped TiO_2. If this is the case, clearly, Cr-N bonds are much stronger compared to either Ti-N or W-N bonds. Mulliken analysis produced charges of +0.92, +1.32, -0.66, and -0.43 for Cr, Ti, O, and N, respectively. For N-doped TiO_2, N has a Mulliken charge of -0.58. Thus, Cr-N bond has a clearly more covalent character compared to Ti-N bonds.

It is interesting to note that even the second N atom preferentially occupies a position close to Cr with an energy advantage of 0.2 eV compared to a position far away from the Cr position (Figure 3-48). For the incorporation of the second nitrogen, three positions were considered: an asymmetric bonding to Cr (P2), symmetric bonding to Cr (P3), and a position far away from the Cr (P4). P2 was found to be the most stable position. Addition of third nitrogen to position P3 or P4 (Figure 3-48) produces similar results in terms of energy cost. Electronic structure calculations were performed only on the system with the third nitrogen atom substituted at position P3. A summary of the results is presented in Table 3-13.

DOS plots of Cr-N-doped TiO_2 with varying amounts of N and oxygen vacancies are shown in Figure 3-49. It can be deduced from the DOS plots that Cr defect positions depend strongly on the concentration of the dopants. Thus, it is possible to tailor, in theory, the band gap of Cr-N-doped TiO_2 by varying the Cr/N ratio.

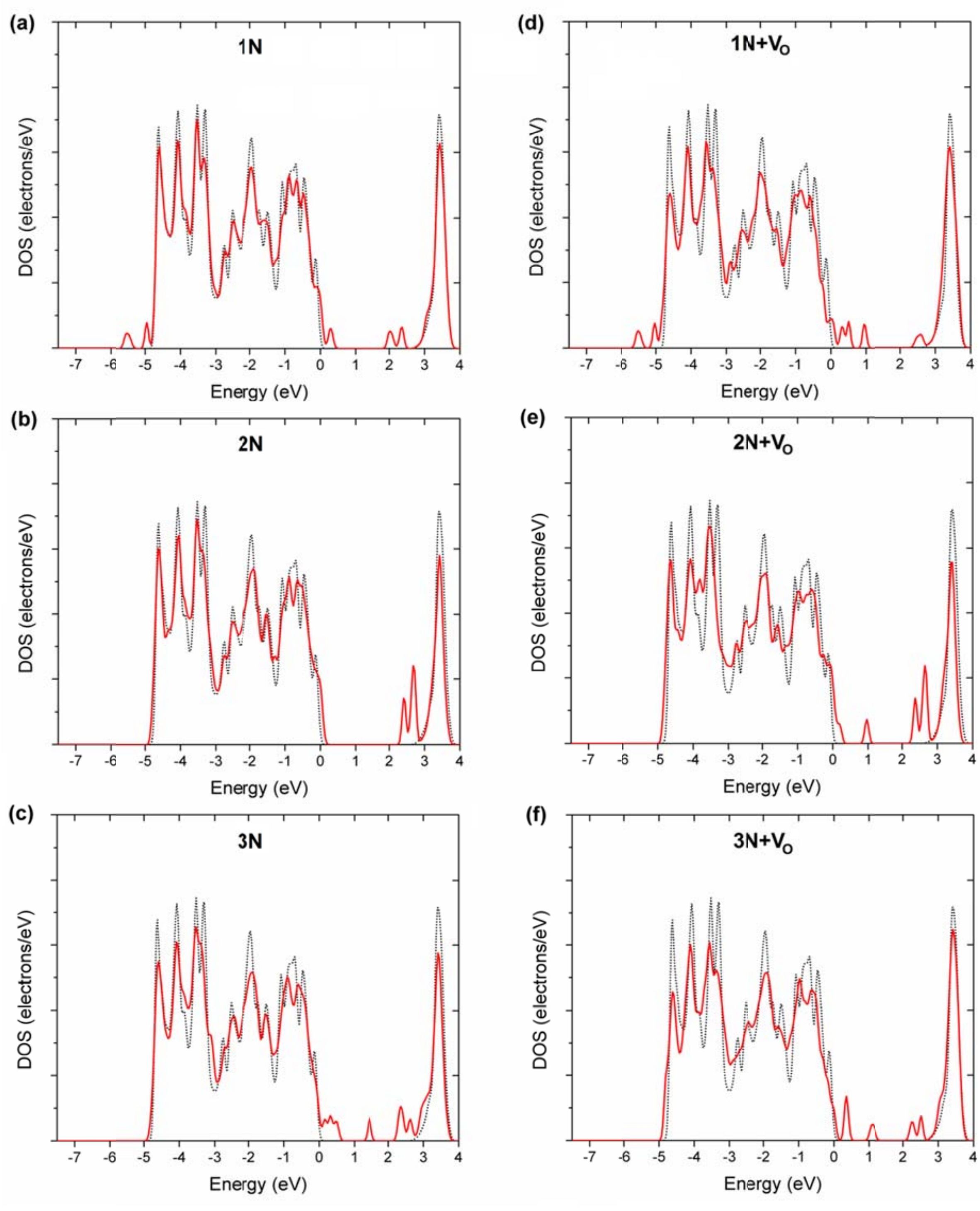

Figure 3-49: Calculated DOS plot of (a) $Ti_{15}CrO_{31}N$, (b) $Ti_{15}CrO_{30}N_2$, (c) $Ti_{15}CrO_{29}N_3$, (d) $Ti_{15}CrO_{30}N$, (e) $Ti_{15}CrO_{29}N_2$, and (f) $Ti_{15}CrO_{28}N_3$.

Plotted electron densities around Cr atom in Cr-doped and Cr-N-doped TiO_2 are shown in Figure 3-50. A highly localized electron density around Cr is obvious in all cases and this is particularly significant especially since DFT calculations tend to favor delocalization. Contrary to DOS plots, electron density plots give a clearer picture to explain the observed decrease in the photocatalytic activity of Cr-doped TiO_2. First, we have shown that Cr-doping leads to oxygen vacancies and according to the calculations conducted, this oxygen vacancy lies next to the Cr dopant. It should be noted at this point that a small amount of oxygen vacancies normally exist in TiO_2 which is responsible for its n-type behavior. Doping with Cr increases the concentration of the oxygen vacancies considerably, and this can be the reason for the lower photocatalytic activity of TiO_2. On the other hand, increased oxygen vacancies, in principle, should increase the photoconductivity of TiO_2 whereas the opposite was observed by Herrmann et al. (Herrmann, Disdier et al. 1984). This discrepancy can only be possible by the existence strong electron traps. A number of Ti^{3+} are ionized at room temperature to form excitons and the equilibrium state can be given as (Richter and Schmuttenmaer 2010)

$$[Ti^{4+}*/e^-] \leftrightarrow [e\text{-}][Ti^{4+}*],$$

where $Ti^{4+}*$ is the ionized state of Ti^{3+}. A similar equation can be given for Cr

$$[Cr^{4+}*/e^-] \leftrightarrow [e\text{-}][Cr^{4+}*],$$

However, as seen from the electron density plot, Cr bounds electrons more strongly compared to Ti, which will result in decreased electron mobility. It has recently been shown by time resolved microwave conductivity (TRMC) that Cr-doping causes a very rapid charge recombination in TiO_2 powders (Pichat, Enriquez et al. 2010). Cr can have multiple oxidation states in TiO_2 as evidenced by XANES, thus single Cr can act as electron trap for more than one electron. When Cr-doped TiO_2 is nitrided, a strong coupling of Cr and N occurs which prevents the extensive ionization of trivalent Cr due to the covalent-like character of the bonding between Cr and N.

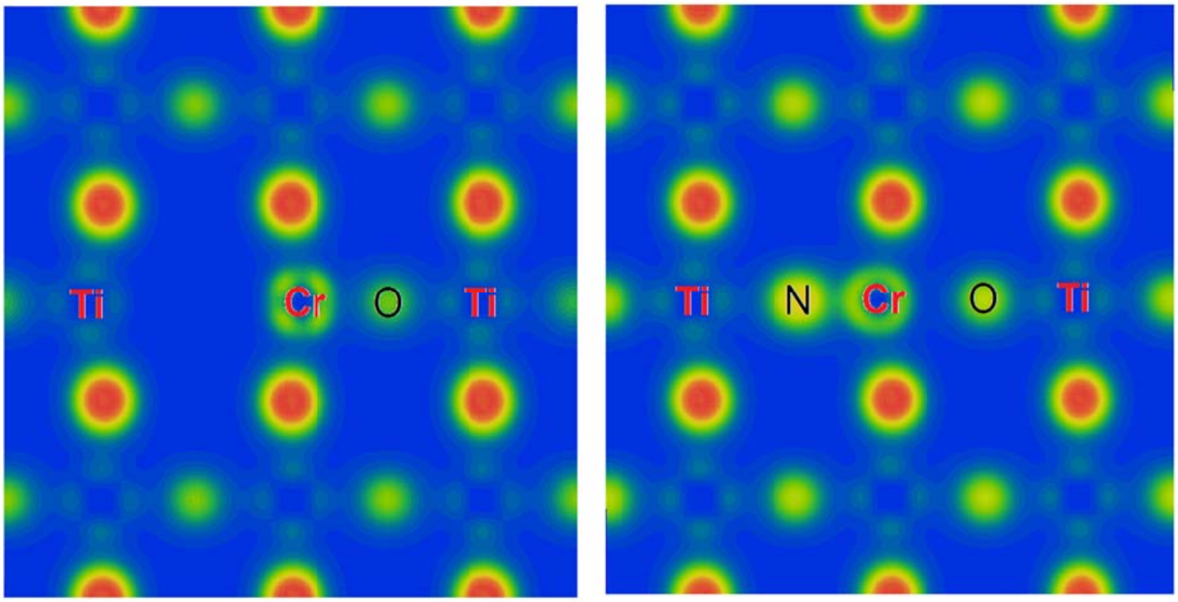

Figure 3-50: Calculated electron densities around Cr atoms in Cr-doped (left) and Cr-N-doped (right) TiO_2.

Following conclusions can be drawn based on the experimental findings and theoretical calculations: (i) N and Cr tend to couple in the TiO_2 lattice forming strong bonds with some covalent character, (ii) The tendency to coupling decreases with increasing N/Cr ratio, though the picture is not clear at high N concentrations, (iii) Cr-N doping creates new levels inside the band gap with a strong dependence on the Cr/N ratio, (iv) Cr-N coupling decreases the amount of trivalent titanium in N-doped TiO_2 which might be responsible for the increased photocatalytic activity. It has indeed, been shown by a recent study that Ti^{3+} states is responsible for exciton-like trap states which limits the electron mobility in TiO_2 nanotubes (Richter and Schmuttenmaer 2010).

Table 3-13: Summary of the calculation results of the Cr-N doped systems with varying amount of N and with/without oxygen vacancy.

System	Cr-N1 bond length (Å)	Cr-N2 bond length (Å)	Cr-N3 bond length (Å)	Cr Mulliken charge	Net spin of the system (µb per Cr)
1N	1.601	-	-	+0.86	1.0
1N+V_O	1.819	-	-	+0.89	3.0
2N	1.599	1.707	-	+0.69	0.0
2N+V_O	1.635	1.735	-		
3N	1.624	1.714	1.822	+0.66	1.0
3N+V_O	1.642	1.744	1.818	+0.66	1.0

3.6.3.2. V-N-doped Titanium dioxide

Titanium dioxide supported vanadia is an important heterogeneous catalyst commonly used for the selective oxidation of hydrocarbons, isopropanol decomposition, and selective reduction of nitric oxide with NH_3 (Bond and Tahir 1991). Hence, titania - vanadia system has been investigated by several authors. Stable polymorphs of titanium dioxide and VO_2 have the same rutile structure which allows them to form a solid solution in a wide compositional range. On the other hand, the Titanium dioxide (anatase) – V_xO_y system is still controversial. In a recent report, Habel at al. reported that there was no miscibility between anatase and vanadium oxide under oxidizing or reducing conditions (Habel, Goerke et al. 2008). Busca et al. have reported successful preparation of a solid solution of V in anatase by a co-precipitation process followed by calcination at 700°C (Busca, Tittarelli et al. 1987).

It is clear from the previous reports that a high calcination temperature (600°C <) is required to dissolve V in anatase. However, it is also required to prevent formation of rutile, and vanadium is known to accelerate this transition. This can be achieved by preparing TiO_2 as a film on an inert substrate (such as silica) rather than a powder since anatase-to-rutile transformation takes place at significantly higher temperatures in films compared to powders due to the spatial restrictions imposed by the substrate.

XRD results of the films calcined at 650°C in air are shown in Figure 3-51. All the films were composed of anatase and no other phase was detected. V-doping evidently increased the crystallinity of the samples whereas this effect was not linear with the V concentration. The strongest peak of anatase (101) showed a shift to higher angles with the incorporation of vanadium, which indicates a possible contraction of the lattice. After samples were further calcined at 650°C under NH_3, crystallinity of the V-doped samples increased in contrast to TiO_2 films, which became X-ray amorphous (Figure 3-51b). Gartner et al. have reported similar results in which a TiO_2 sample calcined at 600°C under NH_3 was amorphous although the one calcined at 500°C under same conditions was amorphous (Gartner, Osiceanu et al. 2008). They attributed this behavior to the ongoing re-crystallization of the sample induced by introduction of N atoms into the structure. On the other hand, amorphisation of TiO_2 is severely detrimental to the photocatalytic activity as fully amorphous TiO_2 has little or no photocatalytic activity. In this respect, V-doping is beneficial to preserve the crystallinity of the films.

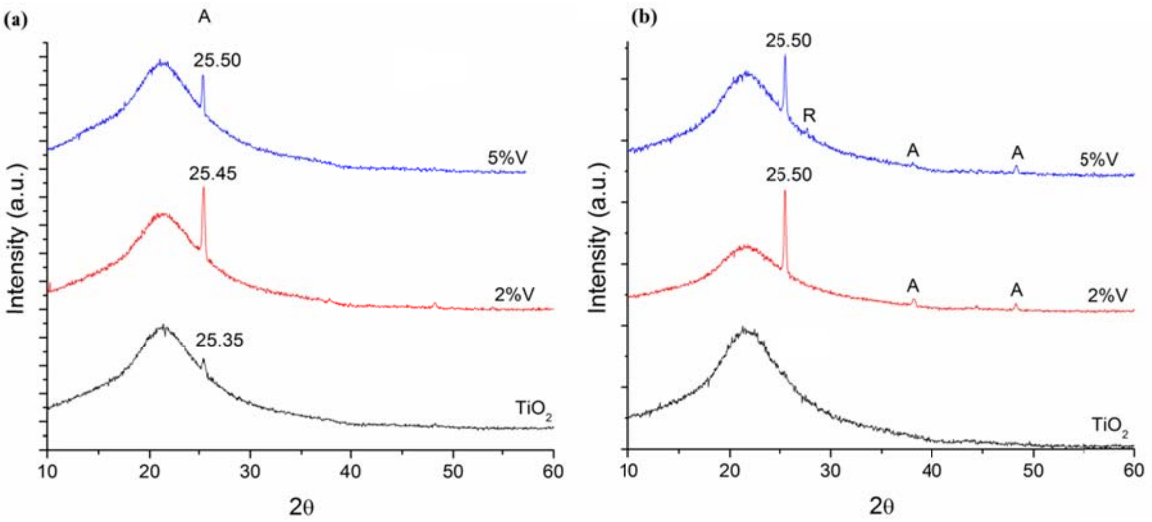

Figure 3-51: XRD pattern of samples (a) calcined at 650°C in air and (b) post-treated at 650°C under NH_3. A: anatase, R: rutile. Anatase (101) positions are shown above the respective peaks.

Optical spectra of the films are shown in Figure 3-52. Absorption edges of the V-doped films were significantly red-shifted compared to undoped films whereas absorption in the UV range was less. Further doping by N caused a slight blue-shift in the spectra of both 2% and 5% V-doped films. For undoped films, there is an increased absorption to the visible region with N-doping which is reported to be caused by formation of defect levels just above valence band of anatase.

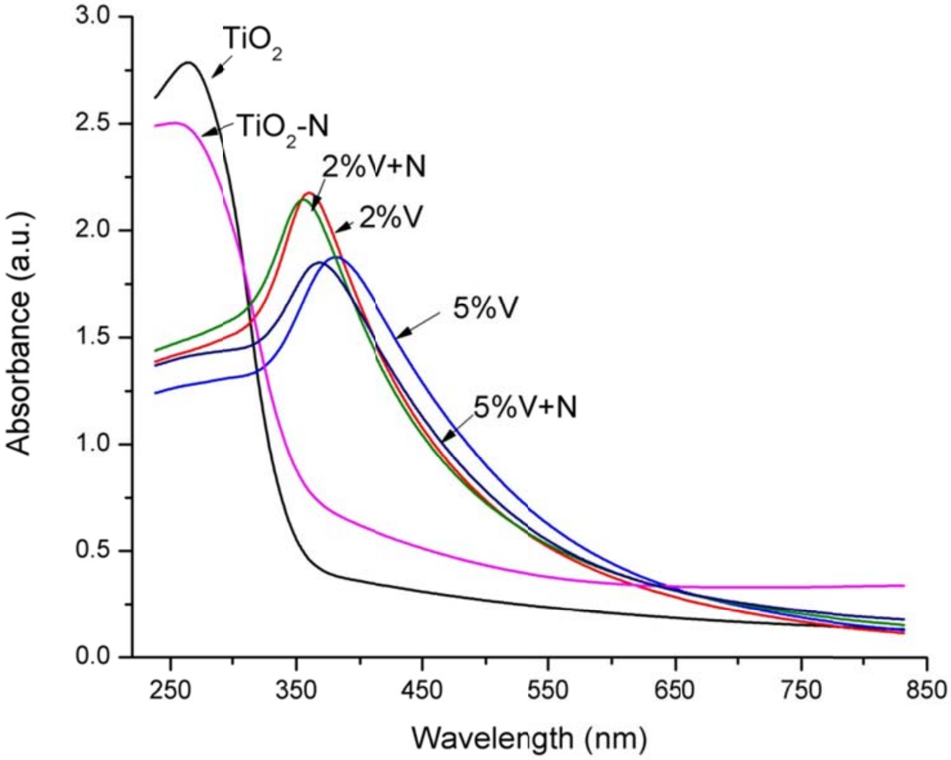

Figure 3-52: Optical spectra of the films calcined in air and air + NH_3.

Visible light photocatalytic activities of the films are shown in Figure 3-53. Slightly increased activities were observed with V-doped films, with increasing vanadium concentration. On the other hand, V-doped films were significantly more absorbing in the visible range, which apparently did not transform to a proportional increase in the visible light activity. This can be explained by the formation of deep level defects within the anatase band gap, which are possibly acting as recombination centers. On the other hand, V-N-co-doped films showed some improvement over N-doped films which indicates elimination of some of the recombination centers.

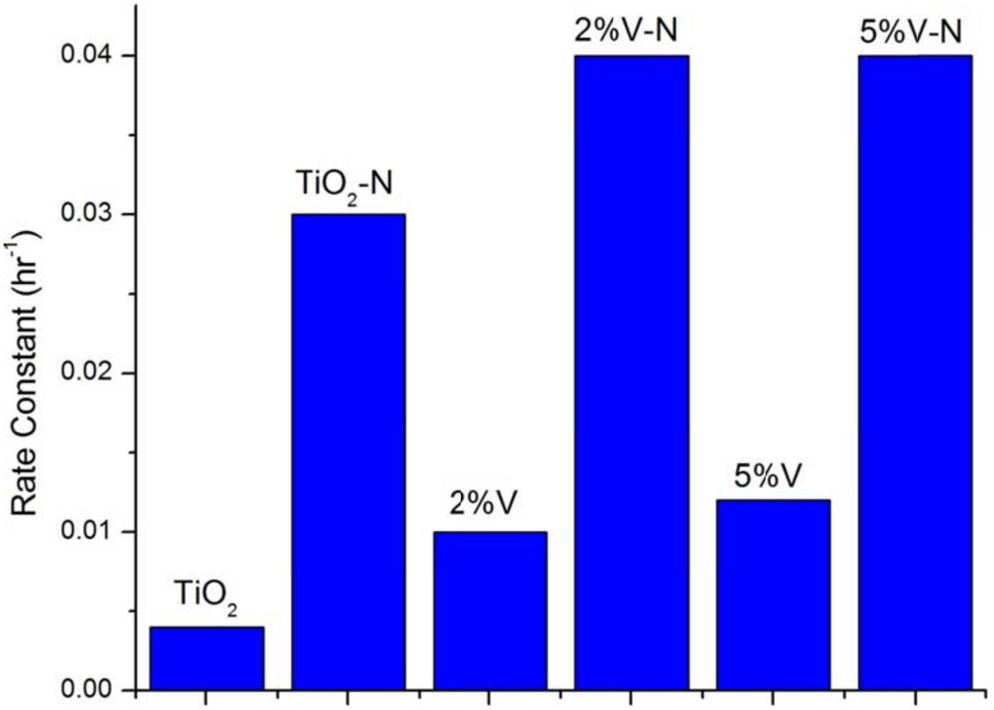

Figure 3-53: Visible-light photocatalytic activity of vanadium and vanadium-nitrogen co-doped films. Nitrogen concentration is estimated to be 10 at. % in all N-doped films. Photocatalytic activity of undoped and nitrogen-doped titanium dioxide films are given for comparison.

Photocatalytic activities of the films under UV light are shown in Figure 3-54. It can be seen that undoped films were almost three times more active as compared to the V-doped films. Dopant concentration has a minor effect as the minimum doping amount is probably high enough to create the deep level defects to certain saturation. V-N-co-doped films are slightly better compared to V- and N-doped films, again most likely due to the elimination of recombination centers.

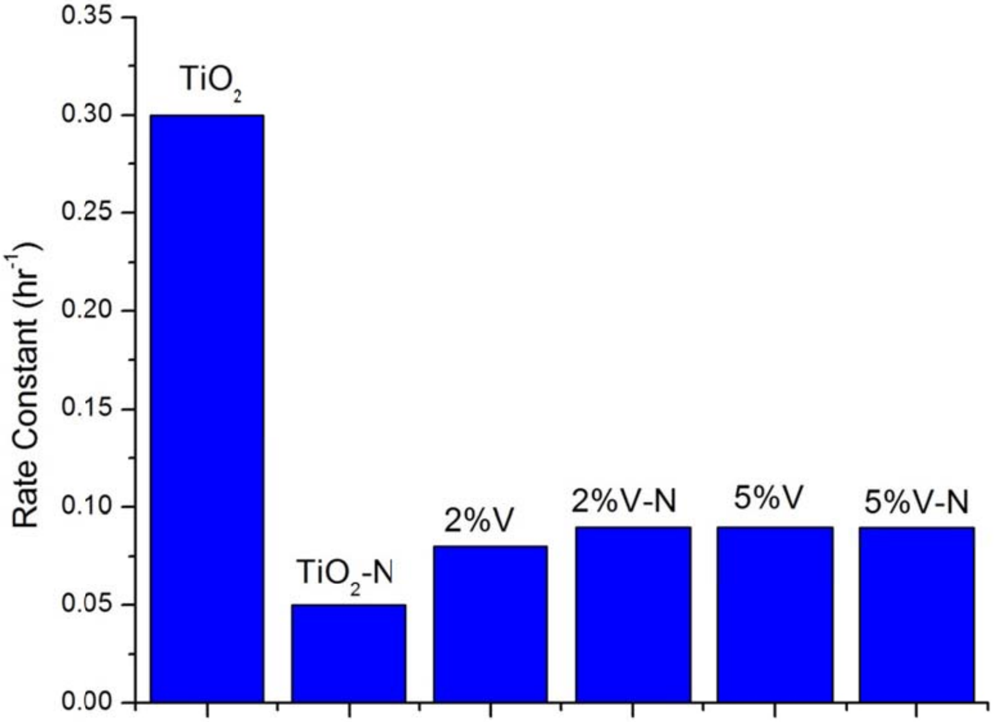

Figure 3-54: UV-light photocatalytic activity of vanadium and vanadium-nitrogen co-doped films. Nitrogen concentration is estimated to be 10 at. % in all N-doped films. Photocatalytic activity of undoped and nitrogen-doped titanium dioxide films are given for comparison.

Low photocatalytic activity of V-doped TiO_2 despite its high optical absorption can be explained as follows. Basic steps of photocatalysis are (a) creation of electron-hole pairs by illumination, (b) efficient separation of the electron-hole pairs so that they do not recombine to release heat, (c) transportation of the pairs to the surface, (d) collection of the free electron on the surface by an acceptor (usually oxygen), and (e) oxidation of the donor on the surface by the holes. The first requirement can be achieved by formation of defect levels within the band gap and can be easily characterized by optical analysis of the structure. Efficient separation and successful transportation of the carriers, on the other hand, require a small particle size, high crystallinity (with minimum defects) and a smoother band gap with as little deep-level energy traps as possible. Thus; visible light activity of the V-doped films should be coming with a cost of decreased efficiency due to the decreased lifetime of the carriers. As proposed by several authors before, thus, obtaining visible light activity requires introduction of shallow level defects into the structure. Another problem with the band gap modification of anatase is the position of the conduction band, which is an indication of reductive power of the semiconductor, being slightly higher than the O_2/O_2^- potential ($E° = -0.32$ V vs. NHE) (Figure 3-55). So, any modification of the conduction band is not desired as this would result in a semiconductor with excess electrons on the surface which cannot be collected by O_2 unless there is another acceptor in the environment. This leads to surface recombination and the loss of photocatalytic activity. Surface coupling with noble metals such as Pt, Pd, or Au also can help to decrease the surface recombination. In this case, however, two problems exist: (a) overall decrease in the reaction surface area as these metals cover some of the semiconductor surface, and (b) limited capacity of these metals to collect electrons, contrary to abundant O_2 which can perform this function indefinitely. It is therefore, desirable to engineer the band gap without causing bulk or surface recombination.

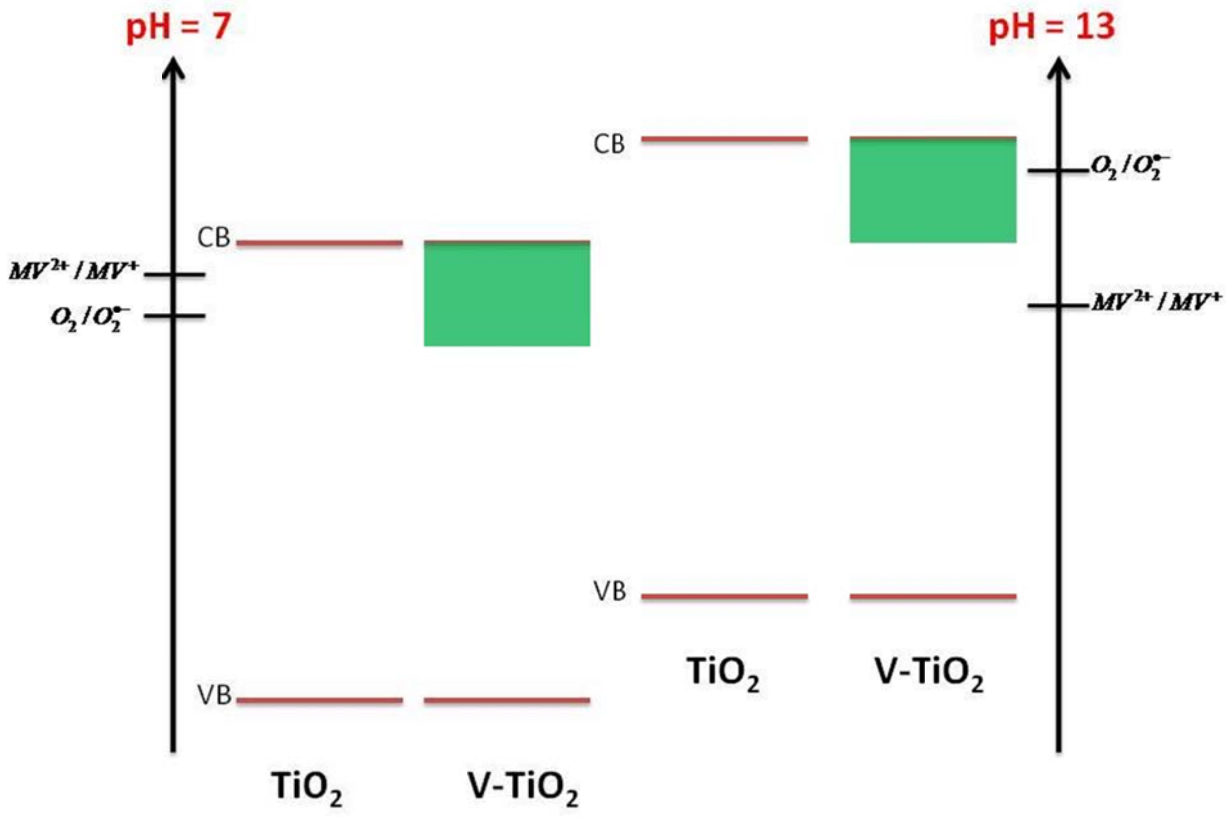

Figure 3-55: Electronic potentials of TiO_2 and V-doped TiO_2 in aqueous solutions at pH 7 and pH 14.

Density of states (DOS) plot of the V- and V, N-doped anatase is shown in Figure 3-56. Calculated band gap of anatase is 2.12 eV, narrower than the experimental band gap of 3.2 eV, which is the known underestimation of band gaps in LDA and GGA methods. The valence band of anatase was roughly same in V-doped TiO_2, but two new levels appeared within the band gap, one is a shallow defect level just below conduction band and the other one is a deep-level defect state 1.22 eV above the valence band. Based on the calculated DOS, thus, it seems possible to narrow the band gap of TiO_2 by V-doping whereas shallow defect level below conduction band and the deep-level defect can cause bulk and surface recombination, respectively. However, it is important to note that the deep-level created by V-doping is not large enough to trap all carriers created by photo-activation since oxygen vacancies are also known to create deep-level defects inside the band gap of anatase, though they are not enough to cease the photocatalytic activity. Modification of the conduction band is, however, a more difficult problem since it results in surface recombination.

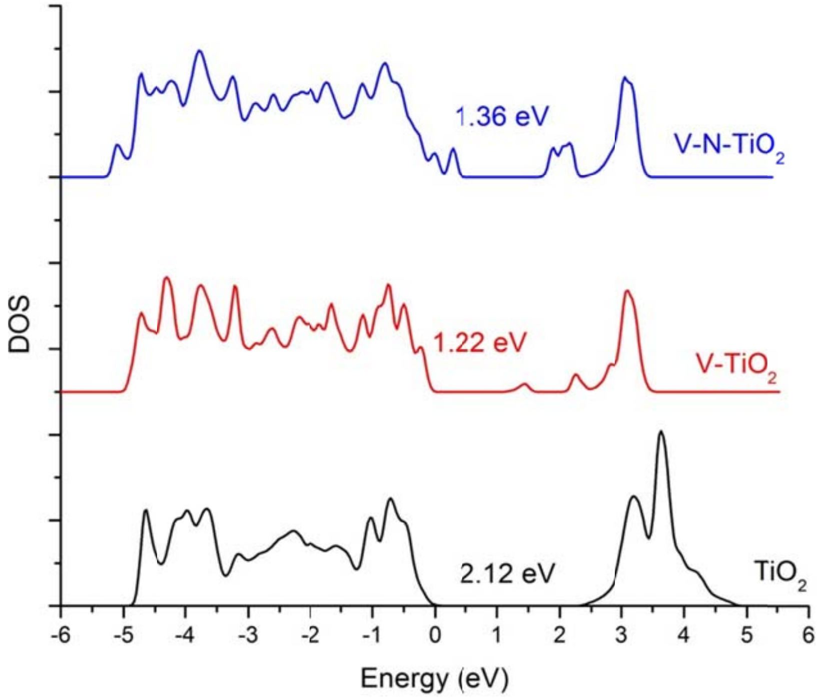

Figure 3-56: Density of States (DOS) plot of TiO_2 (anatase), V-doped TiO_2, and V,N-doped TiO_2.

3.7. Formation of MoO3 Nanobelts on Titanium Dioxide Films

3.7.1. Experimental

To produce α-MoO_3, molybdenum pentachloride ($MoCl_5$) (Alfa-Aesar, 99.6%) was dissolved in N,N-dimethyl formamide (DMF) (Sigma-Aldrich, anhydrous, 99.8%), which yielded a green transparent solution. 150 μl of this solution was dropped onto a TiO_2 coated (ca. 70 nm) glass slide (2 x 2 cm,) using a micropipette. TiO_2 coating of the glass slides was done via a sol-gel method as reported previously (Kurtoglu, Longenbach et al. 2010). Briefly, 120 g ethyl alcohol (200-proof, Electron Microscopy Sciences) and 15 g Ti-(O-i-C_3H_7)$_4$ (Alfa-Aesar, 98%) were mixed and subsequently stirred on a magnetic stirrer for 30 minutes. Then, a mixture of 0.96 g deionized water (18 MΩ), 0.52 g HCl (Fisher Science, 38%), 1 g poly (ethylene glycol) (Sigma-Aldrich, M.W. = 2000) and 6.3 g ethyl alcohol was added drop-wise to the main solution. The solution was stirred for 2 hours. Then, 9.6 g acetylacetone (Sigma-Aldrich, 98%) and 5 ml of deionized water were added to the prepared sol and stirred for an additional hour. Film was prepared by dip-coating (MTI Dip Coater HL-01); for this purpose, a glass microscope slide (Erie Scientific) were dipped into the prepared solution and withdrawn at a constant speed of 100 mm/min followed by calcination at 400°C for 30 minutes. After the deposition of the $MoCl_5$-DMF mixture on TiO_2 coated glass slides, the mixture turned from green to brown with increasing wait time and humidity, which is an indication of hydrolysis. Coated samples were placed into a pre-heated furnace to 500°C within 10 minutes after deposition of the $MoCl_5$-DMF mixture and calcined for 30 minutes. Same procedures were repeated on plain glass microscope slide and TiO_2 coated quartz slides to evaluate the effect of substrate. Samples were characterized by scanning electron microscopy (Zeiss Supra 50VP), transmission electron microscopy (JEOL JEM 2100), UV-Vis spectrophotometry (Thermo Scientific Evolution 600), and x-ray diffraction analysis (Siemens D500).

3.7.2. Results and Discussion

SEM images show that the substrates were covered with belt-like anisotropic crystals with their long end directed upwards, as shown in Figure 3-57a,b. Obtained nanobelts were typically 6 to 8 μm in length and 0.4-0.5 μm in width. Typical thickness of the nanobelts was approximately 50 nm. XRD analysis (Figure 3-57d) was in agreement with the previously reported α-MoO_3 patterns whereas strong anisotropy was evident from the relative intensities of the peaks, particularly the (021) peak. As seen from the TEM image and respective SAED pattern (Figure 3-57c), nanobelts were single crystalline and had a principal growth direction along <001> and the sideways growth along <100>.

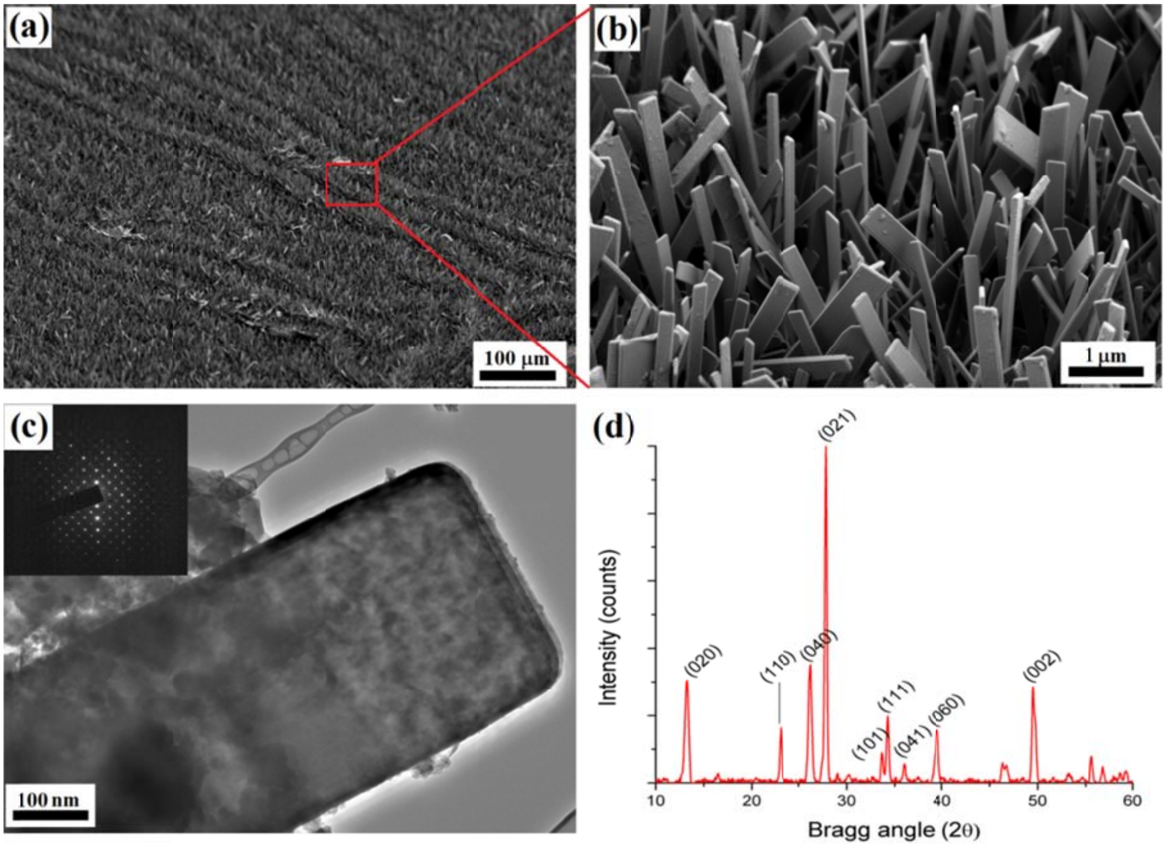

Figure 3-57: **Low-magnification (a) and high-magnification (b) SEM images of MoO_3 nanobelts. A TEM image and a single-crystal SAED pattern (inset) of a typical nanobelt are shown in (c). XRD pattern of nanobelts is shown in (d).**

Our experiments have shown that the obtained morphology strongly depended on the type of the substrate, solvent used for dissolving $MoCl_5$, and the heating rate. When plain soda-lime glass was used as a substrate, rod-like structures with their growth direction parallel to the substrate were obtained (Figure 3-58a). XRD analysis (Figure 3-58b) of the structure shows that these crystals were mainly composed of α-MoO_3 with (0k0) planes aligned parallel to the surface. Some sodium molybdate formation (Na_2MoO_4) was also evident from the diffraction pattern. Thus, this approach allows synthesis of adherent α-MoO_3 coatings on glass. We assume that sodium diffusion was responsible for the change in the α-MoO_3 growth habit.

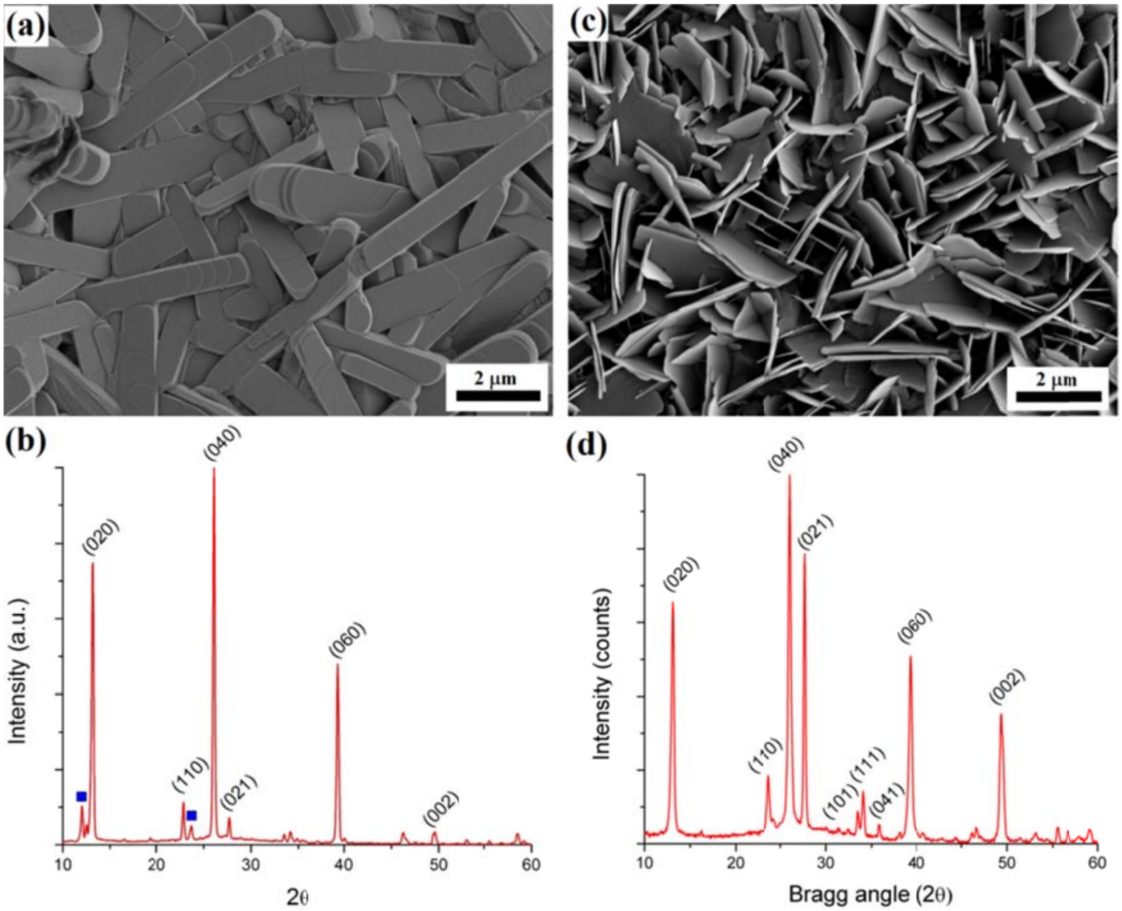

Figure 3-58: SEM images and XRD patterns of α-MoO_3 on TiO_2 coated (a,b) plain soda-lime glass and (c,d) quartz slides; both coatings were calcined at 500°C. (■ - Na_2MoO_4)

When TiO_2 coated quartz substrates were used, nanoplatelets (Figure 3-58c) with their (0k0) planes perpendicular to the substrate were observed. The nanoplatelets were mechanically more intact after handling (scratching, peeling off etc.) compared to nanobelts due to smaller aspect ratio and intersecting plates forming a rigid structure. Therefore, despite their smaller aspect ratio and lower surface area, they may be more suitable for practical applications as a coating, when durability and wear resistance is required.

In order to better understand the growth process, we prepared a set of samples on glass slides and calcined them by heating with the rate of 50°C/min to 350°C, 400°C and 450°C. Samples were taken out of the furnace at each temperature and quenched in air. At 350°C, formation of plate-like structures was evident on the surface (Figure 3-59), whereas nanobelts were already formed at 400°C (Figure 3-59b).

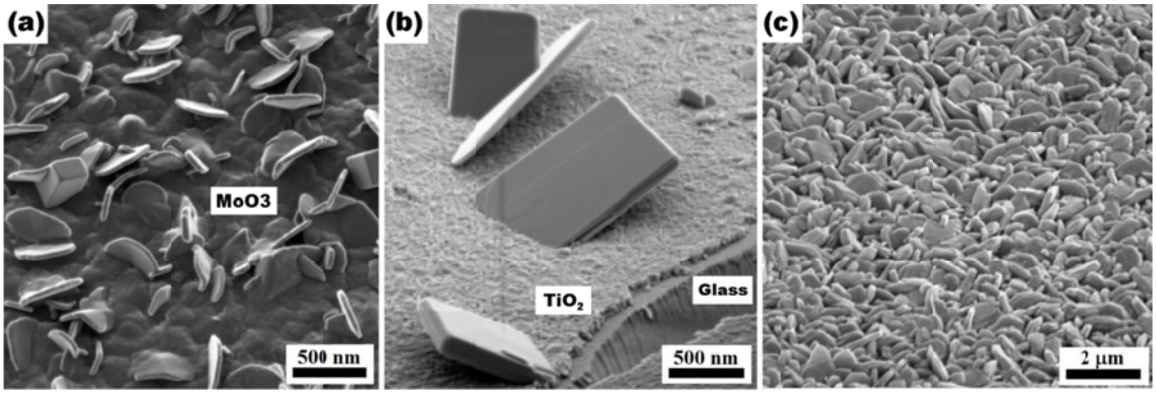

Figure 3-59: **MoO_3 structures obtained after quenching at (a) 350°C and (b) 400°C. (c) SEM image of the film prepared by using 2-propanol as the solvent.**

Based on the observations above, it can be concluded that anisotropic growth of α-MoO_3 nanobelts with their (0k0) planes perpendicular to the substrate plane was favored on TiO_2. The low lattice mismatch between the (010) plane of α-MoO_3 (a = 3.963 Å, b = 3.696 Å, c = 13.856 Å) and the (001) plane of anatase TiO_2 (a = b = 3.785 Å, c = 9.513 Å) (Figure 3-60a) favors preferential nucleation of (010) planes of α-MoO_3 on (001) planes of TiO_2. However, growth along [010] occurs through the creation of van der Waals bonds, which limits the growth rate compared to other principal growth directions, in which the growth occurs through the creation of ionic bonds (Figure 3-60b). Accordingly, planar growth rates along the principal axes of α-MoO_3 decrease in the following order: (001) > (100) >> (010) (Chu, Zhang et al. 2007). Since there is an excess supply of α-MoO_3 precursor due to fast heating rates, growth proceeds along the fastest direction, i.e. [001]. When the heating rate was decreased to 5°C/min, nanoplatelets were formed instead of nanobelts. The TiO_2 (anatase) films deposited on glass are polycrystalline and there is a mixture of faces exposed in random directions. Typically, an anatase crystal has a tetragonal prism structure consisting of eight (011) and two (001) faces (Figure 3-60c) (Oliver, Watson et al. 1997). (001) planes of TiO_2 laying parallel to the surface cannot nucleate nanobelts since (a) growth will be restricted by the compressive stress induced by the substrate due to fast heating and (b) α-MoO_3 supply is provided in the direction perpendicular to the film plane. The growth starts from the TiO_2 film surface and proceeds outwards since heterogeneous nucleation is typically faster than homogeneous nucleation. Thus, those (001) planes of TiO_2, which are oriented at an angle to the substrate, act as preferred nucleation and growth sites for the formation of α-MoO_3 nanobelts. The proposed mechanism is schematically shown in Figures 3-60d-e.

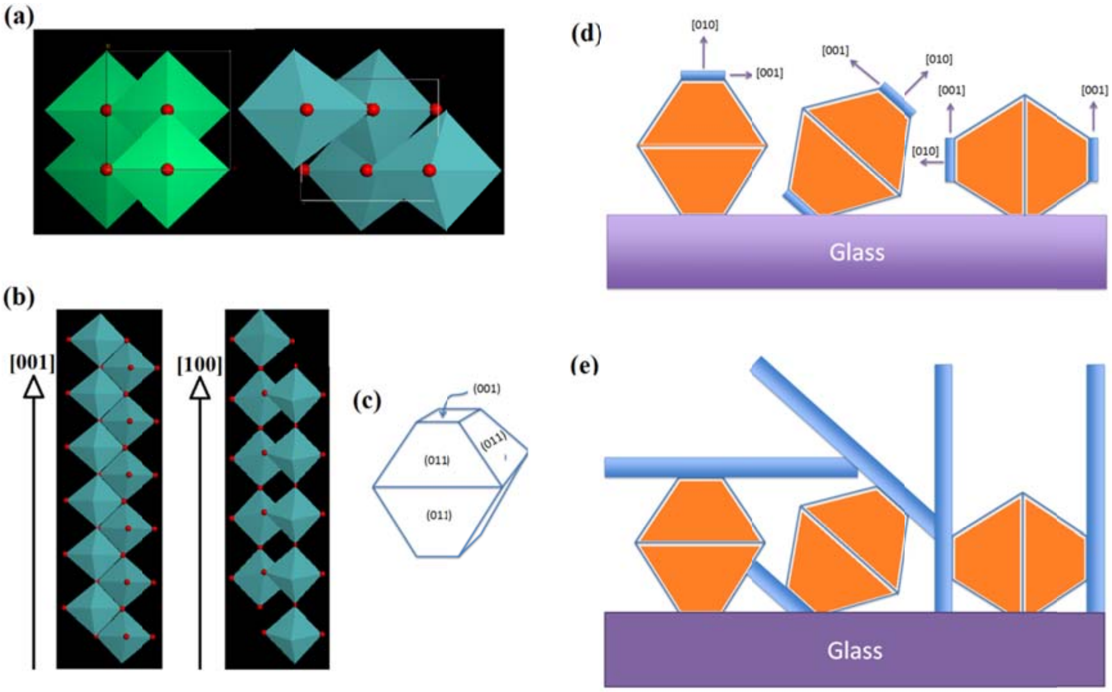

Figure 3-60: (a) (001) Anatase plane (left) and (010) MoO_3 plane. (b) Principal growth directions of MoO_3. (c) A typical anatase crystal. (d) nucleation of (010) MoO_3 on (001) faces of polycrystalline anatase and (e) growth of nanobelts.

It is important to note that rate of nucleation and growth should be carefully controlled to sustain the desired growth. For example, when samples were heated with a speed of 5°C/min, nanobelts were not observed. This can be explained by the high nucleation density due to the slow evaporation of DMF (b.p. = 153°C), during which nuclei are created, but growth is limited as the temperature is well below crystallization temperature. The solvent used to dissolve $MoCl_5$ was also one of the determining parameters on the obtained structure as suggested by several authors (Dong and Dunn 1998; Epifani, Imperatori et al. 2004). When 2-propanol was used as solvent in place of DMF, hydrolysis occured quickly, as evident from the dark blue color of the deposited solution only a few minutes after coating. Dimethyl sulfoxide gave similar results to DMF while methanol produced results similar to 2-propanol. In the case of 2-propanol, the resulting structure is a film composed of fine crystals of α-MoO_3, indicative of a high nucleation rate (Figure 3-59c). On the other hand, it was quite surprising to observe nanoplatelets on TiO_2 coated quartz (Figure 3-58c) rather than nanobelts, similar to the ones obtained on TiO_2 coated soda-lime glass. There are only two differences between TiO_2 coated quartz and glass substrates. The first is the high alkali content of soda-lime glass. In particular, sodium can diffuse easily through TiO_2 films (Watanabe, Fukayama et al. 2000) and may react with $MoCl_5$ to form NaCl and/or Na_2MoO_4, although this amount should be lower compared to an uncoated surface. Second is the thermal expansion of the substrate. Quartz has one of the lowest coefficients of thermal expansion (CTE) (ca. 0.5×10^{-6}/°C (Roy, Agrawal et al. 1989))while soda lime glass has a very high CTE (ca. 7.6×10^{-6}/°C (Mi-tang and Jin-shu 2010)). Thus, coatings on a glass substrate tend to experience a lower compressive stress than the ones on quartz. However, we believe that the alkali content is more important, as evidenced by the decrease of nanobelt density with increasing TiO_2 coating thickness (not shown). Increasing the TiO_2 thickness from ca. 80 nm to 300 nm significantly decreased the nanobelt density per unit of surface area; a thicker titania film led to a decrease in sodium content. Although the exact mechanism is still under investigation, some sodium diffusion through TiO_2 film appears to be necessary to obtain highly anisotropic α-MoO_3 structures.

One-dimensional nanostructures attract great attention in solar cells and photocatalytic applications for light trapping as well as in electrochemical applications (Brezesinski, Wang et al. 2010) due to their high surface area and surface roughness. α-MoO_3 nanobelts grown on an inexpensive glass substrate with such an easy method can be utilized as templates to produce active structures for solar cells and photocatalytic applications. To demonstrate the light trapping ability, obtained α-MoO_3 nanobelts were sputter coated with carbon. As can be seen from its total reflection spectra (Figure 3-61), the reflection of carbon-coated nanobelts was less than 4%, compared to 20% for carbon-coated glass. Nanoplatelets on quartz samples also gave low reflection values (less than 7%).

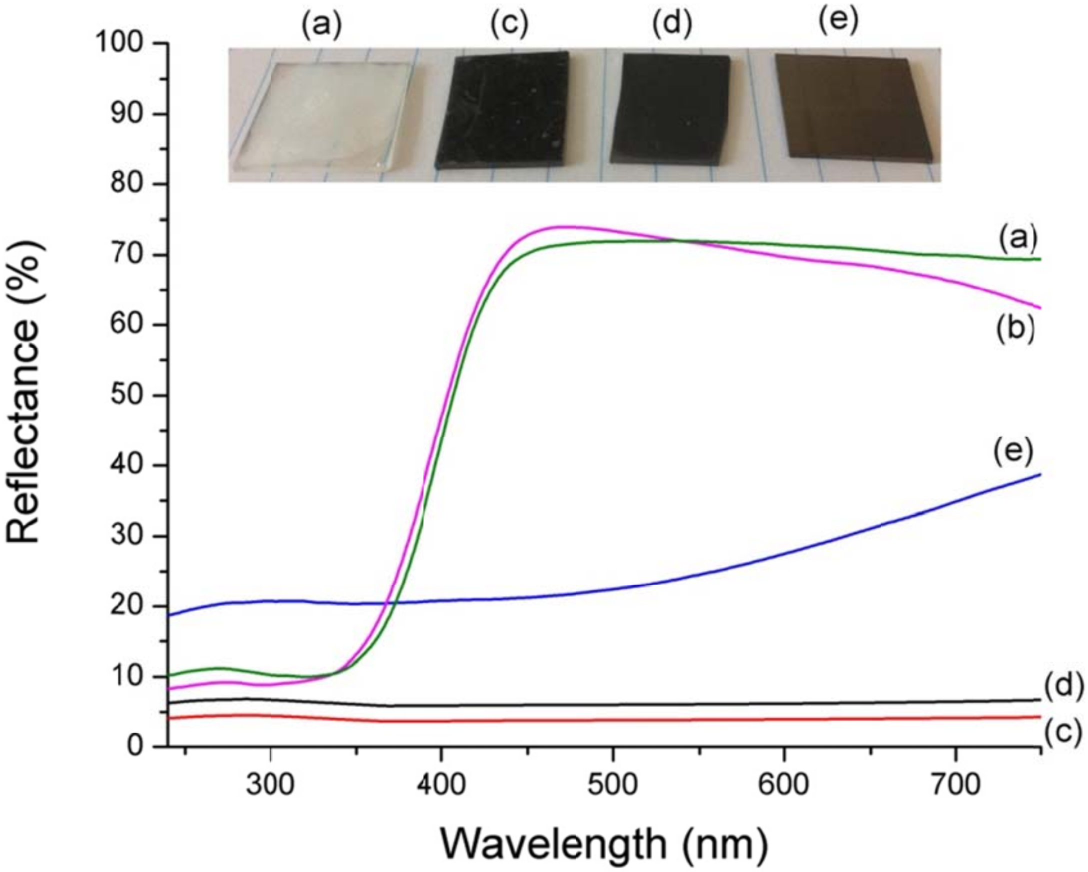

Figure 3-61: **Total reflection spectra and photographs of (a) MoO_3 nanobelts, (b) MoO_3 nanoplatelets, (c) carbon-coated MoO_3 nanobelts, (d) carbon-coated MoO_3 nanoplatelets, and (e) carbon-coated glass.**

For photocatalytic applications, α-MoO_3 nanobelts were first coated by SiO_2 using dip coating and then again dip coated with TiO_2. The resultant film was much more active compared to the film coated on plain glass, possibly due to its much higher surface area (Figure 3-62). Approximately 10 times more dye was decomposed within the first 2 hours by the TiO_2 coating on nanobelts compared to conventionally prepared (Kurtoglu, Longenbach et al. 2010) TiO_2 film on glass. Although we prepared the coatings by a dip-coating process, a gas phase deposition method should be more suitable as it is difficult to prepare a uniform coating on these structures by liquid phase deposition methods.

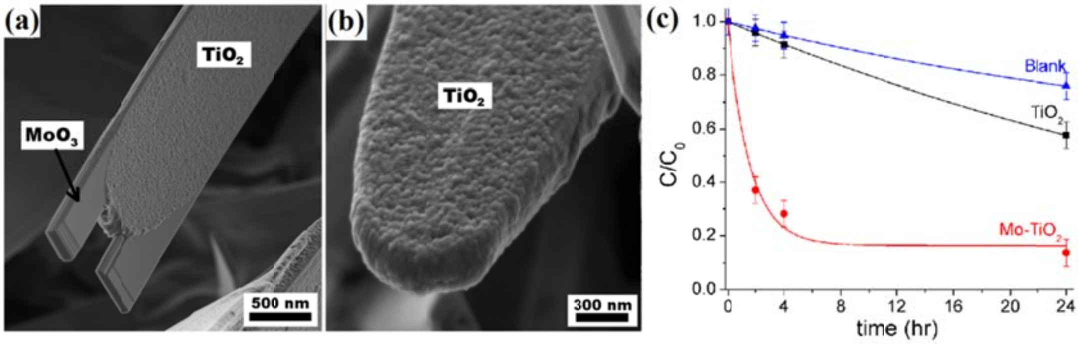

Figure 3-62: **SEM images of the TiO_2 coated MoO_3 nanobelts (a,b) and a plot showing photocatalytic degradation of methylene blue by TiO_2 coated MoO_3 nanobelts, TiO_2 film and a glass substrate (c).**

In order to demonstrate another application area, contact angle measurements were performed by sessile drop method on plain, carbon-coated, and fluorosilane coated α-MoO_3 nanobelts. Flurosilane coating was prepared by soaking nanobelt coated glass in 10 mM octadeyl-fluorosilane – hexane solution for 30 min followed by annealing at 200°C for 10 minutes. The plain nanobelt film was superhydrophilic with a contact angle of zero, possibly due to the hydration of the nanobelts, which also resulted in the nanobelt film to peel off the surface most probably due to stresses associated with the intercalation. After coating with carbon or fluorosilane, films became stable and did not show any sign of peeling or delamination after soaking in water for at least a day. Carbon coated film was hydrophobic with a contact angle of 105° (Figure 3-63a), whereas fluorosilane coated film attained a superhydrophobic state with a contact angle of 154° (Figure 3-63b).

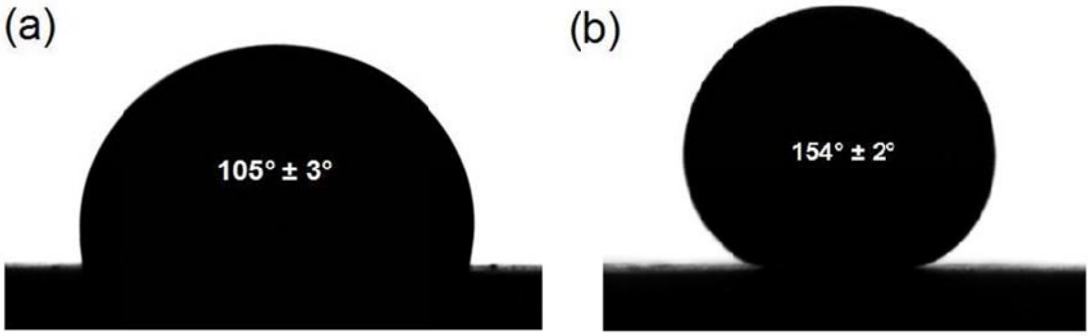

Figure 3-63: Contact angle of (a) carbon coated and (b) flurosilane coated MoO_3 nanobelts, as determined by the sessile drop method.

3.7.3. Conclusion

In summary, a simple yet effective method is demonstrated to produce high surface area α-MoO_3 structures on TiO_2 coated substrates. Depending on the substrate used, it was possible to obtain highly anisotropic structures or plate-like structures with a large aspect ratio and high surface area which can be utilized in several applications, such as solar cells, photo-catalysis and superhydrophobic surfaces.

CHAPTER 4) SUMMARY AND CONCLUSIONS

- A systematic approach was used to investigate the effect of doping on the photocatalytic, electronic and mechanical properties of sol-gel titanium dioxide films were investigated. The aim of this study is to answer the question: “How can sol-gel titanium dioxide films on glass substrates be made better by doping/alloying with other elements?” Particular attention was given to the key issues of the current titanium dioxide technologies: (i) lack of visible light activity, (ii) the negative effect of the glass substrate and (iii) low surface area of the films. In addition, nanoindentation studies were performed on those films to find out the cases when it is challenging to put a high photocatalytic activity film into use where high abrasion/weathering resistance is necessary. Theoretical calculations were utilized to understand the thermodynamics and electronic properties of doped titanium dioxide.

- Effects of calcination temperature and the heating rate on the structure, photocatalytic and mechanical properties of undoped sol-gel titanium dioxide films on glass substrates were investigated. It was found that an optimum calcination temperature and heating rate range exist and that photocatalytic and mechanical properties are degraded outside this range. A calcination temperature above 450°C is necessary to ensure sufficient crystallization of the films. Mechanical properties of the films are strongly influenced by the heating rate where higher heating rates are beneficial. In general, a calcination temperature around 500°C with a heating rate between 5°C/min and 10°C/min gives the optimum combination of photocatalytic activity and mechanical properties. The selected optimum parameters were used as guideline for the rest of studies.

- Theoretical calculations utilizing Density Functional Theory (DFT) were conducted to model doping process with various metal and metal-nitrogen combinations. It was found that the energy cost of substituting titanium with a metal dopant is directly related to the position of that particular metal in the periodic table. The group number of the dopant metal on the periodic table has a substantial effect on the energy cost of doping. The effect of period number is minor. In general, energy cost of substituting titanium in the anatase lattice with transition metal "X" was found to be roughly proportional to the distance between titanium and "X" in the transition block. The reverse is true outside the transition block, i.e. the longer the distance, the higher the energy cost is. Metal doping alone does not cause a dramatic change in the optical spectra, however significantly improved visible light absorption was obtained with certain metal-nitrogen combinations such as Cr-N and V-N.
- Since sodium diffusion is proved to be a major problem for titanium dioxide films on glass substrates, metal-doping was investigated to compensate the deleterious effect of sodium. It was found that not only the chosen metal affects

the photocatalytic activity but the metal precursor as well. Chlorides of molybdenum and tantalum were determined to be very effective to neutralize the sodium diffusion by reacting with the diffused sodium to form sodium chloride on the film surface which can easily be washed away. When mechanical properties are important, gallium doping was found to be a perfect dopant in that it improves the photocatalytic activity (though not as much as molybdenum and tantalum) and mechanical properties. Unfortunately, no visible light activity was detected by metal-doping.

- Visible-light photocatalytic activity was investigated with so-called self-doped titanium dioxide films. For this purpose, carbothermal reduction of titanium dioxide films was performed at various calcination temperatures to produce oxygen-deficit titanium dioxide films and results were compared with the ones calcined in oxidizing atmosphere. While carbothermal reduction brought some visible light activity, it typically resulted in degraded mechanical properties.
- Nitrogen-doped titanium dioxide films were studied for visible-light photocatalytic activity as these films absorb part of the visible spectrum. Although certain amount of visible light activity was observed with nitrogen doping, this effect was not directly proportional to the optical absorption. Visible light activity was optimum at a certain nitrogen concentration above which this positive effect diminished. On the other hand, visible light activity came at the cost of UV-light activity and this behavior was amplified with increasing nitrogen concentrations. Mechanical properties of nitrogen doped films were, overall,

inferior to undoped titanium dioxide films; which was surprising since titanium nitride is an extremely hard material. The beneficial effect of nitrogen doping was only seen at relatively higher nitrogen doping concentrations which was detrimental to both visible and UV light activity.

- Metal-nitrogen co-doping was investigated to address the shortcomings of nitrogen-doped titanium dioxide films. Overall 30-35% increase in the visible light activity as well as a non-negligible improvement in the mechanical properties was obtained with some of the metal-nitrogen combinations (in particular, tantalum, vanadium, and molybdenum). On the other hand, UV-light activity was phenomenally improved with chromium co-doping (up to 7-fold) and less dramatically with vanadium co-doping (2-fold). Cr-N and V-N co-doped films were investigated in detail to understand the observed behavior and some answers were given based on the extensive theoretical calculations.
- Among the metal dopants, molybdenum was studied in detail due to its interesting interaction with titanium dioxide and glass to form one- and two-dimensional structures. By carefully controlling the sol-gel and calcination parameters, high surface area molybdenum oxide structures were synthesized on titanium dioxide coated glass, which was further used as high surface area template for photocatalytic titanium dioxide film deposition. The ease of the method, which arose while investigating metal-doped titanium dioxide films, allows formation of high surface area glass substrates which can be used in improving catalytic reactions.

- Last, but not the least, results obtained during the course of this study have been used to develop the first commercial photocatalytic-antimicrobial tableware glass.

REFERENCES

(2009). "US Geological Survey Minerals Yearbook."

Abou-Helal, M. O. and W. T. Seeber (2002). "Preparation of TiO_2 thin films by spray pyrolysis to be used as a photocatalyst." Applied Surface Science **195**(1-4): 53-62.

Ahn, Y. U., E. J. Kim, et al. (2003). "Variation of structural and optical properties of sol-gel TiO_2 thin films with catalyst concentration and calcination temperature." Materials Letters **57**(30): 4660-4666.

Allain, E., S. Besson, et al. (2007). "Transparent mesoporous nanocomposite films for self-cleaning applications." Advanced Functional Materials **17**(4): 549-554.

Aouadi, S. M., D. M. Schultze, et al. (2001). "Growth and characterization of Cr_2N/CrN multilayer coatings." Surface and Coatings Technology **140**(3): 269-277.

Asahi, R., T. Morikawa, et al. (2001). "Visible-Light Photocatalysis in Nitrogen-Doped Titanium Oxides." Science **293**(5528): 269-271.

Asahi, R., Y. Taga, et al. (2000). "Electronic and optical properties of anatase TiO_2." Physical Review B **61**(11): 7459.

ASTM (2008). ASTM G173-03 Standard Tables for Reference Solar Spectral Irradiances.

Balaji, S., Y. Djaoued, et al. (2006). "Phonon confinement studies in nanocrystalline anatase-TiO_2 thin films by micro Raman spectroscopy." Journal of Raman Spectroscopy **37**(12): 1416-1422.

Barnard, A. S. and P. Zapol (2004). "Effects of particle morphology and surface hydrogenation on the phase stability of TiO_2." Physical Review B **70**: 235403.

Berreman, D. W. (1963). "Infrared Absorption at Longitudinal Optic Frequency in Cubic Crystal Films." Physical Review **130**(6): 2193.

Bhatia, S. and B. Sheldon (2008). "Compositional Stresses in Polycrystalline Titania Films." Journal of the American Ceramic Society **91**(12): 3986-3993.

Bickley, R. I., T. Gonzalez-Carreno, et al. (1991). "A structural investigation of titanium dioxide photocatalysts." Journal of Solid State Chemistry **92**(1): 178-190.

Bond, G. C. and S. F. Tahir (1991). "Vanadium oxide monolayer catalysts Preparation, characterization and catalytic activity." Applied Catalysis **71**(1): 1-31.

Borgarello, E., J. Kiwi, et al. (1982). "Visible light induced water cleavage in colloidal solutions of chromium-doped titanium dioxide particles." Journal of the American Chemical Society **104**(11): 2996-3002.

Brezesinski, T., J. Wang, et al. (2010). "Ordered mesoporous [alpha]-MoO_3 with iso-oriented nanocrystalline walls for thin-film pseudocapacitors." Nat Mater **9**(2): 146-151.

Brezová, V., A. Blazková, et al. (1997). "Phenol decomposition using Mn^+/TiO_2 photocatalysts supported by the sol-gel technique on glass fibres." Journal of Photochemistry and Photobiology A: Chemistry **109**(2): 177-183.

Brinker, C. J., A. J. Hurd, et al. (1992). "Review of sol-gel thin film formation." Journal of Non-Crystalline Solids **147-148**: 424-436.

Brinker, J. and G. Scherer (1990). Sol-gel science: the physics and chemistry of sol-gel processing. San Diego, CA, Academic Press.

Busca, G., P. Tittarelli, et al. (1987). "Evidence for the formation of an antase-type V-Ti oxide solid-state solution." Journal of Solid State Chemistry **67**(1): 91-97.

Cao, F., G. Oskam, et al. (1995). "Electrical and optical properties of porous nanocrystalline TiO_2 films." The Journal of Physical Chemistry **99**(31): 11974-11980.

Carp, O., C. L. Huisman, et al. (2004). "Photoinduced reactivity of titanium dioxide." Progress in Solid State Chemistry **32**(1-2): 33-177.

Cater, S. R., M. I. Stefan, et al. (2000). "UV/H_2O_2 Treatment of Methyl tert-Butyl Ether in Contaminated Waters." Environmental Science & Technology **34**(4): 659-662.

Chatterjee, D. and S. Dasgupta (2005). "Visible light induced photocatalytic degradation of organic pollutants." Journal of Photochemistry and Photobiology C: Photochemistry Reviews **6**(2-3): 186-205.

Chen, X. and S. S. Mao (2007). "Titanium Dioxide Nanomaterials: Synthesis, Properties, Modifications, and Applications." Chemical Reviews **107**(7): 2891-2959.

Chu, W. G., L. N. Zhang, et al. (2007). "Direct thermal oxidization evaporation growth, structure, and optical properties of single-crystalline nanobelts of molybdenum trioxide." Journal of Materials Research **22**(6): 1609-1617.

Colbeau-Justin, C., M. Kunst, et al. (2003). "Structural influence on charge-carrier lifetimes in TiO_2 powders studied by microwave absorption." Journal of Materials Science **38**(11): 2429-2437.

Daneshvar, N., D. Salari, et al. (2003). "Photocatalytic degradation of azo dye acid red 14 in water: investigation of the effect of operational parameters." Journal of Photochemistry and Photobiology A: Chemistry **157**(1): 111-116.

Di Valentin, C., G. Pacchioni, et al. (2004). "Origin of the different photoactivity of N - doped anatase and rutile TiO_2." Physical Review B **70**(8): 085116.

Di Valentin, C., G. Pacchioni, et al. (2005). "Characterization of Paramagnetic Species in N-Doped TiO_2 Powders by EPR Spectroscopy and DFT Calculations." The Journal of Physical Chemistry B **109**(23): 11414-11419.

Donachie, M. J. (1988). Titanium: A Technical Guide. Metals Park, OH, ASM International.

Dong, W. and B. Dunn (1998). "Sol-gel synthesis of monolithic molybdenum oxide aerogels and xerogels." Journal of Materials Chemistry **8**(3): 665-670.

Dutoit, D. C. M., M. Schneider, et al. (1995). "Titania-Silica Mixed Oxides : I. Influence of Sol-Gel and Drying Conditions on Structural Properties." Journal of Catalysis **153**(1): 165-176.

Dvoranová, D., V. Brezová, et al. (2002). "Investigations of metal-doped titanium dioxide photocatalysts." Applied Catalysis B: Environmental **37**(2): 91-105.

Emili, M., L. Incoccia, et al. (1985). "Structural investigations of TiO_2-SiO_2 glassy and glass-ceramic materials prepared by the sol-gel method." Journal of Non-Crystalline Solids **74**(1): 129-146.

Epifani, M., P. Imperatori, et al. (2004). "Synthesis and Characterization of MoO_3 Thin Films and Powders from a Molybdenum Chloromethoxide." Chemistry of Materials **16**(25): 5495-5501.

Fu, G., P. S. Vary, et al. (2005). "Anatase TiO_2 Nanocomposites for Antimicrobial Coatings." The Journal of Physical Chemistry B **109**(18): 8889-8898.

Fujishima, A. and K. Honda (1972). "Electrochemical Photolysis of Water at a Semiconductor Electrode." Nature **238**(5358): 37-38.

Fujishima, A. and T. Rao (1997). "Recent advances in heterogeneous TiO_2 photocatalysis." Journal of Chemical Sciences **109**(6): 471-486.

Gaillard, Y., V. J. Rico, et al. (2009). "Nanoindentation of TiO_2 thin films with different microstructures." Journal of Physics D: Applied Physics(14): 145305.

Gartner, M., P. Osiceanu, et al. (2008). "Investigation on the nitrogen doping of multilayered, porous TiO_2 thin films." Thin Solid Films **516**(22): 8184-8189.

Gartner, M., R. Scurtu, et al. (2004). "Spectroellipsometric characterization of sol-gel TiO_2-CuO thin coatings." Thin Solid Films **455-456**: 417-421.

Ghijsen, J., L. H. Tjeng, et al. (1988). "Electronic structure of Cu_2O and CuO." Physical Review B **38**(16): 11322.

Grambow, B. and R. Müller (2001). "First-order dissolution rate law and the role of surface layers in glass performance assessment." Journal of Nuclear Materials **298**(1-2): 112-124.

Habel, D., O. Goerke, et al. (2008). "Phase Relations in the System TiO_2-V_2O_x under Oxidizing and Reducing Conditions." Journal of Phase Equilibria and Diffusion **29**(6): 482-487.

Hague, D. C. and M. J. Mayo (1994). "Controlling Crystallinity during Processing of Nanocrystalline Titania." Journal of the American Ceramic Society **77**(7): 1957-1960.

Hattori, A., K. Shimoda, et al. (1999). "Photoreactivity of Sol-Gel TiO_2 Films Formed on Soda-Lime Glass Substrates: Effect of SiO_2 Underlayer Containing Fluorine." Langmuir **15**(16): 5422-5425.

Herrmann, J.-M. (1999). "Heterogeneous photocatalysis: fundamentals and applications to the removal of various types of aqueous pollutants." Catalysis Today **53**(1): 115-129.

Herrmann, J.-M., J. Disdier, et al. (1984). "Effect of chromium doping on the electrical and catalytic properties of powder titania under UV and visible illumination." Chemical Physics Letters **108**(6): 618-622.

Hoffmann, M. R., S. T. Martin, et al. (1995). "Environmental Applications of Semiconductor Photocatalysis." Chemical Reviews **95**(1): 69-96.

Houas, A., H. Lachheb, et al. (2001). "Photocatalytic degradation pathway of methylene blue in water." Applied Catalysis B: Environmental **31**(2): 145-157.

Innocenzi, P. (2003). "Infrared spectroscopy of sol-gel derived silica-based films: a spectra-microstructure overview." Journal of Non-Crystalline Solids **316**(2-3): 309-319.

Iwasaki, M., M. Hara, et al. (2000). "Cobalt ion-doped TiO_2 photocatalyst response to visible light." Journal of Colloid and Interface Science **224**(1): 202-204.

Jha, A. and S. J. Yoon (1999). "Formation of titanium carbonitride phases via the reduction of TiO_2 with carbon in the presence of nitrogen." Journal of Materials Science **34**(2): 307-322.

Juliano, T., V. Domnich, et al. (2004). "Examining pressure-induced phase transformations in silicon by spherical indentation and Raman spectroscopy: A statistical study." Journal of Materials Research **19**(10): 3099-3108.

Justicia, I., P. Ordejón, et al. (2002). "Designed Self-Doped Titanium Oxide Thin Films for Efficient Visible-Light Photocatalysis." Advanced Materials **14**(19): 1399-1402.

Kabra, K., R. Chaudhary, et al. (2004). "Treatment of Hazardous Organic and Inorganic Compounds through Aqueous-Phase Photocatalysis: A Review." Industrial & Engineering Chemistry Research **43**(24): 7683-7696.

Kim, D.-W., T.-G. Kim, et al. (1999). "Low-firing of CuO-doped anatase." Materials Research Bulletin **34**(5): 771-781.

Klosek, S. and D. Raftery (2001). "Visible Light Driven V-Doped TiO_2 Photocatalyst and Its Photooxidation of Ethanol." The Journal of Physical Chemistry B **105**(14): 2815-2819.

Konstantinou, I. K. and T. A. Albanis (2004). "TiO_2-assisted photocatalytic degradation of azo dyes in aqueous solution: kinetic and mechanistic investigations: A review." Applied Catalysis B: Environmental **49**(1): 1-14.

Kurtoglu, M. E., T. Longenbach, et al. (2010). "Effect of calcination temperature and environment on photocatalytic and mechanical properties of ultra-thin sol-gel TiO_2 films." Journal of the American Ceramic Society **In press**.

Lachheb, H., E. Puzenat, et al. (2002). "Photocatalytic degradation of various types of dyes (Alizarin S, Crocein Orange G, Methyl Red, Congo Red, Methylene Blue) in water by UV-irradiated titania." Applied Catalysis B: Environmental **39**(1): 75-90.

Lakshmi, B. B., P. K. Dorhout, et al. (1997). "Sol-gel template synthesis of semiconductor nanostructures." Chemistry of Materials **9**(3): 857-862.

Langlet, M. (2003). Low Temperature Processing of Sol-Gel Thin Films in the SiO_2-TiO_2 Binary System. Handbook of Sol-Gel Science and Technology. S. Sakka, Kluwer Academic Publishing**:** 331-355.

Larsson, P.-O., A. Andersson, et al. (1996). "Combustion of CO and Toluene; Characterisation of Copper Oxide Supported on Titania and Activity Comparisons with Supported Cobalt, Iron, and Manganese Oxide." Journal of Catalysis **163**(2): 279-293.

Lawless, D., N. Serpone, et al. (1991). "Role of hydroxyl radicals and trapped holes in photocatalysis. A pulse radiolysis study." The Journal of Physical Chemistry **95**(13): 5166-5170.

Lee, B.-Y., K. Behler, et al. (2010). "Titanium dioxide-coated nanofibers for advanced filters." Journal of Nanoparticle Research.

Lee, D., M. F. Rubner, et al. (2006). "All-Nanoparticle Thin-Film Coatings." Nano Letters **6**(10): 2305-2312.

Lee, K.-S. and S. H. Lee (2007). "Influence of SiO_2 interlayer on the hydrophilicity of TiO_2/SiO_2/glass produced by RF-magnetron sputtering." Materials Letters **61**(16): 3516-3518.

Li, X., B. Bhushan, et al. "Mechanical characterization of micro/nanoscale structures for MEMS/NEMS applications using nanoindentation techniques." Ultramicroscopy **97**(1-4): 481-494.

Lu, Y., R. Ganguli, et al. (1997). "Continuous formation of supported cubic and hexagonal mesoporous films by sol-gel dip-coating." Nature **389**(6649): 364-368.

Maity, S. K., M. S. Rana, et al. (2001). "Studies on physico-chemical characterization and catalysis on high surface area titania supported molybdenum hydrotreating catalysts." Applied Catalysis A: General **205**(1-2): 215-225.

Mardare, D. and P. Hones (1999). "Optical dispersion analysis of TiO_2 thin films based on variable-angle spectroscopic ellipsometry measurements." Materials Science and Engineering B **68**(1): 42-47.

Marquez, E. and et al. (1992). "Calculation of the thickness and optical constants of amorphous arsenic sulphide films from their transmission spectra." Journal of Physics D: Applied Physics **25**(3): 535.

Mi-tang, W. and C. Jin-shu (2010). "Viscosity and thermal expansion of rare earth containing soda-lime-silicate glass." Journal of Alloys and Compounds **504**(1): 273-276.

Mills, A., N. Elliott, et al. (2002). "Novel TiO_2 CVD films for semiconductor photocatalysis." Journal of Photochemistry and Photobiology a-Chemistry **151**(1-3): 171-179.

Mills, A. and J. Wang (1999). "Photobleaching of methylene blue sensitised by TiO2: an ambiguous system?" Journal of Photochemistry and Photobiology A: Chemistry **127**(1-3): 123-134.

Miyauchi, M., A. Nakajima, et al. (2002). "Photocatalysis and Photoinduced Hydrophilicity of Various Metal Oxide Thin Films." Chemistry of Materials **14**(6): 2812-2816.

Monticone, S., R. Tufeu, et al. (2000). "Quantum size effect in TiO_2 nanoparticles: does it exist?" Applied Surface Science **162-163**: 565-570.

Mrowetz, M., W. Balcerski, et al. (2004). "Oxidative Power of Nitrogen-Doped TiO_2 Photocatalysts under Visible Illumination." The Journal of Physical Chemistry B **108**(45): 17269-17273.

Nakamura, I., N. Negishi, et al. (2000). "Role of oxygen vacancy in the plasma-treated TiO_2 photocatalyst with visible light activity for NO removal." Journal of Molecular Catalysis A: Chemical **161**(1-2): 205-212.

Nam, H. J., T. Amemiya, et al. (2004). "Photocatalytic Activity of Sol-Gel TiO_2 Thin Films on Various Kinds of Glass Substrates: The Effects of Na^+ and Primary Particle Size." J. Phys. Chem. B **108**(24): 8254-8259.

Nie, X. L., S. P. Zhuo, et al. (2009). "Doping of TiO_2 Polymorphs for Altered Optical and Photocatalytic Properties." International Journal of Photoenergy **ID 294042**.

Ocaña, M., J. V. Garcia-Ramos, et al. (1992). "Low-Temperature Nucleation of Rutile Observed by Raman Spectroscopy during Crystallization of TiO_2." Journal of the American Ceramic Society **75**(7): 2010-2012.

Ohno, T., K. Sarukawa, et al. (2002). "Crystal faces of rutile and anatase TiO_2 particles and their roles in photocatalytic reactions." New Journal of Chemistry **26**(9): 1167-1170.

Ohno, T., F. Tanigawa, et al. (1999). "Photocatalytic oxidation of water by visible light using ruthenium-doped titanium dioxide powder." Journal of Photochemistry and Photobiology A: Chemistry **127**(1-3): 107-110.

Ohsaka, T., F. Izumi, et al. (1978). "Raman spectrum of anatase, TiO_2." Journal of Raman Spectroscopy **7**(6): 321-324.

Ohtani, B., Y. Ogawa, et al. (1997). "Photocatalytic Activity of Amorphous−Anatase Mixture of Titanium(IV) Oxide Particles Suspended in Aqueous Solutions." The Journal of Physical Chemistry B **101**(19): 3746-3752.

Ohtani, B., Y. Okugawa, et al. (1987). "Photocatalytic activity of titania powders suspended in aqueous silver nitrate solution: correlation with pH-dependent surface structures." The Journal of Physical Chemistry **91**(13): 3550-3555.

Oliver, P. M., G. W. Watson, et al. (1997). "Atomistic simulation of the surface structure of the TiO_2 polymorphs rutile and anatase." Journal of Materials Chemistry **7**(3): 563-568.

Oliver, W. C. and G. M. Pharr (1992). "An improved technique for determining hardness and elastic modulus using load and displacement sensing indentation experiments." Journal Name: Journal of Materials Research; (United States); Journal Volume: 7:6: Medium: X; Size: Pages: 1564-1583.

Ollis, D. F., E. Pelizzetti, et al. (2002). "Photocatalyzed destruction of water contaminants." Environmental Science & Technology **25**(9): 1522-1529.

Osterwalder, J., T. Droubay, et al. (2005). "Growth of Cr-doped TiO_2 films in the rutile and anatase structures by oxygen plasma assisted molecular beam epitaxy." Thin Solid Films **484**(1-2): 289-298.

Palmisano, G., V. Augugliaro, et al. (2007). "Photocatalysis: A Promising Route for 21st Century Organic Chemistry." ChemInform **38**(48).

Pan, C.-C. and J. C. S. Wu (2006). "Visible-light response Cr-doped TiO_2-XN_X photocatalysts." Materials Chemistry and Physics **100**(1): 102-107.

Park, H. and W. Choi (2004). "Effects of TiO_2 surface fluorination on photocatalytic reactions and photoelectrochemical behaviors." Journal of Physical Chemistry B **108**(13): 4086-4093.

Park, M.-S. and M. Kang (2008). "The preparation of the anatase and rutile forms of Ag-TiO_2 and hydrogen production from methanol/water decomposition." Materials Letters **62**(2): 183-187.

Parker, J. C. and R. W. Siegel (1990). "Raman microprobe study of nanophase TiO_2 and oxidation-induced spectral changes." Journal of Materials Research **5**(6): 1246-1252.

Paulauskas, I. E., M. P. Brady, et al. (2006). "Corrosion behavior of CrN, Cr_2N and π phase surfaces on nitrided Ni-50Cr for proton exchange membrane fuel cell bipolar plates." Corrosion Science **48**(10): 3157-3171.

Paulose, M., K. Shankar, et al. (2006). "Anodic growth of highly ordered TiO_2 nanotube arrays to 134 mu m in length." Journal of Physical Chemistry B **110**(33): 16179-16184.

Paz, Y., Z. Luo, et al. (1995). "Photooxidative self-cleaning transparent titanium-dioxide films on glass." Journal of Materials Research **10**(11): 2842-2848.

Pichat, P., R. Enriquez, et al. (2010). "Investigations of Photo-Excited TiO_2 Based on Time Resolved Microwave Conductivity and Oxygen Isotopic Exchange." Solid State Phenomena **162**: 41-48.

Rengaraj, S. and X. Z. Li (2006). "Enhanced photocatalytic activity of TiO_2 by doping with Ag for degradation of 2,4,6-trichlorophenol in aqueous suspension." Journal of Molecular Catalysis A: Chemical **243**(1): 60-67.

Richter, C. and C. A. Schmuttenmaer (2010). "Exciton-like trap states limit electron mobility in TiO_2 nanotubes." Nat Nano **5**(11): 769-772.

Roy, R., D. K. Agrawal, et al. (1989). "Very Low Thermal Expansion Coefficient Materials." Annual Review of Materials Science **19**(1): 59-81.

Sakthivel, S., M. V. Shankar, et al. (2004). "Enhancement of photocatalytic activity by metal deposition: characterisation and photonic efficiency of Pt, Au and Pd deposited on TiO2 catalyst." Water Research **38**(13): 3001-3008.

Satoh, N., T. Nakashima, et al. (2008). "Quantum size effect in TiO_2 nanoparticles prepared by finely controlled metal assembly on dendrimer templates." Nat Nano **3**(2): 106-111.

Schubert, U. (2005). "Chemical modification of titanium alkoxides for sol-gel processing." Journal of Materials Chemistry **15**(35-36): 3701-3715.

Seery, M. K., R. George, et al. (2007). "Silver doped titanium dioxide nanomaterials for enhanced visible light photocatalysis." Journal of Photochemistry and Photobiology A: Chemistry **189**(2-3): 258-263.

Shannon, R. D. and J. A. Pask (1965). "Kinetics of the Anatase-Rutile Transformation." Journal of the American Ceramic Society **48**(8): 391-398.

Shimizu, K., H. Imai, et al. (1999). "Low-temperature synthesis of anatase thin films on glass and organic substrates by direct deposition from aqueous solutions." Thin Solid Films **351**(1-2): 220-224.

Shin, C.-K., Y.-K. Paek, et al. (2006). "Effect of CuO on the Sintering Behavior and Dielectric Characteristics of Titanium Dioxide." International Journal of Applied Ceramic Technology **3**(6): 463-469.

Smyth, D. M. (2000). The defect chemistry of metal oxides. New York, Oxford University Press.

Sunada, K., Y. Kikuchi, et al. (1998). "Bactericidal and Detoxification Effects of TiO_2 Thin Film Photocatalysts." Environmental Science & Technology **32**(5): 726-728.

Tada, H. and M. Tanaka (1997). "Dependence of TiO_2 Photocatalytic Activity upon Its Film Thickness." Langmuir **13**(2): 360-364.

Takeda, S., S. Suzuki, et al. (2001). "Photocatalytic TiO_2 thin film deposited onto glass by DC magnetron sputtering." Thin Solid Films **392**(2): 338-344.

Tan, P. H., S. Dimovski, et al. (2004). "Raman scattering of non-planar graphite: arched edges, polyhedral crystals, whiskers and cones." Philosophical Transactions of the Royal Society of London Series a-Mathematical Physical and Engineering Sciences **362**(1824): 2289-2310.

Tang, H., K. Prasad, et al. (1994). "Electrical and optical properties of TiO_2 anatase thin films." Journal of Applied Physics **75**(4): 2042-2047.

Tjeng, L. H., M. B. J. Meinders, et al. (1990). "Electronic structure of Ag_2O." Physical Review B **41**(5): 3190.

Tracey, S. M., S. N. B. Hodgson, et al. (1998). "The role and interactions of process parameters on the nature of alkoxide derived sol-gel films." Journal of Materials Processing Technology **77**(1-3): 86-94.

Tsumura, T., N. Kojitani, et al. (2002). "Carbon coating of anatase-type TiO_2 and photoactivity." Journal of Materials Chemistry **12**(5): 1391-1396.

Valentin, C. D., G. Pacchioni, et al. (2009). "Cr/Sb co-doped TiO_2 from first principles calculations." Chemical Physics Letters **469**(1-3): 166-171.

van de Krol, R., Y. Q. Liang, et al. (2008). "Solar hydrogen production with nanostructured metal oxides." Journal of Materials Chemistry **18**(20): 2311-2320.

Wang, R., K. Hashimoto, et al. (1997). "Light-induced amphiphilic surfaces." Nature **388**(6641): 431-432.

Wang, W., L.-W. Chiang, et al. (2003). "Decomposition of benzene in air streams by UV/TiO_2 process." Journal of Hazardous Materials **101**(2): 133-146.

Watanabe, T., S. Fukayama, et al. (2000). "Photocatalytic Activity and Photo-Induced Wettability Conversion of TiO_2 Thin Film Prepared by Sol-Gel Process on a Soda-Lime Glass." Journal of Sol-Gel Science and Technology **19**(1): 71-76.

Whang, C. M., J. G. Kim, et al. (2005). "Effect of Co, Ga, and Nd Additions on the Photocatalytic Properties of TiO_2 Nanopowders." Glass Physics and Chemistry **31**(3): 390-395.

Wright, J. D. and N. A. Sommerdijk (2001). Sol-Gel Materials Chemistry and Applications. Boca Raton, FL, CRC Press.

Xiao, Z. and et al. (2008). "Effect of oxygen partial pressure on the ferromagnetism of Cr-doped TiO_2 films." Journal of Physics D: Applied Physics **41**(1): 015005.

Xie, T.-H. and J. Lin (2007). "Origin of Photocatalytic Deactivation of TiO_2 Film Coated on Ceramic Substrate." The Journal of Physical Chemistry C **111**(27): 9968-9974.

Xin, B., L. Jing, et al. (2005). "Effects of Simultaneously Doped and Deposited Ag on the Photocatalytic Activity and Surface States of TiO_2." The Journal of Physical Chemistry B **109**(7): 2805-2809.

Yakovlev, V. V., G. Scarel, et al. (2000). "Short-range order in ultrathin film titanium dioxide studied by Raman spectroscopy." Applied Physics Letters **76**(9): 1107-1109.

Ye, L.-H. and A. J. Freeman (2006). "Defect compensation, clustering, and magnetism in Cr-doped anatase TiO_2." Physical Review B **73**(8): 081304.

Yin, S., H. Hasegawa, et al. (2004). "Synthesis of visible-light-active nanosize rutile titania photocatalyst by low temperature dissolution-reprecipitation process." Journal of Photochemistry and Photobiology A: Chemistry **163**(1-2): 1-8.

Yu, J. and X. Zhao (2000). "Effect of substrates on the photocatalytic activity of nanometer TiO_2 thin films." Materials Research Bulletin **35**(8): 1293-1301.

Yu, J. and X. Zhao (2001). "Effect of surface treatment on the photocatalytic activity and hydrophilic property of the sol-gel derived TiO_2 thin films." Materials Research Bulletin **36**(1-2): 97-107.

Yu, J. C., J. Yu, et al. (2002). "Enhanced photocatalytic activity of mesoporous and ordinary TiO_2 thin films by sulfuric acid treatment." Applied Catalysis B: Environmental **36**(1): 31-43.

Yu, J. G., X. J. Zhao, et al. (2000). "Effect of film thickness on the grain size and photocatalytic activity of the sol-gel derived nanometer TiO_2 thin films." Journal of Materials Science Letters **19**(12): 1015-1017.

Zhang, H. and J. F. Banfield (2000). "Understanding Polymorphic Phase Transformation Behavior during Growth of Nanocrystalline Aggregates: Insights from TiO_2." The Journal of Physical Chemistry B **104**(15): 3481-3487.

Zhang, H., G. Wang, et al. (2008). "Tuning Photoelectrochemical Performances of Ag−TiO_2 Nanocomposites via Reduction/Oxidation of Ag." Chemistry of Materials **20**(20): 6543-6549.

Zhang, H. Z. and J. F. Banfield (1998). "Thermodynamic analysis of phase stability of nanocrystalline titania." Journal of Materials Chemistry **8**(9): 2073-2076.

Zhang, Z., C. C. Wang, et al. (1998). "Role of Particle Size in Nanocrystalline TiO_2-Based Photocatalysts." J. Phys. Chem. B **102**(52): 10871-10878.

Zhou, J., Y. Zhang, et al. (2006). "Photodegradation of Benzoic Acid over Metal-Doped TiO_2." Industrial & Engineering Chemistry Research **45**(10): 3503-3511.

Zywitzki, O., T. Modes, et al. (2004). "Structure and properties of crystalline titanium oxide layers deposited by reactive pulse magnetron sputtering." Surface and Coatings Technology **180-181**: 538-543.

CURRICULUM VITA

Murat Kurtoglu

Education

Ph.D. **Drexel University, Philadelphia, PA** **May 2011**
Materials Science and Engineering

B.S. **Middle East Technical University** **June 2005**
Materials Science and Engineering
Minor: Solid State Physics

Professional Experience

Gurallar ArtCraft	**2005-Present**
Project Manager	2010-Present
R&D Engineer	2006-2010
Product Development Engineer	2005-2006
Product Development Intern	June 2005 – Sep. 2005
Ege Ceramic Corp.	**June 2004 – Sep. 2004**
Quality Control Intern	

List of Publications

M.E. **Kurtoglu**, T. Longenbach, K. Sohlberg, and Y. Gogotsi, *Strong coupling of Cr and N in Cr-N-doped TiO_2 and its effect on photocatalytic activity*, **J. Phys. Chem. C**, **(under review)**

M. Naguib, **M.E. Kurtoglu**, V. Presser, J. Lu, J. Niu, M. Heon, L. Hultman, Y. Gogotsi, and M.W. Barsoum, **Adv. Mater., (under review)**

M.E. **Kurtoglu**, T. Longenbach, and Y. Gogotsi, *Synthesis of quasi-oriented α-*MoO_3 *nanobelts and nanoplatelets on* TiO_2 *coated glass.* **J. Mater. Chem.**, 2011, DOI: 10.1039/C1JM10752F

M.E. Kurtoglu, T. Longenbach, and Y. Gogotsi, *Preventing Sodium Poisoning of Photocatalytic* TiO_2 *Films on Glass by Metal Doping.* **Int. J. App. Glass Sci.**, 2011, 10.1111/j.2041-1294.2011.00040.x

M.E. Kurtoglu, T. Longenbach, P. Reddington, and Y. Gogotsi, *Effect of Calcination Temperature and Environment on Photocatalytic and Mechanical Properties of Ultrathin Sol-Gel Titanium Dioxide Films.* **J. Am. Ceram. Soc.**, **94** [4] 1101-1108, 2011.

Lee, B.-Y., K. Behler, **M.E. Kurtoglu**, M. Wynosky-Dolfi, R. Rest, and Y. Gogotsi, *Titanium dioxide-coated nanofibers for advanced filters.* **J. Nanoparticle Res.**, **12** [7] 2511-2519 (2010)

Lee, B.-Y., **M.E. Kurtoglu**, Y. Gogotsi, M. Wynosky-Dolfi, and R.F. Rest, *Solvothermal Synthesis of Photocatalytic* TiO_2 *Nanoparticles Capable of Killing Escherichia coli*, in ***Biodefence*, NATO Science for Peace and Security Series. A: Chemistry and Biology**, S. Mikhalovsky and A. Khajibaev, eds., Springer, pp. 3-10(2011)

M.E. Kurtoglu and Y. Gogotsi. *Photocatalytic and Mechanical Properties of* TiO_2 *Films Prepared by Sol-Gel Method*, in **Glass Performance Days 2009**. Tampere, Finland.

International Presentations

Eurasia Ceramics Congress, Kutahya, Turkey Oct. 2010
"Visible light photocatalysis by M-N co-doped TiO_2 Films"

Intl. Conf. and Exp. on Adv. Ceramics and Composites, Daytona Beach, FL Jan. 2010
"Increasing the photocatalytic activity of TiO_2 films on glass by metal doping"

Glass Performance Days, Tampere, Finland June 2009
"Photocatalytic and mechanical properties of TiO_2 films prepared by sol-gel method"